DEVELOPMENT OF THE TAMUTRAP FACILITY FOR PRECISION β-DECAY STUDIES

A Dissertation

by

MICHAEL SIMON MEHLMAN

Submitted to the Office of Graduate and Professional Studies of
Texas A&M University
in partial fulfillment of the requirements for the degree of

DOCTOR OF PHILOSOPHY

Chair of Committee,	Daniel Melconian
Committee Members,	Sherry Yennello
	John Hardy
	Bhaskar Dutta
Department Head,	George Welch

May 2015

Major Subject: Applied Physics

ABSTRACT

The Texas A&M University Penning Trap Facility (TAMUTRAP) is an ion trap system currently under construction, that will be used for precision nuclear physics experiments with radioactive beams provided by the Cyclotron Institute. Its primary focus is to search for possible scalar currents in $T = 2$ superallowed β-delayed proton decays, which, if found, would be an indication of physics beyond the standard model. In addition, TAMUTRAP will provide a low-energy, spatially localized source of ions for various other applications.

The experiment is centered around a unique, compensated cylindrical Penning trap that will employ a specially optimized length/radius ratio in the electrode structure that is not used by any other facility. A Radio Frequency Quadrupole (RFQ) Paul trap cooler and buncher will be used to prepare ions for loading into the Penning trap system. This thesis will cover the design and development of the Penning and Paul traps in addition to numerous ancillary components, such as electrostatic beam optics, control systems, electronics, detectors, and mechanical supports.

In particular, the TAMUTRAP RFQ cooler and buncher has been designed, fabricated, assembled, and commissioned and has been demonstrated to generate ion bunches with an approximate time spread of 1.8 μs full width at half max, suitable for acceptance into the TAMUTRAP measurement Penning trap. A theoretical design of the measurement Penning trap has been completed from first principles, which resulted in the description of a seven-electrode tunable and orthogonalized device of a completely new design. And, finally, numerous other beamline elements were developed, fabricated, and implemented after simulations detailing their behavior were performed.

DEDICATION

To my family: my parents Ed and Barbara Mehlman, and my baby brother Timothy.

ACKNOWLEDGEMENTS

I must first thank Dan Melconian who has been a pleasure to work with, an ally and advocate for my future, and a good friend. I also need to thank Praveen D. Shidling, who's guidance has been instrumental in keeping me on track. Praveen, I wish you the best of luck wherever the future takes you! And finally, thank you to Sherry Yennello for starting me down this path in 2008 and providing invaluable guidance and advice along the way.

I must also acknowledge the faculty and staff of the Cyclotron Institute. Greg Derrig, Steve Molitor, and Bob Olsen taught me the art of mechanical design, and spent hours correcting my work. Larry Whitely, James Raines, Andy Clark, and Richard Hanhart literally built this experiment, and were vital for modifying parts when designs didn't work out as planned. I am also grateful that our experiment bordered those of Dr. Gabrielle Tabacaru, and Dr. Greg Chubaryan, who I could always count on for help and advice. Fred, Howard, Ruben, Sharon, Steve Russel, and everyone else in the building: thank you for putting up with me for so many years, and legitimately making this an enjoyable place to work.

I must also recognize Guy Savard, Jens Dilling, Dave Morrissey, Ryan Ringle, Jason Clark, and Mel Good. I relied on these people for support and advice, and they were always generous with their knowledge.

This work was supported by the DOE under grants ER41747 and ER40773.

NOMENCLATURE

TAMUTRAP	Texas A&M University Penning Trap Facility
RFQ	Radio Frequency Quadrupole Paul trap
SM	Standard Model
T-REX	Texas A&M Re-accelerated Exotics

TABLE OF CONTENTS

Page

ABSTRACT ii

DEDICATION iii

ACKNOWLEDGEMENTS iv

NOMENCLATURE v

TABLE OF CONTENTS vi

LIST OF FIGURES ix

LIST OF TABLES xiv

1. INTRODUCTION 1

1.1 The Weak Interaction 2
1.2 TAMUTRAP 3
1.3 Contributions of this Thesis 5

2. THEORETICAL BACKGROUND 8

2.1 β-decay 8
2.1.1 $0^+ \rightarrow 0^+$ Decays 11
2.1.2 The Standard Model 13
2.1.3 Recoil Order Corrections 14
2.2 Observables 16

3. PROPOSED EXPERIMENT 19

3.1 Overview 19
3.2 Ion Traps 22
3.2.1 The Penning Trap 23
3.2.2 The Paul Trap 27
3.3 Decay Simulations 33
3.3.1 Monte Carlo Method 33

3.3.2 Exploring Analysis . . . 36

4. THE TAMUTRAP BEAM LINE . . . 39

4.1 Overview . . . 39
4.1.1 T-REX Upgrade and the Heavy Ion Guide . . . 40
4.2 Beam Line Simulation . . . 44
4.3 Basic Components . . . 46
4.4 Deflectors . . . 51
4.5 Diagnostic Station . . . 54
4.6 Ion Source . . . 63
4.7 Control System . . . 66
4.8 Present State and Future Work . . . 67

5. THE RFQ COOLER/BUNCHER . . . 70

5.1 Prototype . . . 70
5.2 The TAMUTRAP Cooler/Buncher . . . 74
5.2.1 Mechanical and Electrical Design . . . 75
5.2.2 Installation and Alignment . . . 82
5.3 Initial Characterization . . . 86
5.3.1 Continuous Mode . . . 87
5.3.2 Bunched Mode . . . 90
5.4 Present State and Future Work . . . 106

6. THE MEASUREMENT TRAP . . . 113

6.1 Design Considerations . . . 113
6.2 Orthogonalization . . . 115
6.3 Optimization . . . 119
6.4 Simulation with SIMION . . . 121
6.5 Comparison to Existing Traps . . . 123
6.6 Geometric Efficiency . . . 124
6.7 Present State and Future Work . . . 127

7. CONCLUSION . . . 130

REFERENCES . . . 134

APPENDIX A. OPTIMIZED OPERATING PARAMETERS FOR THE RFQ COOLER/BUNCHER 143

APPENDIX B. ELECTRIC FIELD OF THE MEASUREMENT TRAP . . . 145

LIST OF FIGURES

FIGURE Page

1.1 The TAMUTRAP beam line receives ∼10 keV RIB from the T-REX gas-catcher. This beam is transported via electrostatic beam optics to the RFQ cooler/buncher where it is prepared for subsequent transport to and loading in the precision measurement Penning trap. 4

2.1 The effect of recoil order and radiative corrections on the value of $a_{\beta\nu}$ as a function of β energy for the β-decay of ^{32}Ar [27]. The current limit on $a_{\beta\nu}$ is derived from the coupling constants presented in [25], and is presented in the shaded region. 15

2.2 The probability of β-decay as a function of $\theta_{\beta\nu}$ for different values of $a_{\beta\nu}$. Units on the radial axis are arbitrary. Here $p_e/E_e = 0.5$ and b is the value required by Eq. 2.13 in order to achieve the appropriate $a_{\beta\nu}$ by adding a scalar component to the weak interaction. 17

3.1 Decay scheme for a generic $T = 2$, $0^+ \rightarrow 0^+$ superallowed β-delayed proton decay (left), and the chart of the nuclides highlighting the $T = 2$ isotopes of interest (right). 20

3.2 Proton energy distributions for the β-delayed proton decay of ^{32}Ar with $a_{\beta\nu} = -1$, 0, and 1. Each curve contains one billion events. . . . 22

3.3 The three eigenmodes of motion in a perfect Penning trap. 24

3.4 A cartoon indicating the method of loading the Penning trap. The potential on the injection side is lowered (left) until the ion bunch is approximately centered in the trap (middle), at which point the injection side potential is returned to its normal value, trapping the particles (right). 26

3.5 An initial GEANT 4 simulation of a decay of interest within the Penning trap geometry. Here, the teal track shows the motion of the emitted proton, while the blue track traces the path of the β. 27

3.6 A simplified schematic of a linear quadrupole Paul trap employing cylindrical electrodes. 28

3.7 A contour plot highlighting regions of stable ion motion in a Paul trap. The overlapping area in the center represents stability in both principle directions. 30

3.8 68% statistical confidence level on $\tilde{a}$ (Eq. 3.10) about $\tilde{a} = 1$ for the $0^+ \rightarrow 0^+$ superallowed β decay of ^{32}Ar as a function of statistics (number of events in the test Monte Carlo). The dashed line represents the experimental sensitivity achieved by [1]. 37

4.1 A rendering of the entire TAMUTRAP experiment. 40

4.2 A rendering of the T-REX project connected to the TAMUTRAP facility. Various stages in beam production are highlighted. 41

4.3 An annotated view of the T-REX gas-catcher and multi-RFQ. 44

4.4 The injection optics for the RFQ (left) and the extraction optics (right). 45

4.5 The RFQ (left), extraction optics (center), and pulsing cavity (right) as simulated in SIMION. Here 50 ions are being cooled, ejected, accelerated to 10 keV, and, finally, pulsed to 3 keV energy. 47

4.6 Cross-section of a TAMUTRAP Einzel lens with three adjustable electrodes. 48

4.7 A view of the floating pulsing cavity. 49

4.8 A three-quarter section view of the spherical deflector. The inner surface is omitted for clarity. 51

4.9 The cylindrical deflector and a test beam line used for its characterization. 52

4.10 The inner and outer voltages needed to generate a 90° deflection (left), and the beam width in both horizontal (orange) and vertical (blue) directions for a 90° deflection at various outer electrode voltages (right). 53

4.11 Beam spots as viewed on the phosphor of an MCP detector before (left) and after (right) a 90° deflection. Images are not at exactly the same scale. 54

4.12 The TAMUTRAP diagnostic station centered on a Faraday cup and micro channel plate detector, here shown with the pepper pot emittance measurement attachment. The assembly is shown in wireframe to allow visibility of the inner configuration. 56

4.13 A sample emittance analysis in TEMP using data provided by Markus Strohmeier from Lawrence Berkley National Lab [59]. 60

4.14 TEMP calculated emittance as a function of hole-hole spacing at constant (50 mm) screen-mask spacing (left), and screen-mask spacing at constant (2 mm) hole-hole spacing (right) using simulated data. Spot-mask spacing was held at 1000 mm and the generated events exhibited a theoretical emittance of 5.9 mm·mrad. 61

4.15 Comparison of emittance values for actual data provided by Markus Strohmeier from Lawrence Berkley National Lab [59] versus the claimed emittance. 62

4.16 The ion gun electrode structure, which was designed by Yakup Boran [10]. 64

4.17 The TAMUTRAP facility as of late 2014. 68

5.1 A rendering of the mechanical design of the prototype RFQ. 71

5.2 The RC circuit used to block RF from damaging the DC power supplies. 72

5.3 A rendering of the mechanical design of the TAMUTRAP RFQ cooler/buncher.75

5.4 A photo of the TAMUTRAP RFQ cooler/buncher during test assembly. The in-vacuum electronic circuitry is visible at top and bottom. . . . 77

5.5 Peak-to-peak voltage as a function of power for the TAMUTRAP electrode structure, with a simple linear fit. 79

5.6 Sample output of the Behlke ultrafast high voltage switch before being installed. Courtesy of Louis Cooper. 80

5.7 Output of the Behlke ultrafast high voltage switch after installation. The electrodes pose a significant impedance load, slowing the rise and fall time. 81

5.8 A schematic of the test beam line used for initial characterization of the RFQ cooler/buncher. For scale, the RFQ chamber is approximately 97 cm in length. 83

5.9 The final achieved alignment can be seen at several locations along the beam line, as viewed through the optical transit. Thread indicating the flange center is highlighted with red lines, and opaque red dots highlight collimator centers, where applicable. 85

5.10 The collimated beam spot as seen on the first diagnostic MCP (located immediately before the injection optics). The spot is not concentric with the detector due to a misalignment in the detector mount, but can be injected into the RFQ with high efficiency. 88

5.11 Continuous mode efficiencies as a function of pressure for 20, 30, and 60 eV beam energies, with all DC RFQ voltages set to 0. Error bars are assuming an uncertainty in 0.1 pA on current measurements. . . . 89

5.12 Block diagram for acquisition as used in RFQ bunched-mode characterization. 90

5.13 A good bunch with skewed Gaussian fit superimposed. Beam energy = 30 eV, gas pressure = 3×10^{-3} mbar He, drag potential = 0.08 V/cm, incident beam current = 0.7 pA. FWHM of Gaussian fit = 1.89 μs. Note that the mean bunch time of ≈ 67 μs is consistent with a several μs time of flight (as predicted by SIMION) combined with the 50-60 μs fall time of the bunching potential wall, as in Fig. 5.7. 92

5.14 Bunches for which the eject duration was appropriate for the species of interest (left) and too long (right). Beam energy = 30 eV, gas pressure = 3×10^{-3} mbar He, drag potential = 0.08 V/cm. 94

5.15 Bunch FWHM (left) and yield (right) as a function of eject duration for the three primary identified bunches. Beam energy = 30 eV, gas pressure = 3×10^{-3} mbar He, drag potential = 0.08 V/cm. 95

5.16 Original analysis of bunch FWHM (left) and yield (right) as a function of eject duration for the first two bunches together, before they had been resolved individually (the final bunch was previously identified and was excluded in the fitting). Beam energy = 30 eV, gas pressure = 3×10^{-3} mbar He, drag potential = 0.08 V/cm. 96

5.17 Bunch FWHM (left) and yield (right) as a function of DC drag potential. Beam energy = 30 eV, gas pressure = 3×10^{-3} mbar He. . . 99

5.18 Bunch FWHM (left) and yield (right) as a function of buffer gas pressure. Beam energy = 30 eV, drag potential = 0.08 V/cm. Bunches did not form below about 25 mbar He. 100

5.19 Top: The stability diagram for ion motion in the Paul trap assuming the TAMUTRAP cooler/buncher geometry and singly-charged ^{23}Na trapped at 107 V_{PP}. Bottom: Bunch FWHM (left) and yield (right) as a function of RF frequency. Beam energy = 30 eV, gas pressure = 3×10^{-3} mbar He, drag potential = 0.08 V/cm. Peak to peak voltage was held at 107 V. 101

5.20 Top: The stability diagram for ion motion in the Paul trap assuming the TAMUTRAP cooler/buncher geometry and singly-charged ^{23}Na trapped at 1.0 MHz. Bottom: Bunch FWHM (left) and yield (right) as a function of RF voltage. Beam energy = 30 eV, gas pressure = 3×10^{-3} mbar He, drag potential = 0.08 V/cm. RF frequency was held at 1.00 MHz. 102

5.21 Bunch FWHM (left) and yield (right) as a function of incident beam current. Beam energy = 30 eV, gas pressure = 3×10^{-3} mbar He, drag potential = 0.08 V/cm. 103

5.22 Bunch FWHM (left) and yield (right) as a function of incident beam energy. Gas pressure = 3×10^{-3} mbar He, drag potential = 0.08 V/cm. 105

6.1 The trap geometry and boundary conditions used in the analytic solution. The device is symmetric about the $z = 0$ plane. 116

6.2 The optimized trap geometry with SIMION generated electric fields lines overlayed. 122

6.3 Sample geometric efficiency for collecting protons resulting from superallowed decays of interest as a function of trap half-length. For this plot, the entrance and exit apertures are assumed to be 2.4 mm, magnetic field strength is 7 T, and the trap is symmetric about the $Z = 0$ plane. 127

A.1 A good bunch with timespread FWHM = 1.89 μs. Beam energy = 30 eV, gas pressure = 3×10^{-3} mbar He, drag potential = 0.08 V/cm, incident beam current =0.07 pA. 143

B.1 The trap geometry and boundary conditions used in the analytic solution. The device is symmetric about the $z = 0$ plane. 146

LIST OF TABLES

TABLE Page

3.1 The $T = 2$ nuclei that will compose the initial experimental program measuring $a_{\beta\nu}$. The cyclotron radii, R_C, for the ejected protons of interest (having energy E_p) shown are calculated for the 7 T magnetic field of TAMUTRAP. 21

3.2 The inputs and some frequently used outputs for the Monte Carlo simulation of the decays of interest. 33

4.1 The production capabilities of the K150 cyclotron in combination with ECR ion source according to [56]. 42

4.2 Theoretical production rates for ions of interest via fusion evaporation reactions with ^{3}He [54]. 43

6.1 Expansion coefficients are compared for the optimized TAMUTRAP measurement trap when tuned (analytic and simulated) and three other existing Penning traps: TITAN (calculated analytically as in Ref. [11]), PENTATRAP (calculated analytically as in Ref. [45]), and LEBIT (simulated using SIMION as in Ref. [47]). 122

A.1 Operating parameters for the bunch pictured in Fig. A.1. Drag potential is approximately 0.08 V/cm. 144

1. INTRODUCTION

The Standard Model (SM), developed in the 1960's and 1970's, is currently society's best working framework for unifying the fundamental forces known in nature. As such, the SM provides a consistent description of three of the four forces: electromagnetism, the weak force, and the strong force. Though the formalism does not account for inclusion of the fourth fundamental force, gravity, it has still demonstrated wildly successful predictive power (for example anticipating the masses of $W^{\pm}$, Z^0 and Higgs bosons prior to their discovery). Despite this great success, however, there are still many unanswered questions, such as determination of the non-zero neutrino masses, and inclusion of gravity in the formalism, among others. It is our duty to probe the limits of this current best theory, both to search for answers to these remaining open questions, and to assure its absolute validity at any precision level.

From Wu's groundbreaking experiment [65] to the present day [53, 51, 5], low energy precision β-decay studies have proven to be an efficient avenue for probing the weak interaction and, in so doing, the Standard Model. The Texas A&M Penning Trap (TAMUTRAP) facility at the Texas A&M University Cyclotron Institute aims to continue this tradition by searching for possible contributions from non-SM processes in the weak interaction. In particular, we ultimately seek to measure the $\beta - \nu$ correlation parameter [1] for certain decays to the 0.1% level, putting tighter limits on the currently accepted time reversal invariant $V - A$ interaction.

This thesis will discuss the experiment that is being constructed to perform the $\beta - \nu$ correlation parameter measurements at the Texas A&M University Cyclotron Institute. Particular attention will be paid to hardware design of the beam line and

the unique novel measurement Penning trap that will be employed for the completion of these studies. Simulations, and analytic and mechanical designs will be covered, and fabrication, assembly, testing, and characterization of various components will be presented.

1.1 The Weak Interaction

The weak force, one of the four fundamental forces, governs the interaction between half-integer spin particles, *i.e.* fermions. As such, it dictates the behavior of radioactive β (spin = 1/2) decay, which underlies processes as diverse as the burning of hydrogen in the sun via the proton-proton chain and the decay of ^{14}C employed for radio-carbon dating.

The formalism of the weak interaction that has so far proven to empirically describe the weak force was initially postulated in 1933 by Enrico Fermi, and was published the following year in 1934 [14] strictly in German and Italian language journals[1]. This first description of the weak force details a four-body contact interaction between the particles involved (a coupling of two parity-conserving vector currents), defined by the Fermi coupling constant, G_F, for which the currently accepted value is $G_F = 1.166364 \times 10^{-5}$ GeV^{-2} [36]. This is the weakest *coupling constant* for any of the fundamental forces, hence the name[2]. Later, in 1956, Lee and Yang suggested that a parity-violating axial current [34] need not be forbidden in the description of the weak interaction (for which the formalism was established in 1936 by Gamow and Teller [22]). This parity violation was later confirmed experimentally by Wu [65] and others [23]. As a result, and with further work performed by Sudarshan and Marshak and others [60, 15], the weak force was shown to be

[1]Interestingly, the English-language Journal that Fermi's paper was first submitted to, Nature, refused it on grounds that it was "too speculative."

[2]This should not be confused with the actual observed strengths of the forces. For the accessible energy regime, the electromagnetic force displays the weakest strength.

described correctly by a parity-violating vector − axial vector, or $V - A$, structure.

Today, Fermi's formulation has been replaced by an interaction derived from the electroweak theory as developed by Salam, Glashow and Weinberg in 1967 [63], which calls for the exchange of a $W^{\pm}$ or Z^0 boson to propagate the interaction over very short distances. In fact, it is because these bosons interact over such short distances that Fermi's contact model was able to stand up as an initial theory. This description, part of what we refer to as the SM, has so far been shown to express a maximal violation of parity in nature, and is consistent, as mentioned above, with the $V - A$ picture of the interaction. However, also mentioned above, the formalism exists for specifying components of other currents involved in the weak interaction, such as a scalar or tensor term.

It is primarily this scalar current that we wish to search for with the TAMUTRAP experiment. As will be discussed in Ch. 2, simple pure-Fermi β-decays can mathematically only display a vector or scalar current. The SM currently predicts no contribution from the scalar current, and, as a result, an experimental deviation from the SM prediction would be an indication of new physics beyond the SM. With clever measurement techniques, information on the channel by which such a weak decay occurs will be available through decay kinematics captured by the TAMUTRAP experiment, as will be introduced in §1.2.

1.2 TAMUTRAP

The proposed TAMUTRAP experiment (Fig. 1.1) will focus on measuring the proton energy spread in β-delayed proton decays in order to infer the value of the Standard Model $\beta - \nu$ correlation parameter, $a_{\beta\nu}$ [1]. The value of $a_{\beta\nu}$ parametrizes the angular correlation between the β and ν in nuclear β-decay, a result of treating the involved particles relativistically [6]. To do this, an ultra-pure collection of radioac-

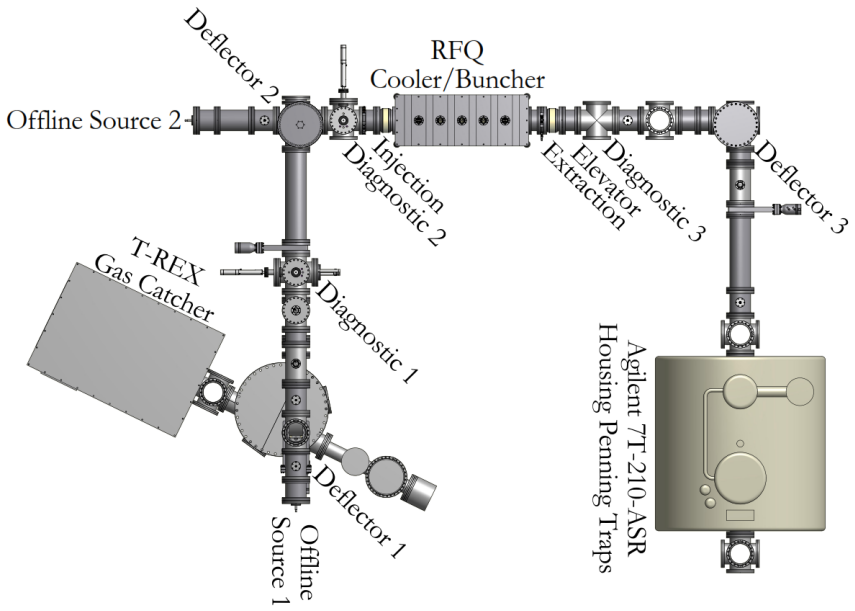

Figure 1.1: The TAMUTRAP beam line receives ∼10 keV RIB from the T-REX gas-catcher. This beam is transported via electrostatic beam optics to the RFQ cooler/buncher where it is prepared for subsequent transport to and loading in the precision measurement Penning trap.

tive ions provided by the Texas A&M re-accelerated exotics (T-REX) upgrade at the Texas A&M University Cyclotron Institute (in this case ^{32}Ar and other select $T = 2$ nuclides) will be stored in a novel measurement Penning trap. From this stopped, background-free location, decays will occur and the energies of protons of interest and βs will be read out via detectors located at the trap endcaps. Here, the proton energy distribution is sensitive to the value of the $\beta - \nu$ correlation parameter, and therefore can be used to infer details on the form of the weak interaction, while detection of the betas will allow for enhanced sensitivity and reduced systematics by allowing detection coincidences. The theoretical foundation for this method will be discussed in more detail in Ch. 2.

The planned experimental approach is similar to that employed by Adelberger, et al. in the late 1990's [1]. In Adelberger's measurement, radioactive ^{32}Ar was

implanted in a foil sandwiched between two silicon detectors. The detectors were used to observe the proton energy distribution from β-delayed proton decays originating from the stopped radioactive ions, which, in turn, was employed to put limits on the values of certain SM correlation parameters for these decays.

TAMUTRAP will be performing the same measurement in spirit, with enhanced sensitivity due to an improved experimental setup and an extended initial program of β-delayed proton emitters made possible by the radioactive ion beam (RIB) capabilities of the T-REX upgrade at the Cyclotron Institute. As a result of performing the measurements from within a Penning trap (which provides an ultra-low-background, cold, spatially localized source of radioactive ions), TAMUTRAP will exhibit several distinct advantages compared to Adelberger's pioneering experiment, including increased (near 4π) geometric efficiency, reduced impact on proton energies due to the shallow Penning trap ion source, and the ability to contain and measure resulting βs. These features are intended to result in a clean proton energy spectrum (having a minimum of untestable systematics), which will be used as discussed in the coming chapters to determine an improved value of the $\beta - \nu$ correlation parameter and set limits on the existence of scalar currents in the SM.

1.3 Contributions of this Thesis

As an applied physics project, my work on the TAMUTRAP facility has been skewed toward design and fabrication of the experimental apparatus. In particular, a deep understanding of the physics was achieved, mathematical simulations were performed, and designs for new components were generated, culminating in the fabrication and assembly of numerous key elements of the TAMUTRAP beam line.

First, physics simulations of various aspects of the experiment were performed. An object-oriented, Monte Carlo simulation was developed in C++ to better un-

derstand the experimental observables and for initial vetting of the experimental strategy. Deterministic calculations and SIMION ion-trajectory simulations were also performed to better understand the kinematics of the decay in the proposed apparatus. These contributions are discussed in Ch. 2.

Next, I completed a full mechanical design of the optimized beam line from the exit of the T-REX upgrade (to be discussed briefly in Ch. 4) to the entrance of the 7 T magnet, which is planned to house the Penning trap measurement device. All elements, including electrode structures, beam supports, and alignment jigs, are new designs for this facility. This work is discussed in Ch. 4, along with an overview of various electronics and the preliminary control system designed for the facility.

As part of the development of the beam line, I designed and constructed an emittance station and associated control, acquisition, and analysis software for determination of transverse emittance of the radioactive ion beam (RIB) via the pepper-pot technique [62]. The design and theory of this device is presented in Ch. 4.

The most critical element of the beam line after the T-REX line and prior to the measurement device is the gas-filled Radio Frequency Quadrupole Paul trap, detailed in Ch. 5, which is necessary for bunching as well as matching the emittance of the incoming radioactive ion beam to the acceptance of the measurement Penning trap. For this work, I performed a complete mechanical design of this device and commissioned and characterized the apparatus in both bunched and continuous modes, the results of which will also be discussed in detail in Ch. 5.

Finally, as part of the simulation process, I completed a theoretical design of the intended measurement Penning trap device. This involved an expansion on the work presented in [21], removing key assumptions to arrive at an original and complete analytic solution for the electric field of a tunable Penning trap with short endcaps. This work was subsequently used to optimize the geometry of the proposed novel

Penning trap for the measurements of interest [37], which will be described in Ch. 6, and further detailed in Appendix B.

2. THEORETICAL BACKGROUND

Our present understanding of the weak interaction through the lens of the Standard Model is understandably much more complete than Fermi's initial 1933 formulation. However, there are still many curious features of the current theory that must be explored to greater and greater precisions in order to attain a more complete understanding of this fundamental force. This chapter will discuss our most general picture of nuclear β-decay, the constraints imposed on this theory by the SM, and how we might search for evidence of physics beyond the SM by considering and observing certain favorable $T = 2$, superallowed β-decays.

2.1 β-decay

Expanding on the work of Gamow and Teller [22] and others, Jackson, Treiman, and Wyld defined the general mathematical form for nuclear β-decay, disregarding assumptions about implicit symmetries in their work [28]. Starting with a generic Hamiltonian including scalar, pseudo-scalar, vector, axial vector, and tensor terms, they arrived at a decay rate for four-body β-decay consistent with Lorentz invariance. Eq. 2.1 gives the rate for an allowed decay with original nuclear angular momentum oriented along $\mathbf{j}$, in terms of β and ν directions and β energy [28]:

$$\begin{aligned}
&\omega\left(\langle J\rangle\left|E_e,\Omega_e,\Omega_\nu\right.\right)\propto \\
&\frac{F\left(Z,p_e\right)}{\left(2\pi\right)^5}p_eE_e\left(E^0-E_e\right)^2dE_ed\Omega_ed\Omega_\nu\xi\left\{1+a_{\beta\nu}\frac{\mathbf{p_e}\cdot\mathbf{p}_\nu}{E_eE_\nu}+b\frac{m_e}{E_e}\right. \\
&+c\left[\frac{1}{3}\frac{\mathbf{p_e}\cdot\mathbf{p}_\nu}{E_eE_\nu}-\frac{\left(\mathbf{p_e}\cdot\mathbf{j}\right)\left(\mathbf{p}_\nu\cdot\mathbf{j}\right)}{E_eE_\nu}\right]\left[\frac{J\left(J+1\right)-3\left\langle\left(\mathbf{J}\cdot\mathbf{j}\right)^2\right\rangle}{J\left(2J-1\right)}\right] \\
&\left.+\frac{\langle\mathbf{J}\rangle}{J}\cdot\left[A\frac{\mathbf{p_e}}{E_e}+B\frac{\mathbf{p}_\nu}{E_\nu}+D\frac{\mathbf{p_e}\times\mathbf{p}_\nu}{E_eE_\nu}\right]\right\}. \qquad (2.1)
\end{aligned}$$

Here, Ω_e and Ω_ν are the solid angles of the β particle and ν; E_e, E^0, p_e, and m_e are the energy, maximum available energy, momentum, and mass for the β; E_ν and p_ν are the energy and momentum of the ν; J is the nuclear spin; $\langle \mathbf{J} \rangle$ is the expectation value of the nuclear spin of the parent (with $\mathbf{j}$ a unit vector in the direction of $\mathbf{J}$); $F(Z, p_e)$ is the Fermi function; and ξ, $a_{\beta\nu}$, b, c, A, B, and D are the correlation parameters that reference the mathematically possible currents involved in the weak interaction. The decay rate is given as a proportionality to indicate that it can be presented with additional terms corresponding to β polarization, etc., which are not considered here. It should be noted that the results presented do not include any of the so-called "recoil order" corrections, various terms of order p_e/M_i or higher where M_i is the mass of the parent nucleus [28]. The effect of these terms will be briefly considered in §2.1.3. The correlation parameters are then, in turn, given by Eqs. 2.2-2.8:

$$\xi = |M_F|^2 \left(|C_S|^2 + |C_V|^2 + |C_S^{'}|^2 + |C_V^{'}|^2\right)$$
$$+ |M_{GT}|^2 \left(|C_T|^2 + |C_A|^2 + |C_T^{'}|^2 + |C_A^{'}|^2\right), \tag{2.2}$$

$$a_{\beta\nu}\xi = |M_F|^2 \left\{\left(-|C_S|^2 + |C_V|^2 - |C_S^{'}|^2 + |C_V^{'}|^2\right)\right.$$
$$\left. \mp \frac{\alpha Z m_e}{p_e} 2\Im m \left(C_S C_V^* + C_S^{'} C_V^{'*}\right)\right\}$$
$$+ \frac{|M_{GT}|^2}{3} \left\{\left(|C_T|^2 - |C_A|^2 + |C_T^{'}|^2 - |C_A^{'}|^2\right)\right.$$
$$\left. \pm \frac{\alpha Z m_e}{p_e} 2\Im m \left(C_T C_A^* + C_T^{'} C_A^{'*}\right)\right\}, \tag{2.3}$$

$$b\xi = \pm 2\Re e \left[|M_F|^2 \left(C_S C_V^* + C_S^{'} C_V^{'*}\right) + |M_{GT}|^2 \left(C_T C_A^* + C_T^{'} C_A^{'*}\right)\right], \tag{2.4}$$

$$c\xi = |M_{GT}|^2 \Lambda_{J'J} \left\{\left(|C_T|^2 - |C_A|^2 + |C_T^{'}|^2 - |C_A^{'}|^2\right)\right.$$
$$\left. \pm \frac{\alpha Z m_e}{p_e} 2\Im m \left(C_T C_A^* + C_T^{'} C_A^{'*}\right)\right\}, \tag{2.5}$$

$$A\xi = |M_{GT}|^2 \lambda_{J'J} \left[\pm 2\Re e \left(C_T C_T^{'*} - C_A C_A^{'*}\right) + \frac{\alpha Z m_e}{p_e} 2\Im m \left(C_T C_A^{'*} + C_T^{'} C_A^*\right)\right]$$
$$+ \delta_{J'J} |M_F||M_{GT}| \left(\frac{J}{J+1}\right)^{\frac{1}{2}} \left[2\Re e \left(C_S C_T^{'*} + C_S^{'} C_T^* - C_V C_A^{'*} - C_V^{'} C_A^*\right)\right.$$
$$\left. \pm \frac{\alpha Z m_e}{p_e} 2\Im m \left(C_S C_T^{'*} + C_S^{'} C_T^* - C_V C_A^{'*} - C_V^{'} C_A^*\right)\right], \tag{2.6}$$

$$B\xi = 2\Re e \left\{|M_{GT}|^2 \lambda_{J'J} \left[\frac{m}{E_e} \left(C_T C_A^{'*} - C_T^{'} C_A^*\right) \pm \left(C_T C_T^{'*} - C_A C_A^{'*}\right)\right]\right.$$
$$- \delta_{J'J} |M_F||M_{GT}| \left(\frac{J}{J+1}\right)^{\frac{1}{2}} \times \left[\left(C_S C_T^{'*} + C_S^{'} C_T^* - C_V C_A^{'*} - C_V^{'} C_A^*\right)\right.$$
$$\left.\left. \pm \frac{m}{E_e} \left(C_S C_A^{'*} + C_S^{'} C_A^* - C_V C_T^{'*} - C_V^{'} C_T^*\right)\right]\right\}, \tag{2.7}$$

$$D\xi = \delta_{J'J} |M_F||M_{GT}| \left(\frac{J}{J+1}\right)^{\frac{1}{2}} \left\{2\Im m \left(C_S C_T^* - C_V C_A^* + C_S^{'} C_T^{'*} - C_V^{'} C_A^{'*}\right)\right.$$
$$\left. \mp \frac{\alpha Z m_e}{p_e} 2\Re e \left(C_S C_A^* - C_V C_T^* + C_S^{'} C_A^{'*} - C_V^{'} C_T^{'*}\right)\right\}. \tag{2.8}$$

C_X and C'_X are the generally complex coupling constants for $X = S$ (scalar), V (vector), A (axial vector), and T (tensor) interactions. The pseudo-scalar coupling constants have been ignored due to a non-relativistic treatment of the nucleons, as in [51], and both C_X and C'_X are present in order to allow for violation of parity [65]. M_F and M_{GT} are the Fermi and Gamow-Teller nuclear matrix elements, and Z, α, m_e, and p_e are the atomic number of the final nucleus, the fine structure constant, the mass of the β (as above), and the β momentum. The $\pm$ signs are applicable to $\beta\mp$ decay. For initial nuclear angular momentum J and final nuclear angular momentum J', $\lambda_{J'J}$ and $\Lambda_{J'J}$ are defined as:

$$\lambda_{J'J} = \begin{cases} 1 & J' = J - 1 \\ 1/(J+1) & J' = J \\ -J/(J+1) & J' = J + 1, \end{cases} \tag{2.9}$$

and

$$\Lambda_{J'J} = \begin{cases} 1 & J' = J - 1 \\ -(2J-1)/(J+1) & J' = J \\ J(2J-1)/[(J+1)(2J+3)] & J' = J + 1. \end{cases} \tag{2.10}$$

The decay rate equations that result from this approach are quite daunting if all terms are to be considered. Fortunately, certain decays exist that reduce the complexity of these equations without imposing any preference by nature as to what channel the weak decay favors.

2.1.1 $0^+ \to 0^+$ *Decays*

In particular, the mathematics becomes much more tractable if we choose to observe $0^+ \to 0^+$ superallowed decays, in which both total angular momentum and

parity are conserved.

According to Fermi's Golden Rule, the transition rate between initial and final states via any perturbative interaction is proportional to the matrix element for that interaction squared. We know there is 0 probability for a $0^+ \to 0^+$ decay to proceed via a Gamow-Teller transition since no spin can be transferred. As a result, we require $M_{GT} = 0$. Additionally, in these decays $J_i = J_f = 0$, which reduces Eqs. 2.9 and 2.10 to reduce to $\lambda_{0,0} = 1$ and $\Lambda_{0,0} = 1$, respectively. These considerations yield a terrific simplification for the correlation parameters listed above:

$$\xi = |M_F|^2 \left(|C_S|^2 + |C_V|^2 + |C_S^{'}|^2 + |C_V^{'}|^2 \right), \tag{2.11}$$

$$\begin{aligned} a_{\beta\nu}\xi = &|M_F|^2 \left\{ \left(-|C_S|^2 + |C_V|^2 - |C_S^{'}|^2 + |C_V^{'}|^2 \right) \right. \\ &\left. \mp \frac{\alpha Z m_e}{p_e} 2\Im m \left(C_S C_V^* + C_S^{'} C_V^{'*} \right) \right\}, \end{aligned} \tag{2.12}$$

$$b\xi = \pm\, 2\Re e |M_F|^2 \left(C_S C_V^* + C_S^{'} C_V^{'*} \right), \tag{2.13}$$

$$c\xi = 0, \tag{2.14}$$

$$A\xi = 0, \tag{2.15}$$

$$B\xi = 0, \tag{2.16}$$

$$D\xi = 0, \tag{2.17}$$

which leads to a similarly impressive simplification of the decay rate for an oriented nucleus, Eq. 2.1:

$$\begin{aligned} &\omega \left(\langle J \rangle \, | E_e, \Omega_e, \Omega_\nu \right) \propto \\ &\frac{F\left(Z, p_e\right)}{\left(2\pi\right)^5} p_e E_e \left(E^0 - E_e \right)^2 dE_e d\Omega_e d\Omega_\nu \xi \left(1 + a_{\beta\nu} \frac{\mathbf{p_e} \cdot \mathbf{p}_\nu}{E_e E_\nu} + b \frac{m_e}{E_e} \right). \end{aligned} \tag{2.18}$$

2.1.2 The Standard Model

The SM currently incorporates the strong, electromagnetic and weak forces into one mathematical formalism, with a number of constants defined empirically. The most fundamental constants pertaining to the weak interaction are the coupling constants, C_X and $C_X^{'}$.

Experiment has so far exposed the weak force as a completely vector and axial-vector process, with these terms exhibiting opposite relative sign, yielding the inherently left-handed $V-A$ structure that is currently accepted in the SM [51]. No contributions from scalar, tensor, or pseudo-scalar currents have so far been observed. As a result, the SM adopts the following values for the coupling constants defining the relative strengths of the various currents possible in the weak interaction:

$$C_V = 1,\, C_V^{'} = 1,\, C_A = -1,\, C_A^{'} = -1, \tag{2.19}$$

and

$$C_S = C_S^{'} = C_P = C_P^{'} = C_T = C_T^{'} = 0. \tag{2.20}$$

Here we have $|C_X| = |C_X^{'}|$ due to the fact that parity has so far been observed to be maximally violated [51].

Plugging these values into Eqs. 2.11-2.13 yields $a_{\beta\nu} = 1$ and $b = 0$ for the $0^+ \rightarrow 0^+$ decays of interest, which further simplifies Eq. 2.18:

$$\begin{aligned} &\omega\left(\langle J\rangle\,|E_e,\Omega_e,\Omega_\nu\right) \propto \\ &\frac{F\left(Z,p_e\right)}{\left(2\pi\right)^5} p_e E_e \left(E^0-E_e\right)^2 dE_e d\Omega_e d\Omega_\nu \xi \left(1+\frac{\mathbf{p_e}\cdot\mathbf{p}_\nu}{E_e E_\nu}\right). \end{aligned} \tag{2.21}$$

Under this approximation, any observed deviation from Eq. 2.21 for a $0^+ \rightarrow 0^+$

decay ($M_{GT} = 0$) will imply the existence of a scalar current, *i.e.* C_S, $C'_S \neq 0$, which is inconsistent with the current empirically-motivated formulation of the SM.

Tests confirm the SM to very high precision at energy regimes currently accessible in the lab, so any framework that goes beyond the SM to incorporate scalar currents in the weak interaction must still reduce to the observed form. Current theories explaining a possible scalar current involve the exchange of a presently unobserved boson or leptoquark in place of the accepted W-boson [52], and would therefore require significant modifications to our understanding of the weak force and the SM. In so doing, the observation of a scalar component to the weak interaction would both further validate the pursuit of physics beyond the SM, and give direction to the search for a more complete and elegant unified theory.

2.1.3 Recoil Order Corrections

The Hamiltonian used to calculate the decay rate in [28] (here Eq. 2.1) includes only the terms relative to the lepton interaction of the weak force. There are, however, additional contributions to the energy of the system that must be included in order to obtain a complete picture of the interaction.

In particular, there are kinematic effects (due to nuclear recoil, hence the name "recoil order corrections"), electromagnetic effects (dubbed "radiative corrections"), and weak magnetism effects that ultimately appear at the order of p_e/M_i and higher in the decay rate (where, again, M_i is the mass of the parent nucleus). The consequences of these terms on the β-decay rate have been calculated by Holstein, and are detailed explicitly in [27]. The result is that the correlation parameters gain an energy dependence when taking these terms into account. Then, according to the

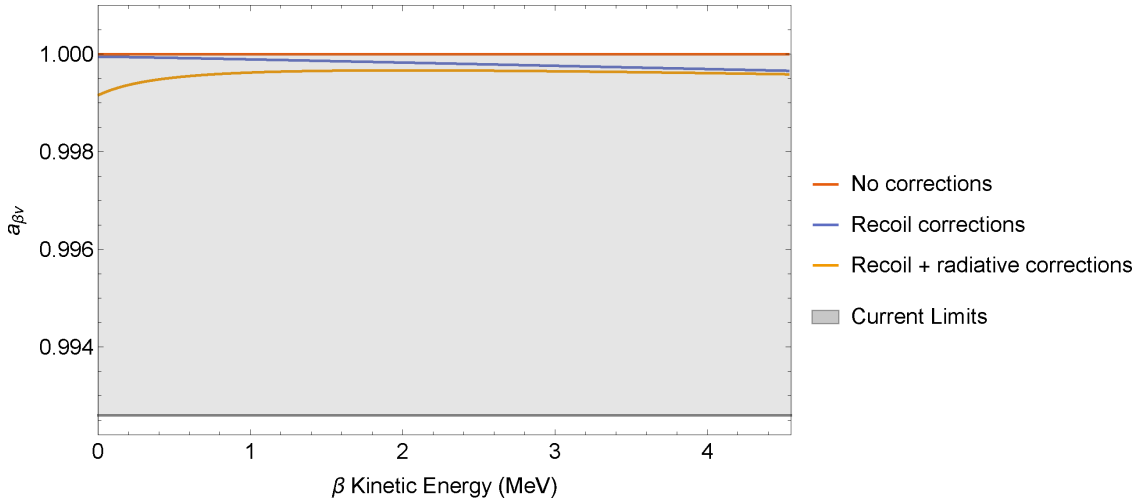

Figure 2.1: The effect of recoil order and radiative corrections on the value of $a_{\beta\nu}$ as a function of β energy for the β-decay of ^{32}Ar [27]. The current limit on $a_{\beta\nu}$ is derived from the coupling constants presented in [25], and is presented in the shaded region.

SM the relevant correlation parameter for this work, $a_{\beta\nu}$, is given by [39, 27]:

$$\begin{aligned} a_{\beta\nu} &= 1 && \text{No corrections} \\ a_{\beta\nu} &= \frac{f_2(E_e)}{f_1(E_e)} && \text{Recoil corrections} \\ a_{\beta\nu} &= \frac{f_2(E_e) + \Delta f_2(E_e)}{f_1(E_e) + \Delta f_1(E_e)} && \text{Recoil and radiative corrections.} \end{aligned} \tag{2.22}$$

The functions $f_1(E_e)$, $f_2(E_e)$, $\Delta f_1(E_e)$, and $\Delta f_2(E_e)$ are given in [27]. Fig. 2.1 shows $a_{\beta\nu}$ as a function of energy for the case of the β-decay of ^{32}Ar, one of the decays of interest, over the entire kinetic energy range available to the β, and includes the current experimental limits on this correlation parameter as calculated in [25]. The combination of these higher order corrections makes up to $\approx$0.08% effect on the value of $a_{\beta\nu}$ for this specific decay. As a result, it is important to consider the consequences of these terms, depending on the expected experimental precision. The energy dependence of $a_{\beta\nu}$ can be similarly calculated for other decays using [27]

and [39].

Though the energy dependence of the correlation parameters complicates the simple picture of the decay, it is fortunate that these terms are suppressed by p_e/M_i. For the remainder of this thesis only corrections due to the kinematic recoil of the daughter nucleus will be included. The effect of this term on the decay rate is calculated in [38], and is consistent with the decay rate presented in [1]:

$$\omega\left(\langle J\rangle\left|E_e,\Omega_e,\Omega_\nu\right.\right) \propto \frac{F\left(Z,p_e\right)}{\left(2\pi\right)^5} p_e E_e \left(E^0-E_e\right)^2 dE_e d\Omega_e d\Omega_\nu \xi \times \left(1+a_{\beta\nu}\frac{\mathbf{p_e}\cdot\mathbf{p}_\nu}{E_e E_\nu}+b\frac{m_e}{E_e}\right)\left(\frac{M_f}{M_i-E_e-p_e\cos\theta_{\beta\nu}}\right). \quad (2.23)$$

Here, M_i and M_f are the masses of the parent and daughter nuclei respectively, and the rest of the variables have been defined previously. The effect of the recoiling nucleus is encompassed in the final term. The decay rate as given in Eq. 2.23, including the lowest order recoil-order corrections, will be used from here on.

2.2 Observables

If we are to search for such a scalar current in the proposed $0^+ \rightarrow 0^+$ decays, it is important to understand what physical observables will be of access for study. Taking Eq. 2.23 (here we ignore the recoil order corrections for simplicity) and removing the constants yields:

$$\omega\left(\langle J\rangle\left|E_e,\Omega_e,\Omega_\nu\right.\right) \propto dE_e d\Omega_e d\Omega_\nu \left(1+\frac{p_e}{E_e}a_{\beta\nu}\cos\theta_{\beta\nu}+b\frac{m_e}{E_e}\right), \quad (2.24)$$

where we have chosen to represent the dot product between β and neutrino momenta in terms of its magnitude and the physical angle between the two particles. The upper limit on the sum of the three neutrino masses is ≈ 0.320 eV [4], so that it is safe for

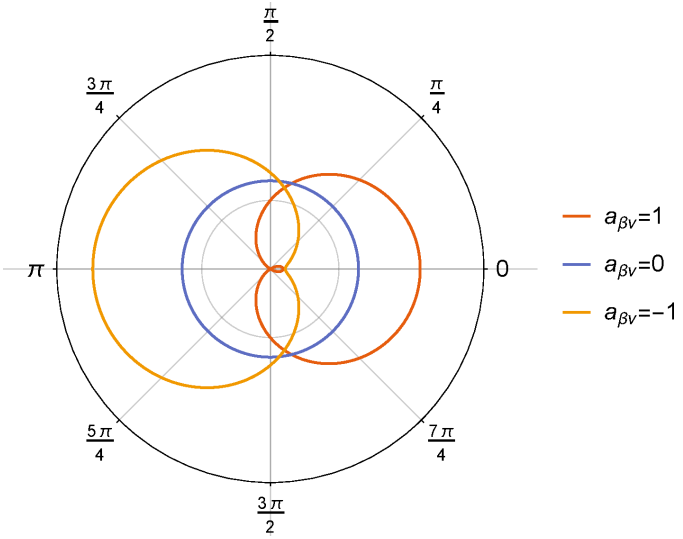

Figure 2.2: The probability of β-decay as a function of $\theta_{\beta\nu}$ for different values of $a_{\beta\nu}$. Units on the radial axis are arbitrary. Here $p_e/E_e = 0.5$ and b is the value required by Eq. 2.13 in order to achieve the appropriate $a_{\beta\nu}$ by adding a scalar component to the weak interaction.

these purposes to assume a massless neutrino and take $p_\nu/E_\nu \approx 1$.

If we are interested in studying the correlation parameters, which contain information about the decay channel, we should look at the observables that appear in their respective terms. From Eq. 2.24, we can see that $a_{\beta\nu}$ appears along side the momentum of the positron, p_e, and the cosine of the angle between the β and ν, $\cos\theta_{\beta\nu}$. Here we will focus on the effect of this latter geometric factor.

It is clear to see that the existence of a scalar component in the weak interaction, which alters the values of $a_{\beta\nu}$ and b via Eqs. 2.11-2.13, drastically changes the behavior of the cross section as a function of $\theta_{\beta\nu}$, as indicated in Fig. 2.2. It is therefore possible to determine the strength of such a scalar component by means of an experimental measurement of the cross section as a function of the angular distribution between the β and ν. That is, measuring the distribution of $\theta_{\beta\nu}$ over many decays allows one to deduce the value of $a_{\beta\nu}$.

Additionally, simple conservation of momentum states that the sum of the β, ν, and daughter momenta must be exactly equal to 0 (assuming the decay occurs from rest). In this way it is easy to see that conservation of momentum requires that the recoil ion achieves a relatively greater momentum magnitude when the β and ν are aligned, and a relatively smaller momentum when the β and ν are anti-aligned. The degree of the momentum kick imparted to the recoil, which corresponds to the angle between the β and neutrino and their kinetic energies, facilitates investigation into the $\beta - \nu$ correlation parameter, and, thereby, the decay channels of the weak interaction.

Measuring the energy, and therefore inferring the momentum, of the recoiling daughter poses its own experimental difficulties, which can be overcome by a clever choice of decay system, as will be discussed in Ch. 3.

3. PROPOSED EXPERIMENT

The TAMUTRAP facility will employ a novel, large-bore Penning trap for precise measurement of the $\beta - \nu$ correlation parameter in specially chosen $0^+ \rightarrow 0^+$ β-decays. The value of $a_{\beta\nu}$ will be compared to the SM prediction in order to search for new physics. As discussed in §2.1.2, any deviation from the standard model value for $a_{\beta\nu}$ in these favorably simple $0^+ \rightarrow 0^+$ decays would be an indication of the existence of a scalar current in the weak interaction, which is currently forbidden by the SM. This chapter will describe how the TAMUTRAP experiment aims to measure $a_{\beta\nu}$, covering both the experimental strategy and some initial simulations of the β-decays of interest.

3.1 Overview

Ch. 2 highlighted the physical observables available when searching for non-SM processes through the aforementioned β-decays. In review, the intended method is to observe the experimental decay rate as a function of the angle between the β and ν, $\theta_{\beta\nu}$, and compare with the decay rate predicted by the SM. Due to the minuscule cross-section for ν detection, it must be considered infeasible to observe this angle directly. As a result, §2.2 described a method to sidestep this issue by observing the momentum kick inherited by the recoiling daughter ion, which, as a result of conservation of linear momentum, corresponds to the angle of interest.

However, due to its large mass, the recoiling daughter nucleus inherits a very small kinetic energy, on the order of $\lesssim$500 eV. Such low ion kinetic energy makes detection using standard solid-state techniques very difficult. The energy threshold for silicon detectors (which are planned for use in the TAMUTRAP facility) is around 1 keV [18], and, as a result, observing the daughter's kinetic energy directly by this

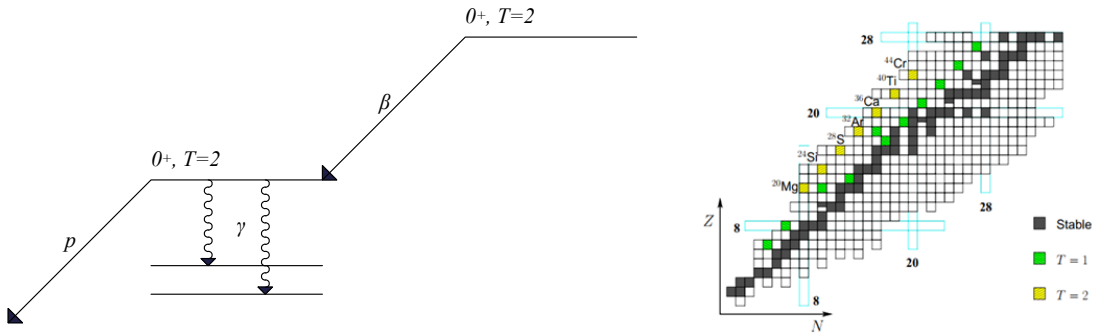

Figure 3.1: Decay scheme for a generic $T = 2$, $0^+ \rightarrow 0^+$ superallowed β-delayed proton decay (left), and the chart of the nuclides highlighting the $T = 2$ isotopes of interest (right).

means is not an option.

If the daughter of the β-decay is unstable with very short lifetime, the energy spread it is imparted as a result of the kinematics of the original decay can be passed on to subsequent decay products, since subsequent decays occur from a moving reference frame. If a secondary decay product is detectable, one can then search for an energy spread around its natural decay energy, which can be much easier to observe precisely.

It is for this reason that we have chosen to study $T = 2$, $0^+ \rightarrow 0^+$ superallowed β-delayed proton emitters at TAMUTRAP (the generic decay scheme and ions of interest are shown in Fig. 3.1). In these decays, the initial $T = 2$ nuclides, which have lifetimes on the order of 100 ms, may decay into proton-unbound daughter states, which themselves decay by emitting a proton. The proton decay occurs almost immediately, with half-life on the order of 10^{-17} s [1]. As a result, the intermediate daughter travels at most 2×10^{-12} m, which for the purposes of this experiment is negligible. Taking the resulting proton as originating from the same location and at the same time as the β-decay, it is easy to understand the effect on the proton energy spectrum as a Doppler energy spread about the mean proton decay energy.

Nuclide	Lifetime (ms)	E_p (MeV)	R_C (mm)
^{20}Mg	131.02	4.28	42.7
^{24}Si	202.74	3.91	40.8
^{28}S	180.37	3.70	39.7
^{32}Ar	145.00	3.36	37.8
^{36}Ca	147.19	2.55	33.0
^{40}Ti	75.60	3.73	39.9
^{48}Fe	65.36	1.23	22.9

Table 3.1: The $T = 2$ nuclei that will compose the initial experimental program measuring $a_{\beta\nu}$. The cyclotron radii, R_C, for the ejected protons of interest (having energy E_p) shown are calculated for the 7 T magnetic field of TAMUTRAP.

The initial program calls for measuring $a_{\beta\nu}$ for the $T = 2$, $0^+ \rightarrow 0^+$ superallowed β-delayed proton emitters listed in Table 3.1 by observing the proton energy spread as discussed above. The effect on the proton energy spread can be predicted by Monte Carlo simulation (to be discussed in greater detail in §3.3). Fig. 3.2 shows the expected experimental distribution of proton energies resulting from the $0^+ \rightarrow 0^+$ decay of ^{32}Ar. One can see the effect of $a_{\beta\nu}$ on the shape and width of the distribution around the mean proton energy of approximately 3.356 MeV. For $a_{\beta\nu} = 1.000$ (the value predicted by the SM), the β and neutrino are preferentially emitted in the same direction (see Eq. 2.23), and, as a result, impart the maximal momentum kick to the daughter, which is, in turn, inherited by the proton. This can be seen clearly in Fig. 3.2 as a greater energy spread about the proton's mean energy, when compared to the other cases. Logically, the spectra for $a_{\beta\nu} = 0.000$ and $a_{\beta\nu} = -1.000$ are each narrower in turn, since they correspond to a theoretical preference for the β and ν momentum vectors to be randomly aligned and preferentially anti-aligned, respectively.

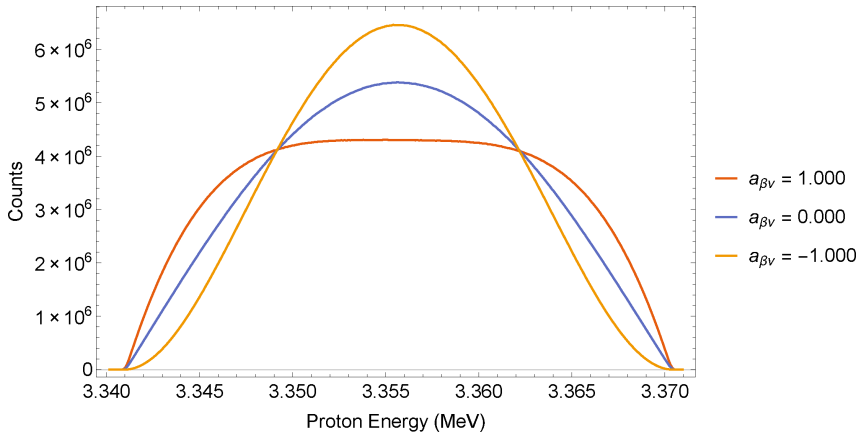

Figure 3.2: Proton energy distributions for the β-delayed proton decay of ^{32}Ar with $a_{\beta\nu} = -1$, 0, and 1. Each curve contains one billion events.

3.2 Ion Traps

In order to obtain the cleanest possible signal, the ions of interest should be isolated from background and initial motion should be limited to prevent unwanted Doppler broadening of the signal. In addition, high geometric efficiency for the protons of interest (yielding a larger signal) and collection of betas from the initial decay (to be used as a coincidence and to reduce systematics) are desired. To achieve this, `TAMUTRAP` plans to diverge from the foil implantation method employed by Adelberger et al. [1], opting to contain initial ions and decay products in a electromagnetic ion trap known as a Penning trap.

Ion traps of various types have been used with great success in a wide range of nuclear physics experiments, from precision mass measurements [8, 47, 9, 61] and purification of radioactive beams [31, 41, 30], to various decay studies [13]. The advantages of using ion traps for these purposes are many: in the presence of a buffer gas ion traps have the ability to reduce a particle's kinetic energy, the trapped particles exhibit well understood motion allowing for ultra-high precision measurements, and it is possible to design traps in such a way as to allow a very

open geometry for the placement of detectors and other experimental equipment. The TAMUTRAP facility has been designed to take advantage of all of these features. In particular a Radio Frequency Quadrupole (RFQ) Paul trap will be used to bunch and lower the emittance of the radioactive ion beam provided by T-REX. A mass purification stage based on a Penning trap is being investigated for purification of the incoming species. And, a novel open-geometry Penning trap will ultimately be employed for the precision measurement to simultaneously obtain a point-like, low-energy source of ions and contain decay products of interest.

3.2.1 The Penning Trap

A Penning trap is a type of ion trap that employs a well-shaped static electric field and a linear magnetic field to spatially confine charged particles in a small, well-known volume. Such a trap can be implemented using a variety of electrode geometries, most commonly in either a cylindrical or hyperbolic configuration, to determine the electric field that is used for axial confinement [21]. The magnetic field, which achieves the radial confinement of the ions, is typically generated by a solenoidal magnet in which the electrode structure is placed. For a quadratic electric field, the resulting ion motion in the trap given by Eq. 3.1, and is illustrated in Fig. 3.3 [7].

$$\begin{aligned} \omega_Z &= \sqrt{\frac{2QU_0}{Md^2}} \\ \omega_+ &= \frac{1}{2}\left(\omega_c + \sqrt{\omega_c^2 - 2\omega_Z^2}\right) \\ \omega_- &= \frac{1}{2}\left(\omega_c - \sqrt{\omega_c^2 - 2\omega_Z^2}\right). \end{aligned} \tag{3.1}$$

There are three eigenmodes for the micro-motion of a trapped ion in a Penning

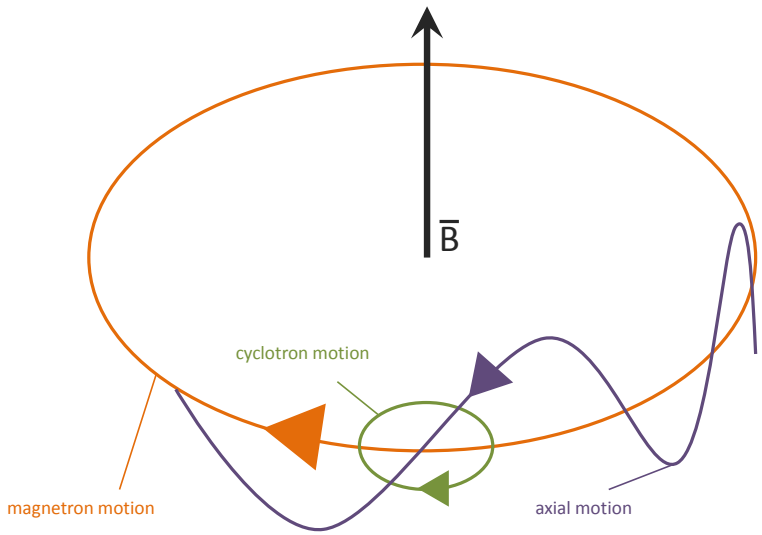

Figure 3.3: The three eigenmodes of motion in a perfect Penning trap.

trap, defined by their characteristic frequencies, given above. The axial frquency, ω_Z, depends on the charge and mass of the ion, Q and M, the depth of the quadratic electric potential, U_0, and the characteristic trap dimension, $d = \sqrt{\frac{1}{2}\left(z_0^2 + \frac{1}{2}\rho_0^2\right)}$ (here z_0 is the trap half-length, and ρ_0 is the inner radius). This axial motion is independent of the radial motions in a quadratic electric field. The two radial motions, dubbed the reduced cyclotron and magnetron motions, are characterized by their intrinsic frequencies, ω_+ and ω_-, respectively. These two motions, which are dependent only on the simple cyclotron frequency, $\omega_c = \frac{QB_0}{M}$ (here B_0 is the strength of the magnetic field) and the axial frequency, ω_Z, are inherently coupled. The specifics of the geometric shape of a Penning trap as it relates to the ion motion within will be revisited in Ch. 6.

Precision β-decay experiments are well served by a Penning trap ion source due to the fact that the magnetic field employed to trap the ions radially may simultaneously be used to contain charged decay products [32] such as β's and protons with up to 4π acceptance in an appropriately designed trap. The strong magnetic radial

confinement (confining charged particles in the MeV range) in combination with the weak electrostatic axial confinement (on the order of eV to hundreds of eV) direct the decay products of interest to either end of the trap for detection (Si detectors are envisioned) with negligible effect on the energy of the particles.

The natural Penning trap geometry requires a hyperbolic set of electrodes to generate the quadratic electric potential, U_0; however many modern traps take advantage of a cylindrical design. As will be discussed in Ch. 6, the cylindrical geometry can be modified to generate a nearly quadratic electric field, and, additionally, allows for more efficient access to the trapped ions (due to the option of having open-endcaps), a large trapping volume compared to the common hyperboloid trap geometry, and an electric field that can still be described analytically, which is of particular importance for optimizing the mechanical design. Additionally, cylindrical electrodes are more easily manufactured with higher precision, a result of the inherently cylindrical turning or milling machining techniques typically employed in fabrication [21]. At the same time, features of a cylindrical trap geometry can be useful for other nuclear physics experiments, such as maintaining a line of sight to the trap center for spectroscopy, an easily tunable and orthogonalized electric field for experiments requiring a harmonic potential (such as mass measurements), and unrivaled access to the trapped ions due to a geometry that does not require confining electrodes that follow the desired equipotential surfaces. For these reasons, Penning traps with a cylindrical geometry have been used widely in nuclear physics research experiments ranging from precision mass measurements [8, 47, 9, 61] to the production of anti-hydrogen [3], and it is this cylindrical geometry that has been chosen for the TAMUTRAP experiment.

As a result of the cylindrical Penning trap geometry, many aspects of the experimental procedure are simplified at TAMUTRAP. First, a small bunch of of ions (to be

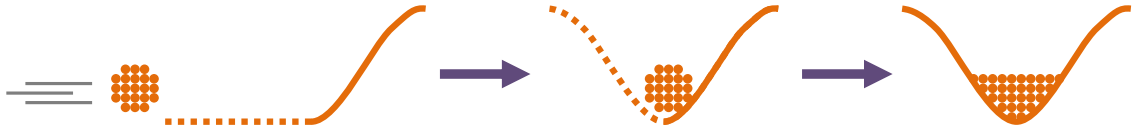

Figure 3.4: A cartoon indicating the method of loading the Penning trap. The potential on the injection side is lowered (left) until the ion bunch is approximately centered in the trap (middle), at which point the injection side potential is returned to its normal value, trapping the particles (right).

discussed more in §3.2.2) will be sent toward the Penning trap. The electric potential on the injection side of the trap will be lowered to allow the ions into the trap center. Once the ions are centered, these injection-side electrodes will be ramped back to voltage such that the ion bunch is trapped in the quadratic potential well. The injection procedure is depicted in Fig. 3.4. Though the physical bunch size is dictated by the time and energy spread of the original bunch, as well as the overall DC offset of the Penning trap relative to ground and specifics regarding the ramping of the injection-side voltages, the ultimate trapped ion cloud should be on the order of several mm in any direction, with an energy spread of several to tens of eV.

When a β-decay of interest is followed by the prompt proton decay, a β and proton (in addition to a slowly recoiling, low energy daughter and undetected ν) are emitted from the ion cloud, located at the trap center. Typical proton energies are listed in Table 3.1, while the β exhibits the traditional β spectrum with endpoint around 5 MeV. As both proton and β greatly exceed the eV scale of the axial confinement, these products easily escape the trap in the axial direction. However, the radial confinement can be quite strong, depending on the magnetic field strength, B_0. For $B_0 = 7$ T (the ultimate field strength to be employed at `TAMUTRAP`), the maximum cyclotron radii of the proton and beta motion can be calculated. In a trap with

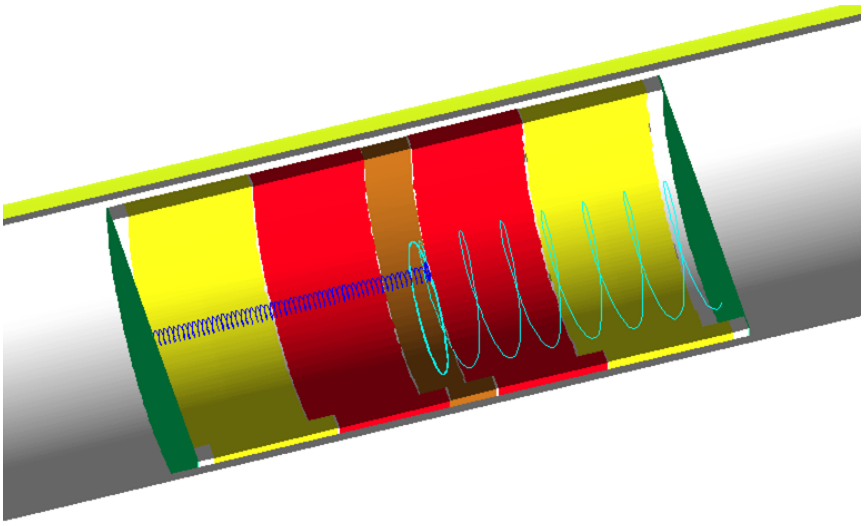

Figure 3.5: An initial GEANT 4 simulation of a decay of interest within the Penning trap geometry. Here, the teal track shows the motion of the emitted proton, while the blue track traces the path of the β.

inner radius larger than these maximum orbital radii, both the proton and β will observe helical orbits within the trap structure, progressing toward either end of the trap (depending on the sign of the axial component of their initial velocities). This can be seen in a GEANT 4 simulation of a sample decay of interest (Fig. 3.5). As a result, `TAMUTRAP` will be able to collect nearly all products[1] of interest with detectors located at either end of the trap.

3.2.2 The Paul Trap

In order to achieve a small effective trap size and low ion energy within the trapped ion cloud, a Penning trap requires bunched beam with minimal energy and time spread (*i.e.* low emittance, or what is referred to as a "cooled, bunched beam") as an input. To achieve this, some means of removing energy and shrinking the phase-space of the ion beam provided by T-REX is required. Another type of ion trap,

[1] All products of interest will be theoretically contained with the exception of those that escape through the entrance diaphragm of the trap.

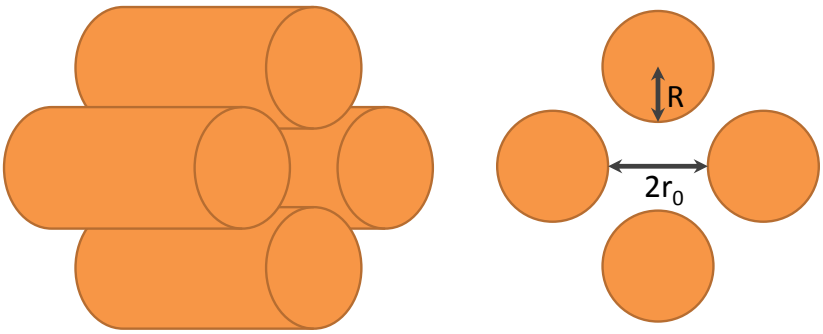

Figure 3.6: A simplified schematic of a linear quadrupole Paul trap employing cylindrical electrodes.

the Radio Frequency Quadrupole Paul trap [42], has proven to be an excellent tool for achieving both these goals when operated in the presence of a buffer gas [48, 55], and has been chosen for beam preparation at TAMUTRAP.

A Radio Frequency Quadrupole (RFQ) Paul trap employs an oscillating electric quadrupole field to achieve ion confinement [42]. Ideally, these fields are generated by a hyperbolic electrode structure operated at frequency Ω yielding the following general potential [7]:

$$\Phi = \frac{U_0 + V_0 \cos(\Omega t)}{2r_0^2}\left(r^2 - 2z^2\right), \tag{3.2}$$

where r_0 describes the scale of the hyperbolic geometry (physically, the half-distance between electrodes), r and z indicate the sampling point for the electric potential, U_0 is a DC potential offset, and V_0 is the oscillating trapping potential amplitude. In reality, however, a variety of electrode structures can be used to create a very good approximation of this geometry, with the linear Paul trap configuration employing four cylindrical parallel rods as seen in Fig. 3.6 to generate a two-dimensional version of this electric field being by far the most popular choice. In this case, it has been shown that setting the ratio of the cylindrical rod radius, R, to the half-distance

between opposite rods, r_0, to $R/r_0 = 1.145111$ yields a very good approximation of the field generated by the ideal geometry [35]. Such a linear Paul trap effectively supplies a rotating saddle-point quadrupole potential in two dimensions, which provides confinement along the trap axis for an appropriate trapping voltage and frequency.

The equations of motion, converted to two perpendicular dimensions, x and y, and including the time-dependent potential from Eq. 3.2, are [7, 55].

$$\begin{aligned} M\frac{\partial^2 x}{\partial t^2} &= -\frac{Q}{r_0^2}\left(U_0 + V_0\cos\left(\Omega t\right)\right)x, \\ M\frac{\partial^2 y}{\partial t^2} &= \frac{Q}{r_0^2}\left(U_0 + V_0\cos\left(\Omega t\right)\right)y. \end{aligned} \tag{3.3}$$

To solve these, it is convenient to make the following substitutions:

$$\begin{aligned} a &= 4QU_0/Mr_0^2\Omega^2, \\ q &= 2QV_0/Mr_0^2\Omega^2, \end{aligned} \tag{3.4}$$

which yields what are referred to as the Mathieu equations [7, 55]:

$$\begin{aligned} M\frac{d^2 x}{dt^2} &= -\frac{\Omega^2}{4}\left(a + 2q\cos\left(\Omega t\right)\right)x, \\ M\frac{d^2 y}{dt^2} &= \frac{\Omega^2}{4}\left(a + 2q\cos\left(\Omega t\right)\right)y, \end{aligned} \tag{3.5}$$

Here, Q and M are the charge and mass of the ion, and, again, U_0 is the DC potential offset of one set of electrodes, V_0 is the oscillating trapping potential amplitude, Ω is the trapping frequency, and r_0 is the half-distance between opposite rods. The

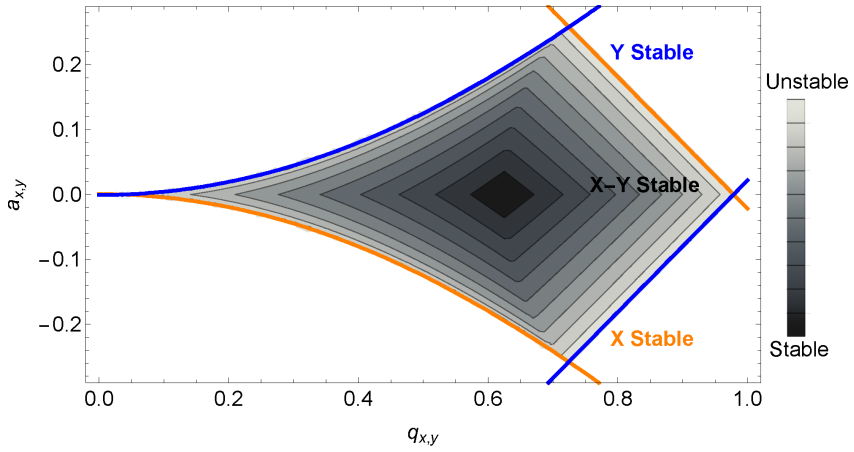

Figure 3.7: A contour plot highlighting regions of stable ion motion in a Paul trap. The overlapping area in the center represents stability in both principle directions.

solution to these equations, which is discussed in detail in [44], is given by:

$$u(\zeta) = B_1 e^{\mu\zeta} \sum_{n=-\infty}^{\infty} C_{2n} e^{2in\zeta} + B_2 e^{-\mu\zeta} \sum_{n=-\infty}^{\infty} C_{2n} e^{-2in\zeta}, \tag{3.6}$$

where $\zeta = \Omega t/2$, B_1 and B_2 depend on the initial conditions, and C_{2n} and μ depend on the geometry and operating parameters of the device, *i.e.* a and q. A careful analysis of this solution suggests that stable periodic motion can only be achieved if and only if μ is a purely imaginary, real non-integer, as discussed in [7, 48]. Since μ depends only on the geometry and operating parameters of the device through a and q, one can determine values of a and q that generate such a value for μ, and, therefore, bring about stable trapped motion. The values of a and q that accomplish this are known as stability regions, and a subset of these are shown in Fig. 3.7 [48]. As will be discussed in Ch. 5, the TAMUTRAP RFQ will be operated at $a \approx 0$ and $q \approx 0.5$.

In a linear, 2 dimensional Paul trap, the axial confinement can further be aug-

mented by the superposition of a electrostatic potential well along this same axis, returning 3 dimensional trapping. Once ions are fully trapped in 3 dimensions, they may be cooled through collisions with a low-mass buffer gas, typically Helium [26]. Collisions with gas molecules (which, on a large scale appear as a resistive or viscous damping force) transport net energy from the ions to the buffer gas, which is ultimately removed from the system through pumping. In so doing, the accessible phase space of the beam is reduced. This is referred to as "cooling" the ions, and, as a result of the process, the ions collect in the lowest energy region of the trap at the axial potential minimum, forming a tight bunch. In the long time limit (which is effectively attained after several ms depending on ion mass and charge, buffer gas selection, etc.), the ions achieve thermal equilibrium with the surrounding buffer gas and cannot be cooled further. This results in a thermal kinetic energy of around 40 meV for a room temperature buffer gas.

While the thermal energy of the cooled beam is quite low, there are other effects that contribute to the final kinetic energy of the ejected bunch (as well as its deviation about the mean). One of these is the method of ejecting the ions, to be discussed in Ch. 5. Any irregularities in the procedure of lowering the ejection barrier, such as higher-frequency transients on the dropping potential, may increase the beam energy for some or all of the trapped ions. Since the ion bunch is not point-like, *i.e.* it occupies a finite amount of space, any spatially dependent component of the ejection potential is likely to induce some energy spread in the resulting bunch. These factors have been studied empirically, and the results are presented in Ch. 5 and Appendix A.1.

A better understood factor that arises to increase ion energy above the thermal limit is due to space-charge effects, or the Coulomb repulsion between trapped ions. Space-charge effects can play a large role in the ultimate bunch size and trap capacity

depending on the incoming beam current. It can be shown that the maximum theoretical ion density due to the competing Coulomb and confining forces for trapped, singly charged ions is given by [48]:

$$\rho_{\max} = \frac{\epsilon_0 \pi^2 \Omega^2 q^2 M}{e^2}, \tag{3.7}$$

where ϵ_0 is the vacuum permitivity, Ω is the trapping frequency (for single ions, this is in the MHz range) and q is given in Eq. 3.4, and is a function of trapping parameters and geometry. Here M is the mass of the ion of interest, and e is the electron charge.

The maximum number of ions included in a bunch can then be approximated by,

$$N_{\max} = \rho_{\max} \frac{4}{3} \pi u_{\max}^3, \tag{3.8}$$

where u_{max} is the trapped ion bunch size in one dimension. In this way, an empirical observation of the number of ions contained in the ultimate ion bunch can be used to give an estimate of the physical trap size. This result will be explored further in Ch. 5.

Through the application of these two varieties of ion trap, a Penning trap to capture and measure decay products of interest, and a Paul trap to prepare ions for use in the Penning trap, the TAMUTRAP experiment will observe proton energy spreads with very high geometric efficiency to be used for investigation of $a_{\beta\nu}$, and, in so doing, the SM. The next chapter, Ch. 4, will discuss how these elements have been physically arranged in the TAMUTRAP experiment to best perform their duties.

INPUTS	OUTPUTS
Parent Z	Proton energy
Parent A	Proton direction
Parent mass excess	β energy
Intermediate product mass excess	β direction
Intermediate product excitation energy	ν energy
Final product mass excess	ν direction
C_X, $X = S, V, T, A, P$	Recoil properties

Table 3.2: The inputs and some frequently used outputs for the Monte Carlo simulation of the decays of interest.

3.3 Decay Simulations

In order to obtain a preliminary understanding of the sensitivity and statistics necessary to measure $a_{\beta\nu}$ by the proposed method, a first-pass data analysis was performed using simulated events generated by a Monte Carlo method developed in C++. This method, was designed to confirm the expected experimental signal, and to search for enhanced sensitivity through various measurement techniques. A more rigorous GEANT4 simulation is planned [54], and will be used for further validation of the proposed experimental setup.

3.3.1 Monte Carlo Method

The Monte Carlo method used to model the $T = 2$, $0^+ \rightarrow 0^+$ superallowed β-delayed proton decays of interest embodies the full physics of the weak interaction as described in [28] and [29]. All physically possible currents are allowed, not just the $V - A$ process required by the SM. A list of the inputs and outputs for the routine can be found in Table 3.2.

For each decay event, separate and uncorrelated random directions are assigned to the parent ion (assuming non-zero initial parent velocity), the β, and the ν. The energy of the β particle is determined by randomly choosing an energy between

0 and the maximum allowed kinematic energy of the β, which is calculated via the mass difference of the parent, daughter, and β, taking into account decays to excited states. The ν, which is considered massless for this purpose, is assumed to be generated simultaneously with the production of the daughter and β, resulting in three bodies at the decay point. The ν energy is the difference of the maximum allowed β energy and the randomly assigned β energy. As a result, the daughter is assumed to take no *energy*, which is a good first order approximation suitable for this purpose, as the daughter in reality can only take a *maximum* of around 500 eV; however, some recoil order corrections are included in the calculation of the decay rate, as will be discussed. Once the β and ν energies are assigned, the intermediate daughter product's velocity and direction is completely determined by conservation of momentum. These three particles are then shifted back to the lab frame for ease of future calculations.

The proton decay is assumed to take place instantaneously after the initial β-decay (again, its half-life is on the order of 10^{-17} s). First, the proton is assigned a random direction in the daughter reference frame, and its energy is calculated via the mass excess of the decaying intermediate daughter. The kinematics of the second daughter are then completely determined in the intermediate daughter frame due to conservation of momentum (a 2-body problem). The resulting products are once again shifted back to the lab frame for ease of calculations.

After all the kinematics of the four resulting products (final daughter, β, ν, and proton) are determined in this way, the event is either accepted or rejected based on the outcome of a random number being compared to the decay cross section,

including lowest order kinematic recoil terms (Eq. 3.9) as in [28, 29, 1].

$$\frac{d^3\omega}{dE_e d\Omega_e d\Omega_\nu} \propto \frac{F\left(Z,p_e\right)}{\left(2\pi\right)^5} p_e E_e \left(E^0 - E_e\right)^2 \xi \times \left(1 + \frac{p_e}{E_e} a_{\beta\nu} \cos\theta_{\beta\nu} + b\frac{m_e}{E_e}\right)\left(\frac{M_f}{M_i - E_e - p_e\cos\theta_{\beta\nu}}\right). \tag{3.9}$$

Here, again, $F\left(Z,p_e\right)$ is the Fermi function; E_e, E^0, p_e, and m_e are the energy, maximum available energy, momentum, and mass of the β; E_ν is the energy of the ν; M_i and M_f are the masses of the parent and daughter nuclei; $a_{\beta\nu}$ and b are the correlation parameters (as in [28]); and $\theta_{\beta\nu}$ is the angle between the β and ν. The decay rate remains reported as a proportionality since normalization is not required for the Monte Carlo technique as long as the entire amplitude of the decay rate is probed.

Before running the simulation, a collection of events are generated to determined the normalization of the decay cross section, which is subsequently multiplied by a safety factor to ensure that the entire amplitude of the decay cross section is tested by the code. For any subsequent event, a random number is generated between 0 and this maximum amplitude of the decay cross section. The value is compared to the calculated cross section for the particular generated event in order to determine if it should be kept or discarded. When the randomly generated number is less than the calculated cross section for the event, the event is recorded, otherwise the event is discarded. The entire process is then repeated for the desired statistics.

The data is histogrammed on-line, event-by-event, and periodic output for given statistics can be specified. These results include the entire set of kinematic information for each of the involved particles relative to the lab reference frame, which allows for the examination of many different detection schemes. Recently, [1] has exclusively used the shape of the proton energy distribution to determine the cor-

relation parameter $a_{\beta\nu}$; however more complicated analyses, such as those involving the direction of the β are also available with the Monte Carlo outputs. The effect of $a_{\beta\nu}$ on the simple proton energy distribution as predicted by the Monte Carlo code has been shown in Fig. 3.2.

3.3.2 Exploring Analysis

The output of the Monte Carlo was employed for preliminary investigations into data analysis and in order to determine a rough limit on the required statistics necessary for various precisions on the measurement of interest. One billion events were generated for $C_S = C_S'$ values of 0.000, 0.005, 0.010, 0.015, 0.020, and 0.025, with output increments at 100,000 events (here $C_V = 1$, and $C_X = C_X'$ assumes maximum parity violation as discussed in [51]). The proton energy spectra were histogrammed on-line using energy bins of width 500 eV [1]. During histogramming, an approximation of detector energy resolution was optionally implemented by throwing a Gaussian random number with mean equal to the accepted proton energy and deviation equal to the hypothetical detector resolution, and placing the event in the corresponding energy bin. Perfect energy resolution and 3 keV energy resolution [1] were investigated. The resulting data files were analyzed in Mathematica [64].

Analysis was performed around the standard model predictions of $C_S = 0$ and $C_V = 1$, corresponding to $C_S/C_V = 0$. The current best value reported in the literature restricts $C_S/C_V < 2.4 \times 10^{-3}$, once again assuming maximum parity violation [25] (without the assumption of maximum parity violation, the current experimental limit is $C_S/C_V = C_S'/C_V < 0.065$). As a result, Monte Carlo outputs for $C_S = C_S' = 0$ with varying statistics were compared to "reference" sets of $C_S = C_S' =$ 0.000, 0.005, 0.010, 0.015, 0.020, and 0.025, each containing 1 billion events. The "reference" sets were normalized to the statistics of the each set, and a χ^2 analysis

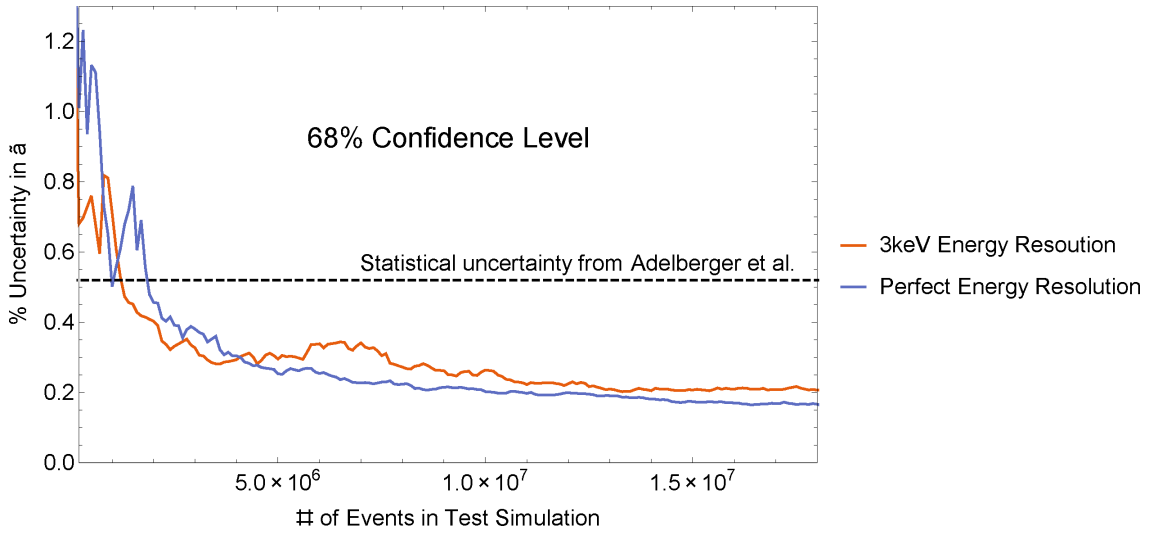

Figure 3.8: 68% statistical confidence level on $\tilde{a}$ (Eq. 3.10) about $\tilde{a} = 1$ for the $0^+ \to 0^+$ superallowed β decay of ^{32}Ar as a function of statistics (number of events in the test Monte Carlo). The dashed line represents the experimental sensitivity achieved by [1].

was performed.

For the purpose of comparison, the input C_S values were transformed into values of $\tilde{a}$, a quantity typically reported in the literature for these measurements [1, 25, 24]. For the β decay of interest from ^{32}Ar, $\tilde{a}$ is given by [1]:

$$\tilde{a} = \frac{a_{\beta\nu}}{1 + 0.1913b}, \tag{3.10}$$

where, b is the Fierz term. The unreduced χ^2 was fit by a quadratic as a function of $\tilde{a}$ for each amount of statistics. To extract the uncertainty in the measurement for the given statistics, the fitted curve was used to determine the change in $\tilde{a}$ needed to effect an increase of 1 in unreduced χ^2, corresponding to a 1σ (68% confidence level) deviation from the observed value. The resulting achievable statistical uncertainty in $\tilde{a}$ is plotted as a function of the statistics of the test set in Fig. 3.8.

Fig. 3.8 indicates that a 1σ statistical uncertainty in a measurement of $\tilde{a}$ about the value $\tilde{a} = 1$ of approximately 0.5% may be made with 2 million events, which agrees nicely with Adelberger et al. who observed $\tilde{a} = 0.9989 \pm 0.0052$ with approximately 2 million events, corresponding to a percent uncertainty of 0.52%.

This is only a first look at data analysis. Two changes will be taken into account in the future. First, a more detailed simulation of the experimental setup will be performed with GEANT4 to generate more physically realistic data. And, second, additional experimental observables and analysis techniques will be explored. In particular, the TAMUTRAP facility will obtain kinematic information for the β in the decays of interest, which may then be used to clean the proton energy spectrum via imposing coincidence conditions, and also for enhancing sensitivity. Sensitivity enhancements are expected by breaking the data into events in which the proton and β are emitted in the same hemisphere in the lab versus events in which these particles are emitted in opposite hemispheres, and fitting resulting proton energy spectra individually. While these two improvements to the analysis scheme will allow a more accurate measurement with less uncertainty, experimental attenuating factors such as noise, apparatus systematics, backgrounds, etc., will make the measurement more difficult in reality. In the end, it is expected that uncertainties achieved at TAMUTRAP should be a significant improvement over the measurement made by Adelberger, et al. due to a similar event rate with an advancement in detection scheme and an increase in event observables.

4. THE TAMUTRAP BEAM LINE

The beam line at the TAMUTRAP facility serves to prepare and transport the radioactive ion beam from the heavy ion guide (a part of the T-REX upgrade project to be discussed in §4.1.1) to the measurement Penning trap system, and will employ an entirely electrostatic ion guiding scheme, excluding the RFQ cooler and buncher. Electrostatic ion guides provide comparable performance to magnetic systems at low beam energies, and are significantly less expensive to fabricate and operate. Since the majority of the Texas A&M University Cyclotron Institute utilizes magnetic beam transport elements, existing designs could not be relied on, and a great deal of work was required to develop new electrostatic beam elements for the TAMUTRAP facility.

4.1 Overview

The TAMUTRAP beam line, presented schematically in Fig. 1.1 and rendered in Fig. 4.1, includes all elements necessary for transporting the radioactive ion beam past three 90° bends, around 11 m of vacuum chamber, and through the cooling and bunching RFQ Paul trap to the measurement station, which houses the precision Penning trap.

Electrostatic elements are utilized wherever possible to achieve the focusing, steering, and deflecting necessary for high-efficiency beam transport. The T-REX project [56], to be discussed in more detail in §4.1.1, will supply a 10 keV ion beam of the desired species. This 10 keV beam will travel through focusing lenses and steerers (which will be discussed in the coming sections) referenced to earth-ground. After covering approximately 7 m, the beam decelerates onto a high voltage platform held at slightly less than 10 kV. The decelerated ion beam, having a kinetic energy on the order of tens of eV, is injected into the RFQ for bunching and a reduction

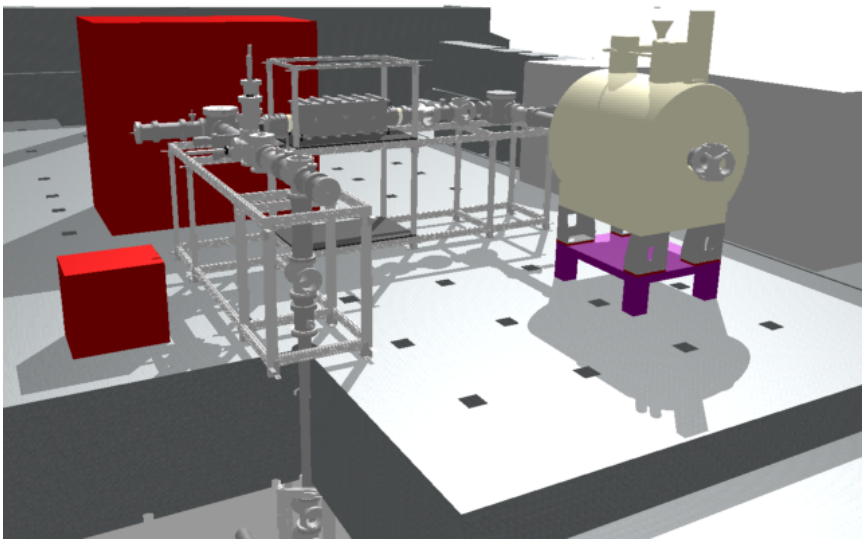

Figure 4.1: A rendering of the entire TAMUTRAP experiment.

of the ion beam's phase space as discussed in Ch. 3. Once bunched, the beam is ejected from the RFQ and re-accelerated to nearly 10 keV by returning to an earth-ground referenced beam pipe. The ion bunch is then guided farther by the same electrostatic techniques, with the addition of two pulsing cavities designed to lower the beam energy to the eV range for acceptance by the measurement trap. Beam line elements prior to the bunching stage are operated in a steady-state mode, while some of those following the bunching stage, such as the pulsing cavities, are required to be operated periodically. Periodic operation is governed by a fast FPGA-based control system and software. Both, continuous and bunched beam transport is observed via diagnostic stations based on MCP and Faraday detectors at various locations.

4.1.1 T-REX Upgrade and the Heavy Ion Guide

The Texas A&M Re-accelerated Exotics upgrade program, known as T-REX [56], will provide the isotopes of interest for the TAMUTRAP experiment, and is depicted in Fig. 4.2. T-REX employs the K150 (88 inch) cyclotron at the Texas A&M University

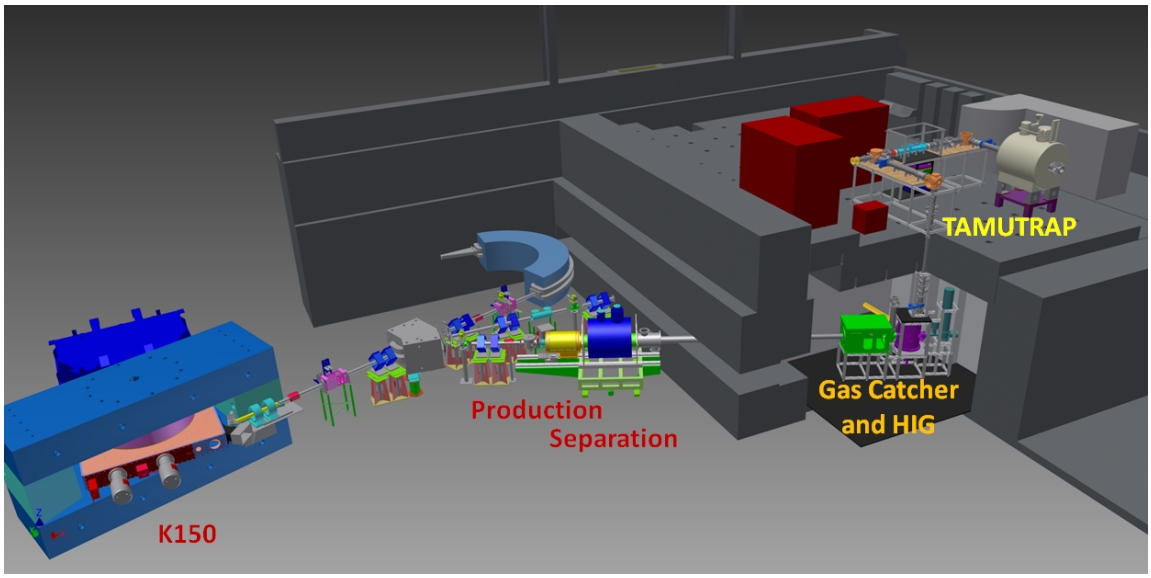

Figure 4.2: A rendering of the T-REX project connected to the TAMUTRAP facility. Various stages in beam production are highlighted.

Cyclotron Institute to accelerate various primary beams to energies on the order of 20 MeV/u. These primary beams are first generated by an Electron Cyclotron Resonance (ECR) type ion source, where the species of interest is injected into a microwave cavity in a gas phase. In the ECR, the gas is bombarded with microwave energy, creating a plasma and stripping electrons off the originally neutral atoms. This process, known as charge-breeding, yields highly charged ions of the species of interest, which are subsequently injected into the center of the K150 cyclotron. The K150 cyclotron accelerates these highly charged ions from the keV level to tens of MeV before extraction. Expected production rates calculated by Souliotis, et al. are listed in Table 4.1.

The resulting primary beam can then be directed to a target of choice in order to create the secondary radioactive ion beam, or RIB. In order to generate the RIBs of interest to TAMUTRAP, a light gas target will be employed to facilitate fusion evaporation reactions, which have been calculated to exhibit the largest production

Species	Energy (MeV/u)	Intensity (pμA)	Species	Energy (MeV/u)	Intensity (pμA)
p	55	27	^{20}Ne	28	3.0
d	35	21	^{22}Ne	29	0.5
^{3}He	45	11	^{34}S	20	0.7
^{4}He	35	10	^{40}R	17	1.4
^{6}Li	35	7	^{40}Ca	17	1.5
^{7}Li	25	8	^{59}Co	11	0.9
^{10}B	35	4	^{78}Kr	10	0.6
^{11}B	29	4.7	^{86}Kr	8.3	0.6
^{16}O	35	2.3	^{129}Xe	5.6	0.5

Table 4.1: The production capabilities of the K150 cyclotron in combination with ECR ion source according to [56].

cross-sections [54]. The gas target chosen for these reactions is ^{3}He, which should yield the greatest production rates for ions of interest. The theoretical rates are listed in Table 4.2 [54].

Since the projectile is in motion and is rather heavy compared to the stationary, light target[1], the reaction causes a very forward-focused beam containing the RIB of interest in addition to a great deal of isobaric and other mass contamination. The resulting secondary beam will be cleaned according to m/q ratio via the BIGSOL 7 T superconducting magnet, which will be placed slightly downstream of the interaction point. Since ions resulting from interaction with the target will be deflected off-axis by some amount in the collision process, mass selection may be made through a series of annular and lollipop-style collimators. As a result of varying reaction energy, each product exhibits a mean deflection angle, and, in this way, a characteristic ratio of axial to transverse momentum. The transverse components of ion momentum are converted to periodic radial motion via the cyclotron force in the BIGSOL magnet, and return to the beam axis after some travel distance depending on their mass

[1]This is referred to as an inverse kinematics reaction.

RIB	Projectile	Beam Energy (MeV/u)	Approximate Rate (pps)
^{40}Ti	^{40}Ca	17	7.0×10^4
^{36}Ca	^{36}Ar	20	2.5×10^5
^{32}Ar	^{32}S	20	1.4×10^5
^{28}S	^{28}Si	20	1.5×10^5
^{24}S	^{24}Mg	20	6.5×10^4
^{20}Mg	^{20}Ne	21	1.4×10^5

Table 4.2: Theoretical production rates for ions of interest via fusion evaporation reactions with ^{3}He [54].

and initial longitudinal and transverse velocities. As the product of interest is at its maximal radial position, an on-axis lollipop-style beam blocker is used to remove the remaining primary beam and contaminants with low transverse energies. Next, a tight annular, or CD-shaped collimator can be placed at the location downstream of the interaction point where the ions of interest first return to the beam axis due to the cyclotron motion imposed by BIGSOL's magnetic field. In this way, the desired ions pass through the collimator on-axis, while many other species that have either different masses or initial transverse energies are removed. This method is estimated to produce a mass resolution, $m/\delta m$ of several hundred, though ultimately there will be a trade-off between increasing mass resolution and overall efficiency.

After mass purification in BIGSOL, the MeV energy beam needs to be de-accelerated in order to be useful for charge breeding (after which it can be re-accelerated in the new K500 cyclotron) or so that it can be used directly by experiments such as `TAMUTRAP`. To achieve this, the purified RIB is caught in an Argonne-style gas-catcher [49] sitting on a 10 keV high voltage platform, where it will initially be stopped and thermalized in a helium atmosphere of about 200 mbar pressure. Within this device, the ions are guided by three forces: a net repulsive RF force on the walls that prevents neutralization, a linear drag potential that guides the ions

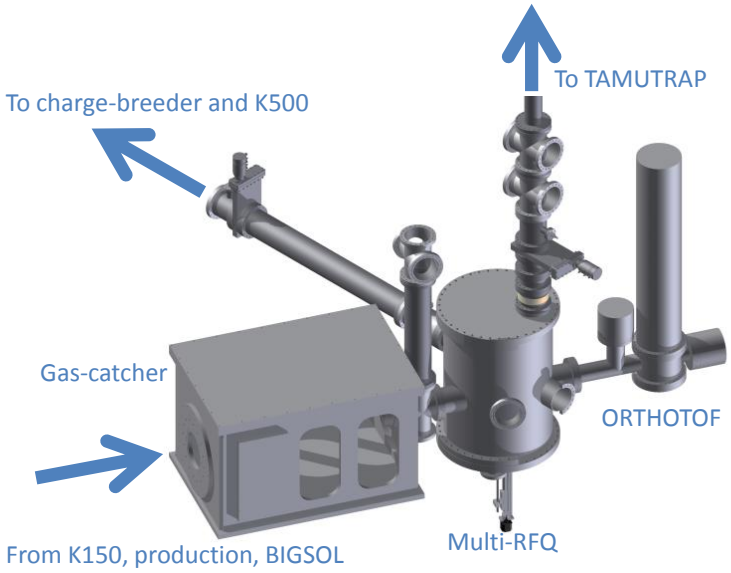

Figure 4.3: An annotated view of the T-REX gas-catcher and multi-RFQ.

toward the exit of the gas catcher, and a axial force due to gas flow that becomes significant near the small exit aperture. After spending a few ms in thermal contact with the Helium buffer gas, the ions are extracted via the nozzle into a multi-RFQ switch yard. This switch yard allows delivery of the beam to one of three locations: the charge breeder as the next step to making a re-accelerated beam, an ORTHOTOF mass spectrometer for characterization, or the TAMUTRAP beam line, as in Fig. 4.3. All beam lines after the multi-RFQ switch yard are earth-ground referenced, endowing the ions with a 10 keV beam energy.

4.2 Beam Line Simulation

The first step toward developing the beam line design shown in Fig. 4.1 required a theoretical look at what components would be necessary for beam transport from the T-REX multi-RFQ to the final location of the TAMUTRAP measurement Penning trap. Lead by Dr. Praveen Shidling, SIMION was used to determine the optimum

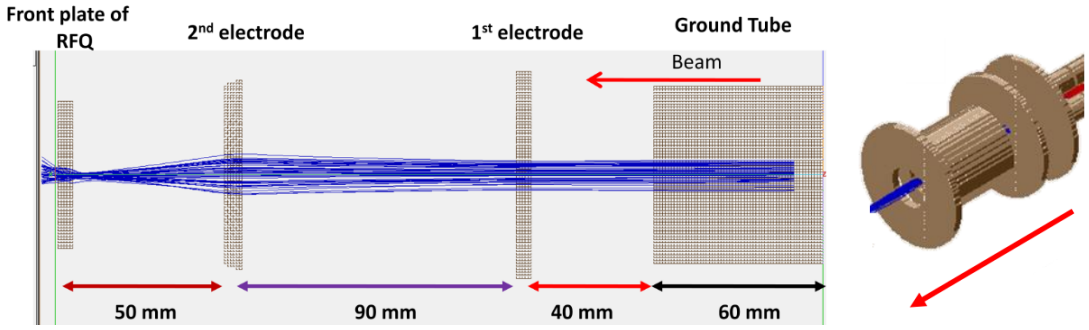

Figure 4.4: The injection optics for the RFQ (left) and the extraction optics (right).

placement and characteristics of various focusing and deflecting elements. Great care was taken to achieve very high efficiencies, especially in areas requiring large electric field gradients, such as the injection and extraction optics of the RFQ, and areas employing dynamic electric potentials, such as the RFQ structure itself or the subsequent pulsing cavities.

Through optimization in SIMION, the structure and placement of Einzel lenses and beam steerers was established in order to ensure efficient beam transfer such that the beam envelope was able to remain small relative to the cross-section of the vacuum chamber. This was achieved by inputting the predicted beam properties at the exit of the multi-RFQ, and tweaking inter-element spacings so that the beam remained well collimated during simulated transport. The ideal spacing between Einzel lenses was determined to be approximately 2 m, though tweaking of the lensing potentials can account for some required deviation from this value. It was decided to pair beam steerers with every lens in order correct for fabrication and alignment imperfections.

Next, the injection and extraction optics, the focusing elements before and after the RFQ structure, were modeled in SIMION with the goal of achieving maximum efficiency during de-acceleration and re-acceleration of the 10 keV ion beam. Again,

this work was lead by Dr. Praveen Shidling, and resulted in the structures seen in Fig. 4.4. The 3-element injection optics yields nearly 100% transport in decelerating the simulated beam from 10 keV to 10-100 eV; however some small losses are encountered in simulation when coupling to the RF structure of the cooler/buncher. The resulting injection optics is composed of three electrodes: a ground tube, a 32 mm inner diameter first electrode, and a 28 mm inner diameter second electrode. The extraction optics were optimized in a similar fashion and are composed of three electrodes: two 6 mm long and one 50 mm long cylinders all with 26 mm inner diameter and separated by 5 mm.

SIMION was also used to simulate the performance of the RFQ in cooling and bunching mode, and to determine the configuration of pulsing cavities needed to lower the beam energy. To do this, a user program was implemented to add a hard-sphere based gas collision routine to the observed ion motion due to the electrode structures of the device. As a result, the simulations included cooling and bunching of the incoming ion beam. Once cooled in simulation, the ions were ejected through the optimized extraction optics and were sent toward a drift tube. The subsequent time of flight of the ions was analyzed in order to determine an appropriate length and position for the drift tube such that pulsing a 1.2 μs bunch would be easily possible. The resulting optimized drift tube structure is 400 mm long with a 30 mm inner diameter. A screen shot of the simulation used to ensure the theoretical functioning of the RFQ and associated optics, including the aforementioned pulsing cavity can be seen in Fig. 4.5.

4.3 Basic Components

After optimizing ideal element spacing and design and ensuring the theoretical functioning of the RFQ in SIMION, realistic mechanical designs were generated for

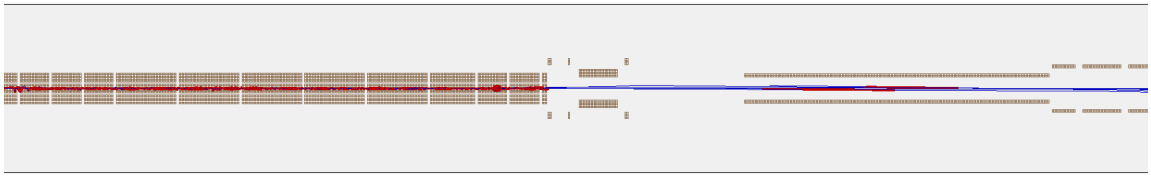

Figure 4.5: The RFQ (left), extraction optics (center), and pulsing cavity (right) as simulated in SIMION. Here 50 ions are being cooled, ejected, accelerated to 10 keV, and, finally, pulsed to 3 keV energy.

the TAMUTRAP facility. In general, electrodes have been precisely fixed to adjacent flanges, such that the alignment procedure for the resulting structure is completed by alignment of the flange centers; however, some elements with specifically stringent alignment requirements, such as the injection and extraction optics, have been designed to allow fine tuning of the electrode position separate from the mounting flanges.

The vacuum chamber has been designed to employ 8 in. ConFlat (CF) flanges for typical beam-pipe connections, and 2.75 in. CF flanges for various feedthroughs and measurement ports. The 8 in. CF requires a 6 in. outer diameter beam pipe, which provides a good compromise between pumping speed and cost. The entire Texas A&M University Cyclotron Institute has been transitioning to this setup for several years. Vacuum is currently provided by two 1000 L/s Leybold turbomolecular pumps, each backed by dry scroll roughing pumps, eliminating any concerns of oil contamination from the system. With the present system (to be discussed more in Ch. 5), pressure is better than 10^{-7} mbar, even with several Viton gaskets in place of copper seals at frequently opened flanges. When complete, the beam line will require four similar capacity turbo pumps (one at each end of the RFQ, one in the line following T-REX and one before the measurement trap), all backed by oil-free roughing pumps. Additional pumps may ultimately be required to obtain long enough trap lifetimes in the measurement trap and to reduce collisional beam

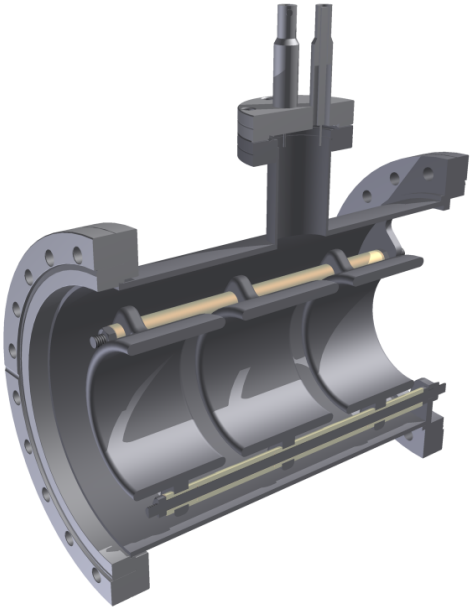

Figure 4.6: Cross-section of a TAMUTRAP Einzel lens with three adjustable electrodes.

spread immediately before or after the RFQ, but this needs to be established with further testing (see Ch. 5).

The vacuum chamber support structure is constructed from solid-core 1.5 in. 8020 aluminum extrusions, which exhibit minimal deflection at the loads typically encountered on the TAMUTRAP beam line. An important consideration for the support structure is the inclusion of some means of aligning the vacuum chamber once it is in place. The vacuum chamber support structure allows for the previously mentioned alignment method of centering flanges on an optical axis via three 1/2-13 set screws at various positions along the beam line. Due to machining and welding imperfections, flanges are not typically perpendicular to the beam pipe on which they are mounted. As a result, a common deviation from the optical axis on the order of 5-10 mm can be observed before alignment.

Einzel lenses for the TAMUTRAP facility were designed to allow for a large beam

Figure 4.7: A view of the floating pulsing cavity.

envelope, and to handle high electrode voltages. Two designs have been created, one with grounded end electrodes, and one with adjustable end electrodes for finer control of the beam profile (shown in Fig. 4.6). Both structures employ a 50 mm inner diameter, with 46 mm length outer electrodes and a 56 mm inner electrode separated by 9 mm. All edges have been radiused to minimize sparking, ceramic insulators have been custom machined for good electrical isolation, and the connectors have been specified to handle 20 kV where needed.

Beam steerers for TAMUTRAP are one of the few elements that utilize an existing Texas A&M University Cyclotron Institute design, which has been modified to be permanently aligned with the mounting flange. In this way, the steerers may be aligned in the same fashion as many other beam elements. In the current TAMUTRAP beam line, a steerer is paired with each Einzel lens.

The pulsing cavity, which employs a 400 mm drift tube, has been designed as a floating element able to sit at any free location within the beam line. The support structure consists of three semi-circular legs that can be placed arbitrarily along

the length of the electrode, and are held in place via set screws. Since the drift tube ideally imposes no lensing on the beam (the entering beam sees only a wall of charge due to the flat front face as in Fig. 4.7, and the exiting beam sees only ground), alignment is slightly less critical in this application, which permits the flexible design. The movable structure allows the position of the drift-tube entrance to be tweaked as needed for timing considerations, and additionally does not require a dedicated mounting flange, which is convenient in the crowded section of beam pipe immediately following the RFQ.

The high voltage platform on which the RFQ cooler/buncher sits has been designed in concert with technical staff of the Texas A&M University Cyclotron Institute. The structure has been assembled from the same 8020 extrusions as the adjacent beam line. This support is surrounded by a Faraday cage with interlocked doors, both of which are tied to earth-ground. Electrical insulation for elements held at high voltage is achieved through the use of 1/2 in. thick chemical-resistant poly-vinyl chloride, or PVC, which is backed by particle board for increased structural rigidity. The floating section of the beam line is separated from the adjacent grounded sections by custom 4.5 in. CF ceramic breaks located at each end. Power is supplied through a center-tapped 15 kW, 20 kV isolation transformer. The center tap on the floating side dictates the floating potential, and is set by a 20 mA, 15 kV Spellman high voltage supply. Communication to devices on the high voltage platform is carried out over either USB or TCP/IP, both mediated by optical fiber. The gas supply for the RFQ cooler/buncher is located at ground, and is provided to the electrically controlled valve (to be discussed more in Ch. 5) via a non-conductive gas line.

Many power supplies are required for operation of the electrostatic beam optics that compose the `TAMUTRAP` beam line. Voltages that are rarely adjusted, such as

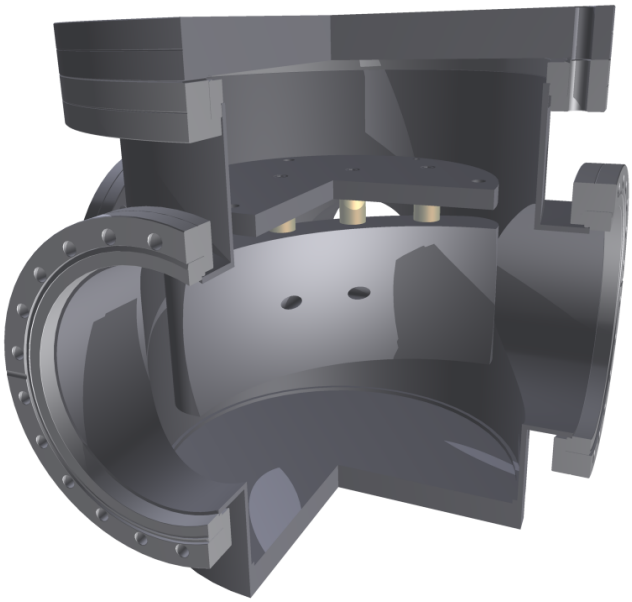

Figure 4.8: A three-quarter section view of the spherical deflector. The inner surface is omitted for clarity.

those provided to the first Einzel lens, the high voltage platform, and the ion source, are supplied by manually adjustable Spellman supplies. The remainder of the beam line is operated by ISEG low and high voltage modules that are either standalone or located in Weiner MPOD crates. These supplies were chosen for their low-ripple output claims, ease of control, and low cost. The control system used to manipulate these supplies will be discussed in §4.7.

4.4 Deflectors

The three 90° bends in the TAMUTRAP beam line were required to allow sufficient room for the RFQ cooler/buncher outside of the stray magnetic fields of the 7 T magnet employed by the Penning trap. An electrostatic deflector with spherical shaped electrodes is the ideal means of bending a beam electrostatically. Since the ideal electric field gradient generated by this structure is completely in the radial di-

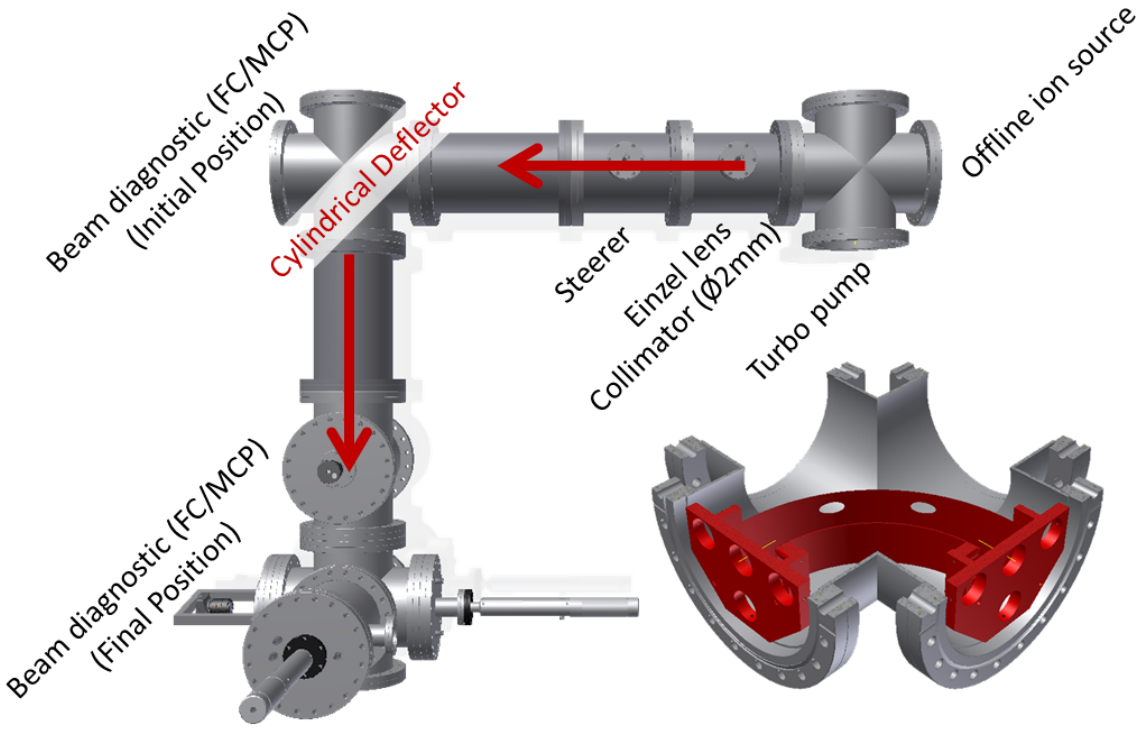

Figure 4.9: The cylindrical deflector and a test beam line used for its characterization.

rection, the beam theoretically suffers no transverse-position-dependent aberrations during bending.

Such a spherical deflector has been developed for use at TAMUTRAP, as pictured in Fig. 4.8. This device, which employs a 260 mm radius of curvature for the beam, has been shown to exhibit approximately 100% transmission efficiency for beams with transverse dimensions less than 1 in. It also features 10 mm on-axis through holes in the outer electrode to allow line of sight to the beam axis, and to allow straight-through transmission when the electrodes are held at ground. The structure is fixed to a 13.25 in. CF top flange of a custom chamber, and is machined for correct alignment.

Despite the high efficiency and expected regularity of the beam profile after bending, the spherical deflector poses some drawbacks to widespread implementation. In

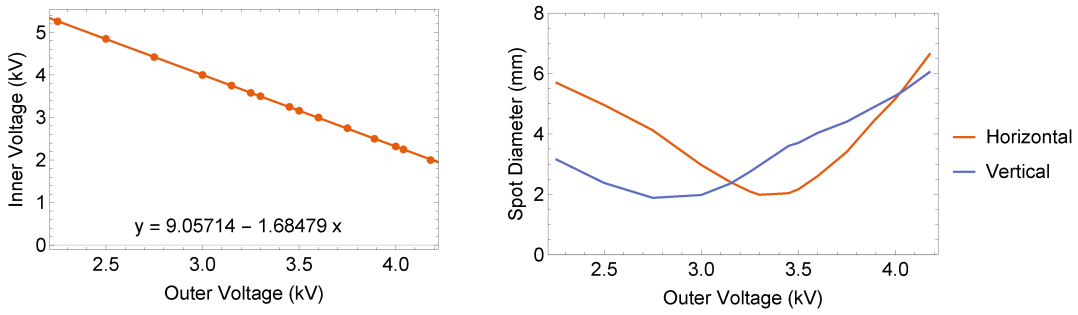

Figure 4.10: The inner and outer voltages needed to generate a 90° deflection (left), and the beam width in both horizontal (orange) and vertical (blue) directions for a 90° deflection at various outer electrode voltages (right).

particular, the spherical electrodes are very difficult to machine and, for the radius of curvature chosen here, require a costly custom chamber for housing. An alternative to this is the much simpler spherical deflector as presented in [33]. This device theoretically generates some asymmetrical lensing in the two transverse beam directions; however, this effect has been shown to be relatively small and well understood. Additionally, the simplicity of the structure allows it to be formed out of sheet-metal, making fabrication significantly easer. These thinner electrodes are able to fit within a standard 8 in. CF 4-cross, which further reduces the cost and footprint of the device.

For the TAMUTRAP beam line, such a deflector was designed in the spirit of [33], featuring a 240 mm radius of curvature for the transported ions and two 10 mm holes for line of sight and straight-through transmission as in the spherical device. This apparatus, along with the setup used to test it, is shown in Fig. 4.9.

Lead by Robert McAfee, this device was characterized with an offline ion source and found to exhibit minimal asymmetric lensing with an appropriate choice of inner and outer electrode potentials. As can be seen in Fig. 4.10, there exists a continuum of inner and outer electrode voltage configurations that generate the desired 90°

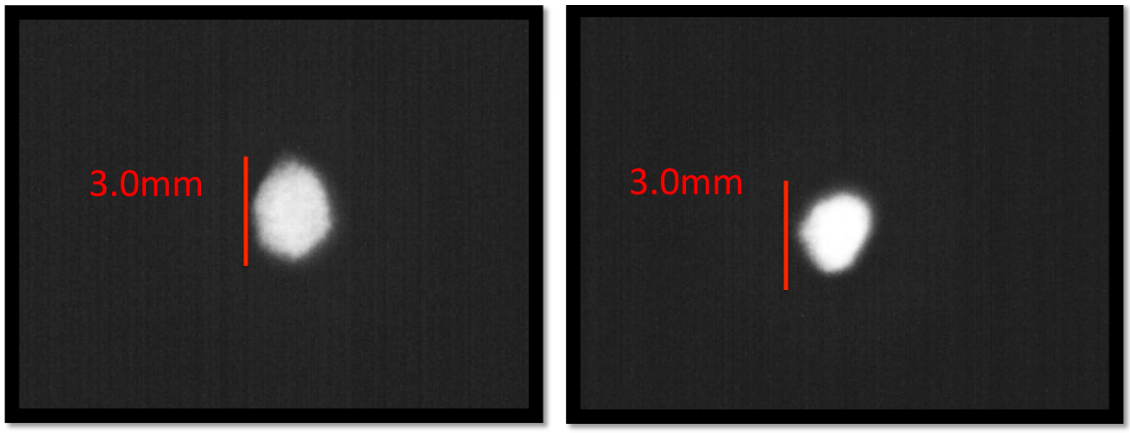

Figure 4.11: Beam spots as viewed on the phosphor of an MCP detector before (left) and after (right) a 90° deflection. Images are not at exactly the same scale.

deflection. However, only a single combination of inner and outer voltages fails to generate asymmetry in the resulting beam profile, indicated by the crossing point in the right pane of Fig. 4.10. The beam profiles with and without the bend are shown in Fig. 4.11. These tests were performed at 10 keV incident beam energy, with a highly collimated source. A different beam energy would require different values to produce a symmetric 90° deflection.

As a result of this work, the TAMUTRAP facility will employ cylindrical deflectors whenever possible in the future. The device has been shown to bend the available 10 keV test beam successfully at 90° with minimal transverse asymmetry at appropriate settings.

4.5 Diagnostic Station

In order to determine whether or not the ion beam is correctly being transported, bunched, or otherwise manipulated by the various elements of the TAMUTRAP beam line, some means of particle detection is necessary. For this reason, a modular diagnostic station (Fig. 4.12) has been created consisting of two primary detectors.

The first detector, an electron suppressed Faraday cup, is solely used to measure

beam current, with no position information. The detector consists of a floating copper cup, which is connected to the input of a pico-ammeter and is surrounded by a grounded sleeve. The copper collection electrode is 0.75 in. in diameter, and is positioned by a pneumatically controlled push/pull motion feedthrough. An additional annular electrode is positioned around the opening for the copper collection electrode. This is referred to as the electron suppression electrode, and can be floated to an arbitrary potential in order to force sputtered electrons back into the cup, improving measurement accuracy. The electron suppression ring potential was varied during testing to determine the optimum operating voltage. An asymptotic decrease in beam current was observed, flattening at around -50 V suppression voltage. It is understood that at this voltage nearly all electrons ejected by ion collisions (which would leave a positive "hole" in the Faraday cup, giving an artificially high signal current) are forced back onto the collection electrode. The Keithley pico-ammeter used to read out the incoming beam current for this device is capable of accurately measuring currents down to approximately 0.01 pA, or 6×10^4 singly charged particles per second. There is no practical[2] upper limit on incoming current for this detector.

The second port in the diagnostic station is occupied by a two-plate Micro Channel Plate (MCP) detector manufactured by Beam Imaging Solutions. This MCP detector, in either 18 or 40 mm diameters, consists of two glass plates replete with a multitude of tiny channels, oriented in what is known as a chevron configuration (*i.e.* the holes in the two plates are not parallel with one another), and backed by a metalized phosphor screen. The plates are impedance matched (to avoid electronic noise due to reflecting signals). Up to 1000 V per plate is applied across the detector,

[2]The ion source never exceeds 1 nA output, which well within the safe operating range of the pico-ammeter.

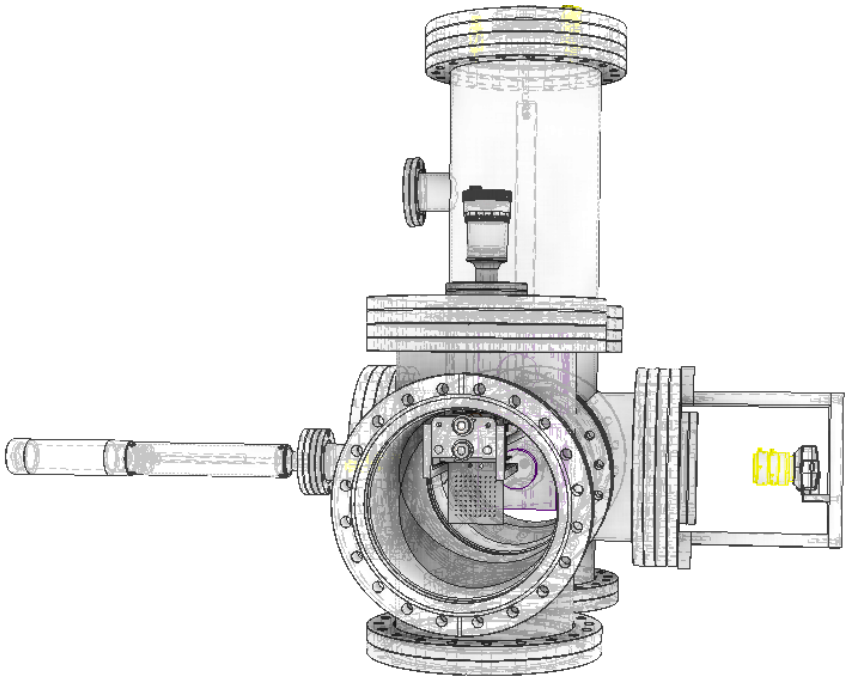

Figure 4.12: The TAMUTRAP diagnostic station centered on a Faraday cup and micro channel plate detector, here shown with the pepper pot emittance measurement attachment. The assembly is shown in wireframe to allow visibility of the inner configuration.

such that an ion striking the first plate will generate an electron shower, which is further amplified by the second plate. This secondary shower is collected on the metalized phosphor anode, which can be read out by electronics, or viewed by eye. Electronic readout is performed capacitively, and further signal processing is implemented as discussed in Ch. 5. The MCP detector is also situated on a pneumatic push-pull motion feedthrough. The maximum recommended operating current for such a detector is less than several nA; however, the sensitivity is quite high, allowing for the detection of single ions.

As mentioned, the MCP detectors are backed by a phosphor screen, in this case a 15 μm thick P43 phosphor that exhibits a 1 ms decay time. The screen is in turn backed by a 45° mirror, allowing the image to be viewed through a glass viewport oriented perpendicularly to the beam line. The screen, when viewed by a high resolution digital camera, gives position information for the detected particles, and can be calibrated to sub-mm precision.

Utilizing these two detectors, each diagnostic station is capable of measuring both high and low currents, as well as beam profiles in transverse space and time at the location of the device, which is equivalent to information about the beam in the three spatial dimensions. To observe the complete phase-space of the beam, however, additional information regarding the angular divergence of the beam (in the case of the transverse dimensions) and energy spread of the beam (in the case of the longitudinal dimension) is required. The transverse divergence can be measured by employing the pepper pot technique, as will be discussed immediately.

Emittance, which is a measure of the area occupied by a plot of the beam profile in phase-space, takes into account both momentum and position characteristics of the particles composing the ion beam at any time. In particular, in a single direction, the root mean squared (RMS) emittance, ε_{rms}, for a number of particles is defined

as,

$$\varepsilon_{rms} = \sqrt{\langle x^2 \rangle \langle x'^2 \rangle - \langle x x' \rangle^2}, \tag{4.1}$$

where $\langle x^2 \rangle$ is the variance of the single particle positions and $\langle x'^2 \rangle$ is the variance of the single particle angles.

The pepper pot technique [62] is a convenient method of measuring the transverse emittance of a particle beam in that it only takes one position sensitive measurement to make a calculation. The method involves the placement of a carefully perforated mask a known distance upstream of a position sensitive detector. The beam is collimated according to the perforation of the mask, and the clipped beam travels until its position can be recorded on the detector. When implemented correctly, the signal on the detector takes the form of numerous spots, corresponding 1:1 with the holes on the mask. The positions of the centers of the spots can then be related to the positions of the centers of the holes in the mask in order to determine the angle of incidence of each "beamlet." As a result, one can simultaneously capture angular information and position information for each hole, and, therefore, calculate the overall emittance in the two transverse directions. In the case of the pepper pot technique, single-particle position and angles are unknown, but this information is available per mask hole. As a result, the single-particle information in Eq. 4.1 is simply substituted by the hole information and weighted according to the intensity of the hole, giving a good approximation of the transverse emittance [57, 58]. Performing the measurement at several mask-detector distances may be employed to reduce error and infer systematics.

The emittance station add-on to the `TAMUTRAP` diagnostic station includes a 9 by 9 hole mask, with 1 mm hole diameter and 4 mm hole-hole spacing . The center hole is blocked to provide a reference for relating holes and spots in software. The mask is

located on a linear motion stage, operated by a manual rotational feedthrough. The mask was designed to travel one inch per 8 rotations of the the feedthrough. The minimum screen-mask distance is 22.2 mm, and the mask retracts in the manner of a garage door when it reaches its maximum displacement to allow the beam to travel straight through.

A complete data acquisition and analysis package, called the `TAMUTRAP` Emittance Measurement Program (TEMP), was written in LabView to perform the emittance measurements using the mask described above and a digital camera for viewing the phosphor screen of the MCP. The software will be used to capture data directly with an IDS uEYE high resolution digital camera, but analysis can also be performed off line with saved images. The workflow of the software and an example of an emittance calculation is shown in Fig. 4.13.

At the time of development, no position-sensitive detector was in place for an empirical test. To test the software, a simple ray tracing routine was written in Java. Inputs included particle mass, energy, position distribution, angular distribution, and the geometric particularities of the hypothetical system (mask properties and all relevant distances). The routine was used to perform a deterministic ray trace for a given number of particles, ultimately yielding position and angular information in addition to a boolean indicating whether or not the path intersected the mask for each particle. The emittance of the simulated beam generated in this program was calculated by directly computing ε_{rms} particle-by-particle according to Eq. 4.1 in Microsoft Excel, using the known position and direction of each particle. The ray trace output data was also used to generate post-mask beam spots as a grayscale JPEG image with a known pixel resolution in Mathematica. The resulting image was fed into TEMP along with the hypothetical parameters used to generate it, and the emittance generated by TEMP was compared to the value calculated particle-

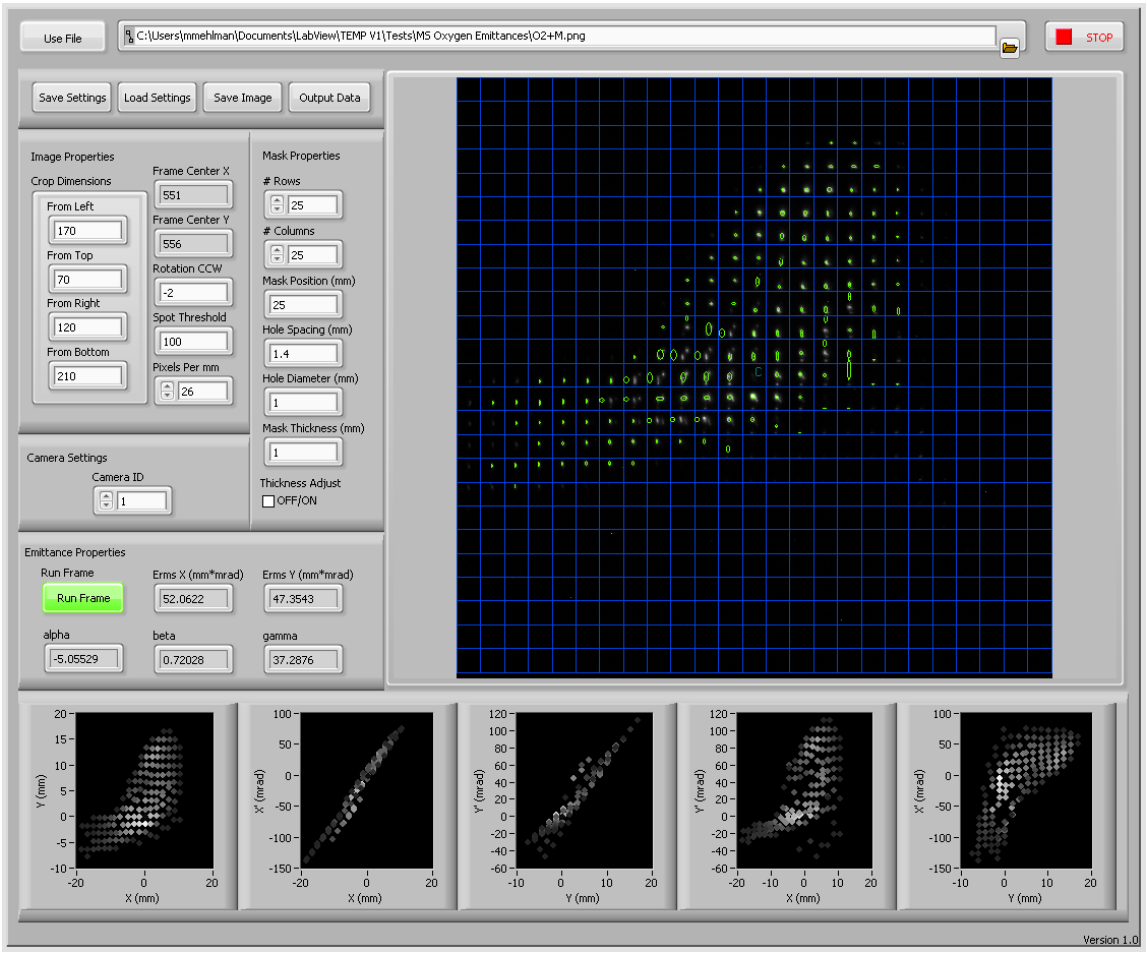

Figure 4.13: A sample emittance analysis in TEMP using data provided by Markus Strohmeier from Lawrence Berkley National Lab [59].

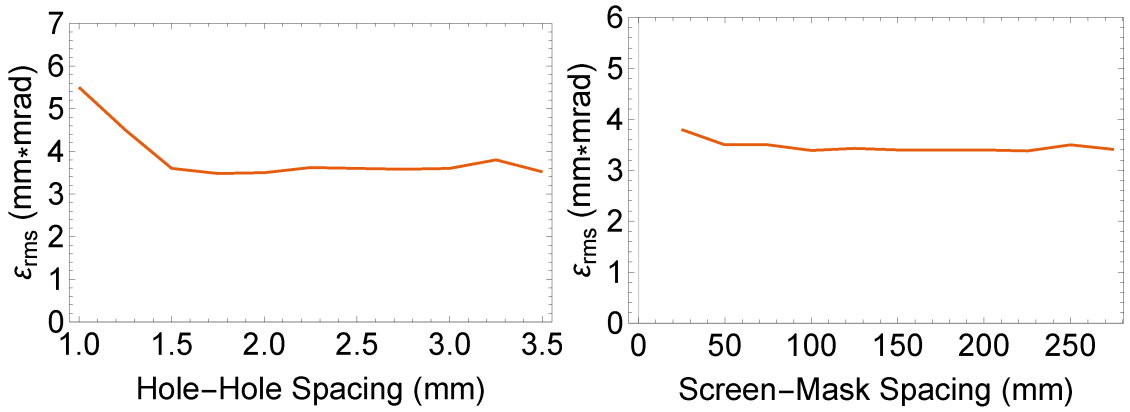

Figure 4.14: TEMP calculated emittance as a function of hole-hole spacing at constant (50 mm) screen-mask spacing (left), and screen-mask spacing at constant (2 mm) hole-hole spacing (right) using simulated data. Spot-mask spacing was held at 1000 mm and the generated events exhibited a theoretical emittance of 5.9 mm·mrad.

by-particle using Eq. 4.1.

The output of TEMP was studied as a function of several parameters, such as hole-hole spacing (a property of the mask) and screen-mask spacing (the position of the mask relative to the screen). These parameters should have no effect on emittance due to Liouville's theorem, which requires that phase space (or emittance) is maintained in the absence of non-conservative forces. Results for these systematic tests are shown in Fig. 4.14. As can be seen, the calculated emittance value is typically about 40% lower than the generated value, a large error. In the left pane, the abrupt change in measured emittance at low hole-hole spacing is due to overlap of spots, which made disentangling which spots came from which holes difficult, and should be disregarded.

A deeper literature search revealed that the pepper pot method can be very sensitive to small effects. Such easily overlooked factors as pixelation in the position sensitive detector are quoted as yielding as much as 15% deviation from the expected value [58]. A combination of small effects therefore, can easily yield a large discrep-

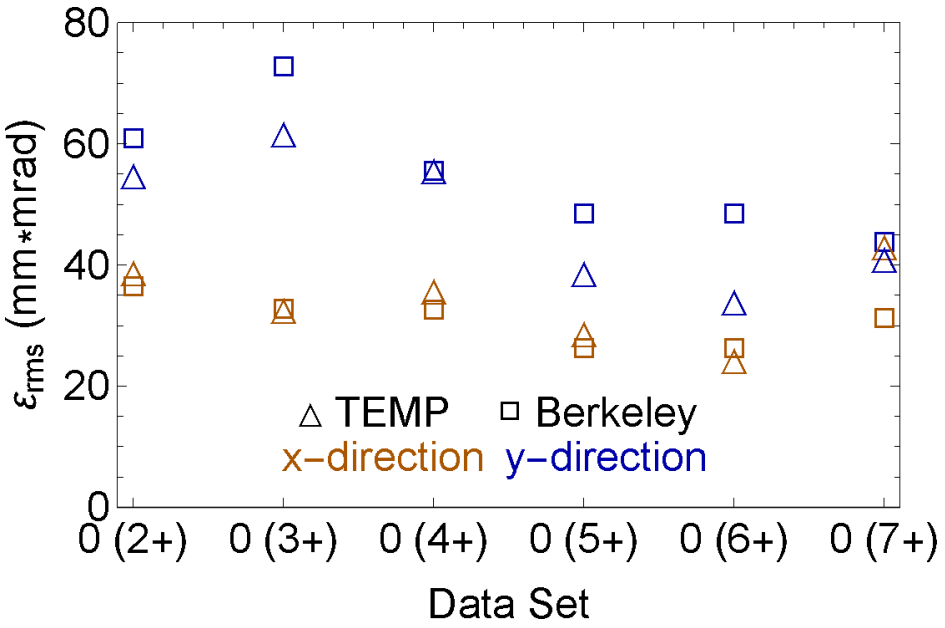

Figure 4.15: Comparison of emittance values for actual data provided by Markus Strohmeier from Lawrence Berkley National Lab [59] versus the claimed emittance.

ancy, and it is for this reason that it is typically recommended to employ the pepper pot technique as a qualitative measurement for determining relative emittances as a function of changes in the incoming beam.

To verify that the TEMP code was running correctly, data was provided for emittance calculations performed on an actual ion beam for comparison. This data, from the ion source at Lawrence Berkeley National Laboratory (LBNL), consisted of six Oxygen beams at various charge states. Photos of the beam spots after the pepper pot mask were provided, as well as all relevant measurement parameters [59]. Analyzing these photos in TEMP and comparing the resulting emittances to those measured at LBNL yielded the plot in Fig. 4.15. The emittances measured by TEMP are within a few percent of the values measured at LBNL, which is as good as should be expected from this method. As a result, it was determined that the TEMP software applies the pepper pot method correctly, but that the method should not

be used to perform any critical quantitative measurements.

Remaining work on this project will involve the commissioning of the emittance station in the TAMUTRAP beam line. The linear motion pepper pot mask stage will need to be installed, and initial transverse emittance measurements should be made with the offline ion source and position sensitive MCP detectors. In light of the above discussion, these measurements should be used not as absolute emittance values, but as reference values to determine the effect of subsequent changes to the beam elements being investigated (*e.g.* the effect of gas pressure in the RFQ on transverse emittance). Upon commissioning of the emittance stations, the TAMUTRAP diagnostic stations will exhibit the complete intended functionality, and may be used to their full design capacity in the beam line.

4.6 Ion Source

A hot filament offline ion source has been installed at TAMUTRAP for initial testing of the beam line and other devices in anticipation of coupling to T-REX. The source currently in use has been manufactured by Heat Wave Labs and is mounted in an ion gun electrode geometry designed by Yakup Boran as part of his masters project [10].

The source itself is composed of either Na or K deposited around a heating filament. These species were chosen for their ease of ionization and due to the fact that their masses are in the range of the isotopes that will ultimately be studied at TAMUTRAP. The filament heats the entire source to achieve thermionic emission of the alkali metals, typically with +1 charge due to their electronic structures. The ions are emitted roughly isotropically, and exhibit energy in the thermal regime. As a result, it is necessary to accelerate these ions in order to be a useful approximation of the final beam delivered by the T-REX upgrade. To achieve this, the entire ion gun [10] is situated at high voltage, typically 10 kV. Upon emission, ions are drawn

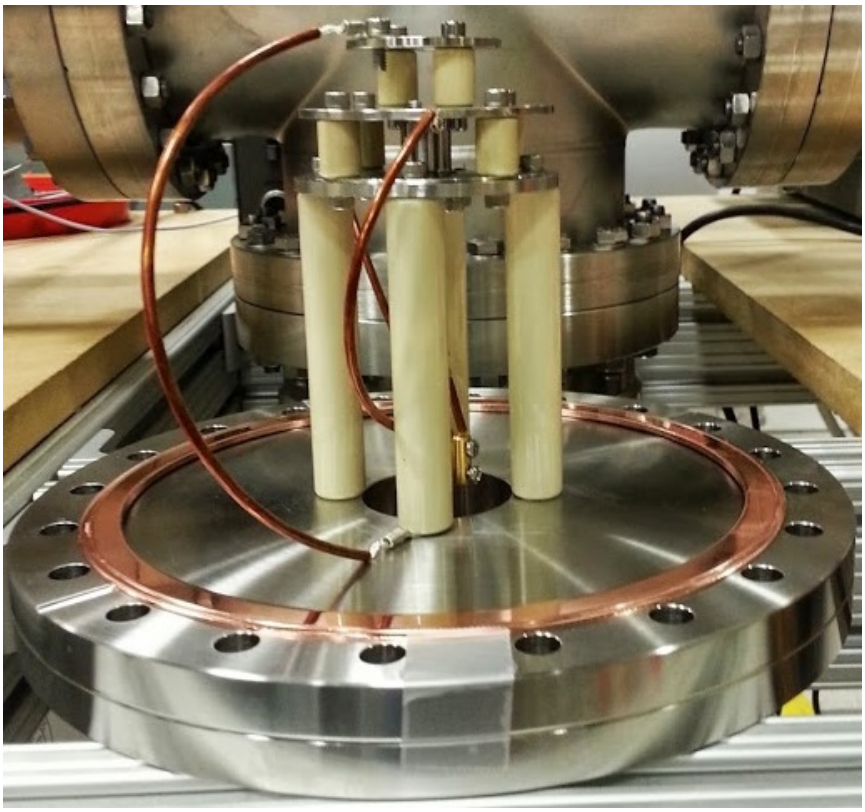

Figure 4.16: The ion gun electrode structure, which was designed by Yakup Boran [10].

through a series of collimators toward ground. One of the collimators features an adjustable voltage slightly different than the platform voltage, so that initial focusing may be achieved.

The power supply for the ion gun is based off of a Heat Wave Labs design with some modifications. The intensity of the beam output is a function of the temperature of the source, which is, in turn, a function, of the current applied to the heating element. The heating element current, which is set by the floating power supply, is generated by an adjustable autotransformer connected to the floating AC line within the power supply, which is used to effectively set the input voltage to the heating element as a fraction of the line voltage. Any line fluctuations are first transmitted to the floating platform via the 1:1 isolation transformer, and are then transmitted to the heating element via the autotransformer. Though these fluctuations are scaled along with the heating voltage, they are still passed on to the heating element, and can, in this way, create a time changing beam intensity. Additionally, the resistance of the source changes as a function of time (especially as the element heats up), so that even an ideally constant heating element voltage, will produce a time-changing heating element current, and, therefore, a time-changing beam intensity. It has been observed that after allowing the source to stabilize for several hours, the fluctuations of output beam intensity can be up to the 20% level at 0.5 pA (*i.e.* 0.1 pA). Fluctuations tend to be smaller, percentage-wise, at higher beam currents; however, as will be discussed in Ch. 5, testing at low beam currents is useful due to space charge limits in the RFQ Paul trap.

One method of improving the stability of the ion source in terms of output beam intensity would be to change the power supply to impose a current limit, rather than a proportional voltage limit, on the heating element. Though the device would still need time to ramp, once the operating temperature has been reached, a current

stabilized supply should remove the effects of any line fluctuations on the ultimate beam intensity. Such a supply is being investigated for future use at TAMUTRAP.

4.7 Control System

The control system currently in use at TAMUTRAP is a collection of LabView-based and other softwares used to edit settings of the various electronic elements employed. Custom LabView interfaces have been written for the MPOD power supplies, the gas control system, and the timing system (elements employed by the RFQ cooler/buncher will be discussed more in Ch. 5). Additional Windows executables are employed by the RF power generator and the ISEG high voltage crate power supplies.

LabView is an ideal solution for a control system, as it includes a diverse set of hardware drivers, making device communication easy. Additionally, software can be developed individually on an element-by-element basis and easily combined into a final coherent package when complete, allowing for improved ease of use and simpler recording of operating parameters. At this stage, the software still exists in many separate units.

There are two softwares used for power supply control. The ISEG MPOD modules are controlled with a custom LabView interface developed primarily by Robert Burch. This interface employs the simple net management protocol to communicate with the devices via TCP/IP over ethernet and fiber. The control system can handle any type of high or low voltage ISEG module that can be used in an MPOD crate. The high voltage ISEG crate used to control the injection optics is run with an IP protocol tool distributed by ISEG. Integration of this system into the custom interface is planned for the near future.

Settings for the gas control system for the RFQ (to be discussed in Ch. 5) are

adjusted via another LabView program that communicates via RS-232 to the MKS 146-C controller (via intermediate USB and fiber connections). This software sends PID settings, and reads the reported pressure at an adjustable rate. The T&C Power Conversions power amplifier is also communicated with via RS-232; however, in this case the software used to control the device has been distributed by the manufacturer.

Ultra precise timing for the TAMUTRAP experiment is provided by a National Instruments sbRIO-9623 Field Programmable Gate Array (FPGA), featuring a 40 MHz (or 25 ns) FPGA clock. This hardware has 96 digital IO channels which can be used as triggers or for determining or setting experimental states, in addition to several 12-bit analog inputs and outputs, which can ultimately be used to control proportionally adjustable power supplies or even record data. The advantage to using the National Instruments FPGA is that it can be programmed entirely in LabView. Trigger control software for the FPGA has been developed to send precise timing signals for ejection of the ion bunch from the RFQ, with an arbitrary number of additional channels available for future time-sensitive triggering tasks. This software is also planned to be part of the ultimate integrated TAMUTRAP control system.

4.8 Present State and Future Work

Many elements of the TAMUTRAP beam line have been tested and commissioned at this point (see Fig. 4.17 for a current view of the facility). An approximately 5 m section of beam line including the RFQ cooler/buncher, to be discussed in more detail in Ch. 5, is complete. Elements for additional sections of beam line have been fabricated and assembled and are awaiting installation.

To complete the TAMUTRAP beam line, several projects must still be accomplished. Three additional straight sections of beam line (one vertical and two horizontal) need to be installed and aligned, using mostly existing components. During this

Figure 4.17: The TAMUTRAP facility as of late 2014.

process, the existing straight section of beam line may need to be moved to match the alignment of the new sections, which are referenced to the still-undetermined final location of the T-REX project. One additional cylindrical deflector needs to be fabricated for the vertical 90° bend. The pulsing cavity must be installed and tested in conjunction with the RFQ ejection and the triggering system. Two more sets of turbo pumps need be purchased for general beam line vacuum needs: one to be used in the line following T-REX, and one to be employed before the ultimate location of the measurement traps. As discussed above, the pepper pot emittance station needs to be commissioned before application in the TAMUTRAP beam line.

Other than these required tasks, the TAMUTRAP beam line would also benefit from a few notable upgrades. Improvement of the power supply for the offline ion source is important for more accurate offline tests of any beam line element, especially the RFQ cooler/buncher, which will be discussed in greater detail in Ch. 5. The current

unit exhibits significant beam intensity instability, which makes precise, low current efficiency measurements very difficult. In addition to the ion source, the control system for the TAMUTRAP beam line should be unified in order to improve ease of use and allow for simplified recording of operating parameters. Finally, though suitable for commissioning, the pumping capacity and other vacuum features of the beam line (including the addition of safety features such as gate valves) should be improved in preparation for the addition of the Penning trap, in order to reduce contamination and background in future measurements.

5. THE RFQ COOLER/BUNCHER

The TAMUTRAP RFQ cooler/buncher will be employed to convert the continuous RIB supplied by the T-REX gas catcher to a bunched beam with low emittance suitable for efficient loading in the Penning trap system. The design chosen for the device is entirely new, though it has been inspired by existing facilities such as the cooler/bunchers at Argonne National Laboratory's Canadian Penning Trap experiment and TRIUMF's TITAN experiment. The advantages to the TAMUTRAP design are several: the electrode dimensions and spacing have been chosen to allow operation with a simple analog RF source, electrode-electrode clearances are smaller than in any other facility, allowing for a more continuous electric field (machining tolerances are correspondingly tight), the entire structure is symmetric across the axial mid-plane, allowing theoretical forward and reverse operation, and the design uses a minimum of custom parts, yielding a cost-effective and easily repairable apparatus. These advantages, as well as the general mechanical and electrical structure of the TAMUTRAP cooler/buncher, will be discussed in this chapter, and an initial characterization of the device will be presented.

5.1 Prototype

The TAMUTRAP cooler/buncher in use today is an evolution of a previous device, designed in 2010-2012. The initial device, pictured in Fig. 5.1, was inspired by an apparatus that had previously been used at Argonne National Laboratory.

The mechanical design of the device consists primarily of four parallel rods of radius r =7 mm and opposite-opposite spacing of $2r_0$ =12 mm. This gives a characteristic ratio of $r/r_0 = 1.1\bar{6}$, which is sufficiently close to the optimum value of $r/r_0 = 1.145111$ reported by [35] (see Ch. 3). The scaling of the electrode di-

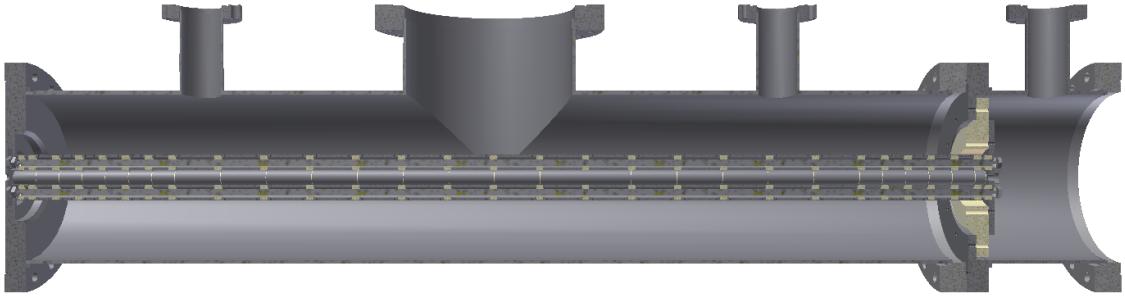

Figure 5.1: A rendering of the mechanical design of the prototype RFQ.

mensions was chosen to maximize room between electrodes, while at the same time allowing the structure to be electrically driven easily to high enough RF voltages through an analog circuit. As r_0 grows, the RF voltage must also grow, so while it is ideal for acceptance considerations to have a very large trap, the cost of electronics needed to drive such a trap increases quickly. The prototype TAMUTRAP RFQ was designed to operate at a q value of around 0.5, which is located safely within the stability region discussed in Ch. 3. This requires RF voltages on the order of 100 V peak to peak, and frequencies on the order of 1 MHz, depending on the mass of the ion of interest. These settings are easily achievable with an analog RF power generator, assuming the electrode structure exhibits reasonable electrical impedance.

In order to achieve cooling and bunching, the electrode structure was segmented axially into 28 segments. From the injection side, the segments were grouped in bunches of one at 9 mm length, five at 20 mm length, fifteen at 40 mm length, and seven at 20 mm length. These varying lengths were selected to allow finer control of DC potentials on injection and in the location where the bunch was to be formed. The entire electrode structure spanned approximately 86 cm.

The RF voltage for this device was generated with an analog radio frequency

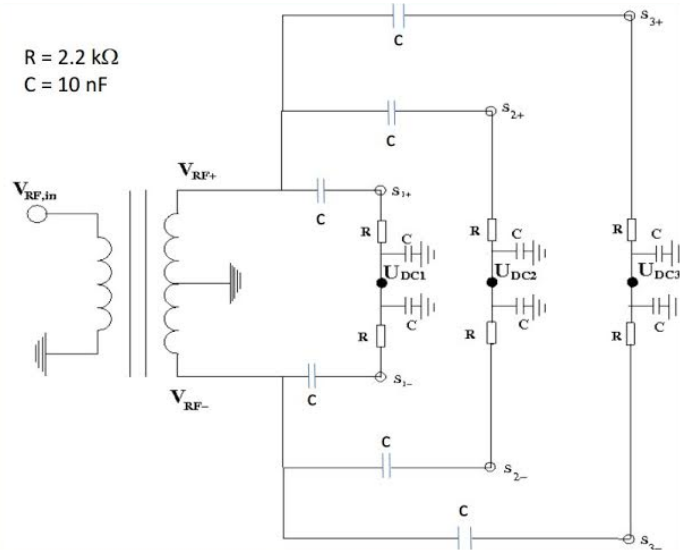

Figure 5.2: The RC circuit used to block RF from damaging the DC power supplies.

power generator, capable of driving the electrode structure above 100 V peak-to-peak. The linear, DC drag potential was applied to each segment individually via a Weiner MPOD multi channel power supply. The RF was coupled capacitively to the DC voltage for each segment via the circuit shown in Fig. 5.2, which has been designed by Praveen Shidling. This circuit was located entirely out of vacuum, and, as a result, yielded 56 outputs to be transported into the vacuum chamber and attached to the electrode structure (28 for each phase of RF).

During assembly and initial testing, a number of possible improvements were identified, precipitated by an observation of around 13% maximum continuous mode efficiency, which was well below the design goal of over 50%. The deficiencies in the original device will be discussed briefly, so that improvements become apparent in the discussion of the apparatus currently in use.

The primary shortcoming of the prototype device was the lack of mechanical rigidity and associated problems. As can be seen in Fig. 5.1, each rod is supported only on either end. The rods are assembled such that a threaded grounded support

runs through the center line of each rod, and is attached to a support piece at either end of the device. The rods were locked in place by two nuts outside of these support pieces. Sagging was prevented by tension in the threaded rod along the centerline. Individual segments were spaced (with 0.5 mm gaps) by captive ceramic spacers between every segment and between the first and last segments and the support pieces. These small ceramic spacers proved to be the weak link in the mechanical structure, and would not tolerate sufficient torque on the locking nuts to allow for sag free rods. If over-torqued, the ceramics would fracture, causing more significant problems. In combination with stacking of machining tolerances, these effects resulted in a sag over the length of the structure of several mm.

Though a sag itself is not a critical problem (there are many bending RFQs in existence, such as the multi-RFQ switch yard employed by the T-REX upgrade), an inconsistent sag between the four rods effectively alters the trapping parameters of the device as a function of length. Such an inconsistent sag was observed, the cause of which was determined to be stacking of machining tolerances and machining imperfections. Each piece in the assembly was given a tolerance of 0.005 in. on its length, but no overall tolerance on the assembly was stipulated. As a result, 28 segments employing 28 spacers could yield a maximum of $56 \times 0.005 = 0.28$ in. (or 7 mm) discrepancy between rod lengths, leading to inconsistent sag between rods. Since the RF voltage and frequency is ideally constant over the length, this yields a spatially varying q-parameter and, therefore, a spatially varying trapping efficiency. In practice, the rod-rod spacing, $2r_0$, was found to vary by as much as 2 mm (or around 10%) over the length of the device, and so greatly affected the trapping efficiency as a function of position, largely contributing to the poor observed efficiency.

The second most significant shortcoming of the prototype was improper align-

ment, leading to a loss of ions on injection. Contributions to poor alignment included inadequate physical supports outside the device, and a poorly designed support system for the injection side of the device. The injection flange of the prototype was fabricated with a recessed hole in which the injection-side support was intended to sit captively. Tolerances for the recessed hole and support were set at 0.0015 in., or ≈0.4 mm, since the support needed to be installed blindly while sliding the electrode structure into place from the opposite end of the apparatus. The large allowed tolerance created an inherent mis-alignment, which, in combination with poor external flange alignment, is thought to have caused a significant loss in efficiency. Additionally, the prototype design allowed only for a floating extraction support, with the injection plate permanently grounded. While this may or may not have had a direct effect on efficiency, having both injection and extraction electrodes adjustable allows for finer control of the incoming and outgoing ions.

In addition to the critical deficiencies mentioned above, many other potential improvements to the prototype were noted. The design called for many custom parts, that proved to be expensive individually in the case of replacement. Assembly was very difficult due to confined spaces and order of operations considerations. And, finally, the electronics would only physically fit outside the vacuum chamber, making wiring and installation a challenge, but also increasing line impedance due to RF being spread out to the 56 wires attached to each segment. These points and others were considered when designing the improved RFQ, as will be discussed in §5.2.

5.2 The TAMUTRAP Cooler/Buncher

The TAMUTRAP RFQ cooler/buncher (pictured in Fig. 5.3) is a new, flexible device designed to lower the emittance of the incoming radioactive ion beam, and collect and

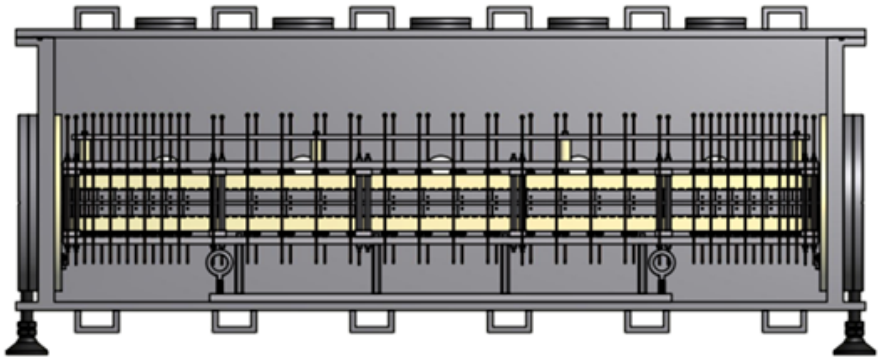

Figure 5.3: A rendering of the mechanical design of the TAMUTRAP RFQ cooler/buncher.

bunch that beam periodically into packets with energy spread on the order of 5 eV Full Width at Half Max (FWHM) and time spread on the order of 1.2 μs FWHM. Though inspired by the device located at the TITAN facility at TRIUMF [55], the TAMUTRAP cooler/buncher is an original, symmetric apparatus, that has been shown to achieve competitive performance with a minimum of custom parts paired with simple analog electronics. The design and initial characterization of this device will be discussed over the next sections.

5.2.1 Mechanical and Electrical Design

For the reasons listed in §5.1, the transverse arrangement of the electrode structure was unchanged during the design of the TAMUTRAP RFQ. That is, the device still utilizes a linear quadrupole field defined by rods of radius $r = 7$ mm and opposite-opposite rod spacing of $2r_0 = 12$ mm. This allows the new device to employ the same RF driver and electronics as the prototype.

The mechanical structure of the TAMUTRAP RFQ consists of 33 segments, totaling approximately 87 cm. The electrodes are arranged in groups of four segments at 9.5 mm, five segments at 19.4 mm, fifteen segments at 39.2 mm, five segments at

19.4 mm, and four segments at 9.5 mm, yielding an apparatus that is completely symmetric about the axial midplane. The support structure has been optimized to ensure mechanical rigidity and allow for tight machining tolerances. The backbone of the device consists of four baked alumina pieces to which all electrodes are directly fixed and that run the length of the structure. As a result, all electrode spacings are held at 0.38±0.13 mm, and are toleranced such that the total length of the electrode structure can vary by no more than ±0.13 mm as well. Transverse movement of electrodes (in both directions) is similarly limited to less than 0.13 mm, and angular mis-alignment is only tolerated by typically 0.2°.

In order to best hide dielectrics from the trapping region, minimal electrode-electrode gaps have been employed as discussed above, and the placement of the ceramic backbone is such that it occupies an insignificant solid angle as viewed by an ion on the centerline of the device. The only other ceramic pieces are standoffs for the RF bus (to be described shortly), which are hidden from view from the trap centerline, and the support structures that allow for floating the injection and extraction-side diaphragms, which are similarly hidden.

Additionally, the design has been performed with a conscious effort to minimize electrical impedance of the RF structures by minimizing material in critical locations. Any extraneous material that is in either capacitive or direct electrical contact with the RF driver poses a correspondingly larger source and sink for electrons, and, thus, reduces the attainable peak to peak voltage at a given power (a result of increased electrical impedance). To this end, the electrodes themselves have been moved as far away as possible from the grounded mechanical support, and the bus bars, which carry the two phases of RF into the vacuum chamber, are similarly stood off. The design that has been used has been influenced by several conversations regarding electrical impedance [46, 40].

Figure 5.4: A photo of the TAMUTRAP RFQ cooler/buncher during test assembly. The in-vacuum electronic circuitry is visible at top and bottom.

To reduce cost and fabrication time, as well as facilitate any future repairs, the main structure is composed of only 8 custom fabricated precision parts, with the remainder of the assembly coming from precision stock components. When separated from the base, the structure is also symmetric under 180° rotations in any direction, which facilitates installation and assembly. Apart from electronics, all components used are composed of aluminum, stainless steel, or ceramic for vacuum considerations. The electrode structure has been placed in a box-type chamber to allow for removal of the inner components without disassembly of the beam line.

The electrical design of the current TAMUTRAP RFQ has been carried over from the prototype device, with some critical modifications. RF power is generated by a T&C Power Conversions 175 W power amplifier with built in oscillator. The signal from this unit is separated into two out of phase components via a simple custom-wound one-to-one transformer with grounded center-tap. These out of phase signals are fed into the vacuum chamber via short coaxial RG-58 cables with BNC connectors.

Once inside the vacuum region, the signal is transported over short lengths of Kapton insulated single conductor wiring to one of two RF bus bars, respectively. From the bus bars, the voltage is transferred capacitively to each electrode individually via 500 V, 10 nF ceramic capacitors. Opposite electrodes are placed in electrical contact via bus wires, one for each electrode pair, or 66 in total. The peak-to-peak RF voltage seen on the RFQ electrodes as a function of the input power from the RF power amplifier can be seen in Fig. 5.5. A linear fit of this data averaged over the various frequencies gives,

$$V_{pp} = 35.41 + 1.03P, \tag{5.1}$$

where V_{pp} is the peak to peak voltage in Volts, and P is the input power in Watts as set on the RF power amplifier. The relationship between the input power and resulting peak-to-peak voltage is ideally linear while within the operating range of the transformer (in terms of frequency and power). It is possible to see some small deviations from the linear fit at the extremes in Fig. 5.5, which are, however, acceptable for our purposes.

The DC potentials of the first and last five segments of the TAMUTRAP RFQ cooler/buncher are supplied directly by individual ISEG MPOD low voltage power supply channels in order to allow for fine tuning of the potentials in these critical areas, while the majority of the structure is supplied voltage by a voltage divider designed to generate a linear potential drop considering the varying segment lengths. The voltage divider potential is set at each end by an additional single ISEG MPOD low voltage channels. Development of the voltage divider, as well as switching electronics to be discussed shortly, was performed by Louis Cooper, a summer Research Experience for Undergraduates (REU) student. Voltages are transferred into vacuum

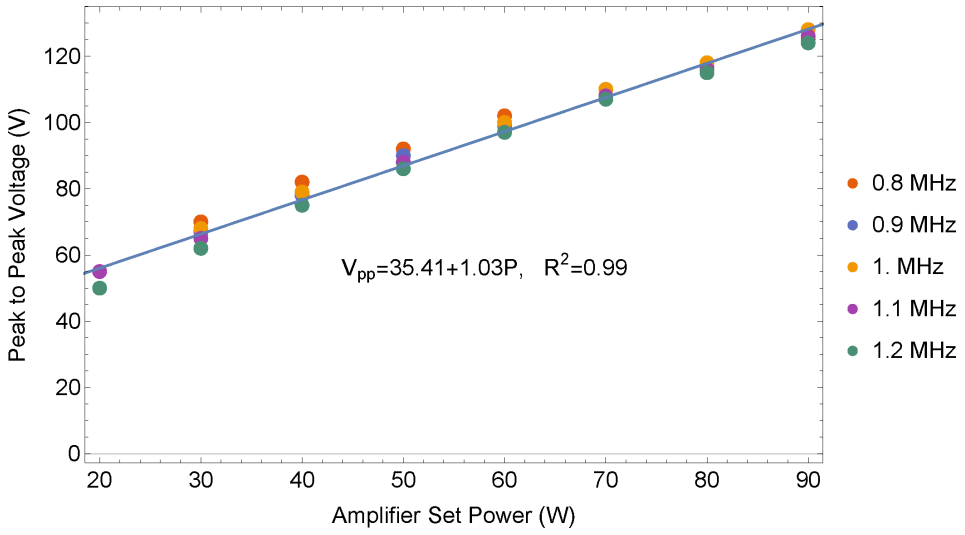

Figure 5.5: Peak-to-peak voltage as a function of power for the TAMUTRAP electrode structure, with a simple linear fit.

individually, where they are connected resistively through the same circuit shown in Fig. 5.2, though miniaturized and optimized for vacuum. The capacitors are small 10 nF ceramic capacitors used as AC filters connected to the grounded mechanical structure of the RFQ. Uncoated ceramic resistors complete the RC-circuit serving as current limiters for the DC power supplies. The resulting circuit reduces the ≈100 V RF voltage to the millivolt scale on the DC voltage supply lines, thereby protecting the power supplies. The entire assembly can be seen in Fig. 5.4, including the aforementioned RC protection circuit.

The configuration of the in-vacuum electronics is the same for all 33 segments; however, the last segment receives a different DC voltage supply in order to enable operation in switched mode, which is required for bunching and ejecting ions from the trap. For this set of four electrodes, two DC supply channels, one positive and one negative are supplied to a Behlke HTS series ultrafast high-voltage switch. The output of the Behlke switch is attached directly to the current limiting resistor in the protection circuit. The initial switching trigger is generated by the FPGA-based

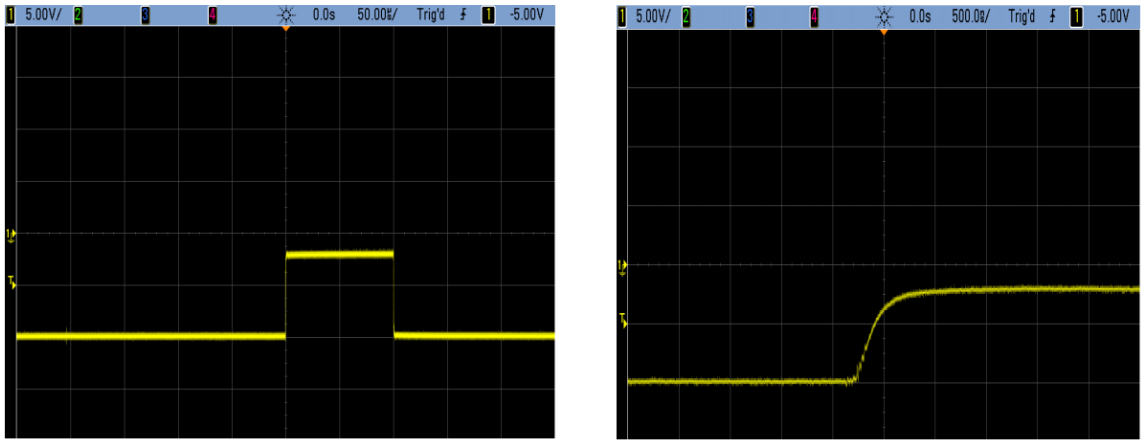

Figure 5.6: Sample output of the Behlke ultrafast high voltage switch before being installed. Courtesy of Louis Cooper.

control system as discussed in Ch. 4, which is first conditioned by a custom designed active amplification circuit in order to display the correct polarity and magnitude for acceptance by the Behlke switch. This work, also performed by Louis Cooper as part of the REU program, resulted in a fast-switching potential of rise time 500 ns with negligible jitter, as shown in Fig. 5.6 before being connected to the RFQ structure. After connection to the RFQ structure, the rise time was greatly increased due to impedance of the RFQ and the in vacuum RC filter circuit. The filter circuit is essentially a low-pass filter, and, as such, it impedes the fast voltage change of the Behlke switch, yielding a significant increase in rise and fall time. The switching voltage when connected to the electrodes is shown in Fig. 5.7 and displays a rise and fall time of approximately 50 μs, around two orders of magnitude slower than without the impedance load of the electrodes. Despite this, good bunching characteristics are still observed, as will be discussed. If an improvement of the bunch time is desired in the future, it can be achieved in two ways. Since the rise and fall time has been observed to be independent of the applied voltages, a greater voltage difference may be used to achieve a shorter time scale for the desired voltage range. Additionally,

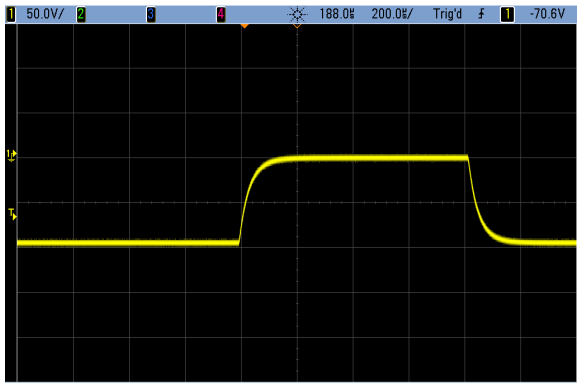

Figure 5.7: Output of the Behlke ultrafast high voltage switch after installation. The electrodes pose a significant impedance load, slowing the rise and fall time.

removal or modification of the low-pass supply protection circuit, which specifically limits high frequency spikes, can be considered, though care should be taken to maintain some protection for the Behlke swithc and power supplies from the RF trapping potential.

In order to achieve beam cooling, the RFQ must be operated in the presence of a buffer gas. For TAMUTRAP, ultra pure Helium (99.999%) has been chosen due to its low atomic weight, low reactivity, and the fact that it is relatively easy to obtain. In general, the cooling process occurs through the equilibration of the temperatures of the species that are present. Over time, a "hot" incoming beam and a buffer gas will attain thermal equilibrium. If the buffer-gas temperature is roughly room temperature, the thermal equilibrium of the system will be on the order of tens of meV. The additional energy transported into the system via the higher energy ion beam of interest is continually transferred to the buffer gas and pumped away by the vacuum system. A low atomic weight buffer gas is desirable due to the collision kinematics: when two particles of similar kinetic energy collide, the heavier of the two will, on average, achieve a lower velocity as a result of the collision (due to conservation of momentum). This increases the likelihood of retaining ions of

interest in the trapping region during cooling, thereby increasing efficiency.

At TAMUTRAP, the buffer gas is maintained by an MKS 146C controller operating a Proportional-Integral-Derivative, or PID, loop between a capacitance manometer vacuum gauge and an electronically-controlled precision needle valve. The capacitance manometer can read pressures in the range of $10^{-1} - 10^{-4}$ mbar, and provides feedback through the PID loop to the control valve. After selecting a set-point, the position of the valve is continuously adjusted to maintain the desired pressure. The system is not closed, having 6 mm diaphragms on either side of the RFQ chamber. As a result, a pressure gradient is established from the injection point of the gas (in the center of the RFQ) to the pumping ports. This gradient is not linear, and is affected by geometry: for example, relative to the gradient outside the RFQ diaphragms, the pressure is roughly constant within RFQ chamber. The range of pressure available for use is dependent on the maximum supply rate of gas from the control valve and the pumping speed of the beam line pumps to ensure that satisfactory beam line pressures are maintained. For the purpose of this experiment, we have taken the maximum operating pressures of the MCP detector and hot cathode ion source (10^{-6} mbar range) as the upper limit for the allowable beam line pressure. With the nearby turbo pumps (first discussed in Ch. 4 and to be mentioned again in §5.2.2) operating at full pumping speed, a maximum buffer gas pressure as measured by the capacitance manometer within the RFQ of 5×10^{-3} mbar is attainable.

5.2.2 Installation and Alignment

Commissioning and initial characterization of the TAMUTRAP RFQ cooler/buncher and adjacent beam line has been performed offline using a hot cathode ion source (described in Ch. 4). Though some changes will be required when coupling to the T-REX line, considerations have been made to ensure that the test setup is as accurate

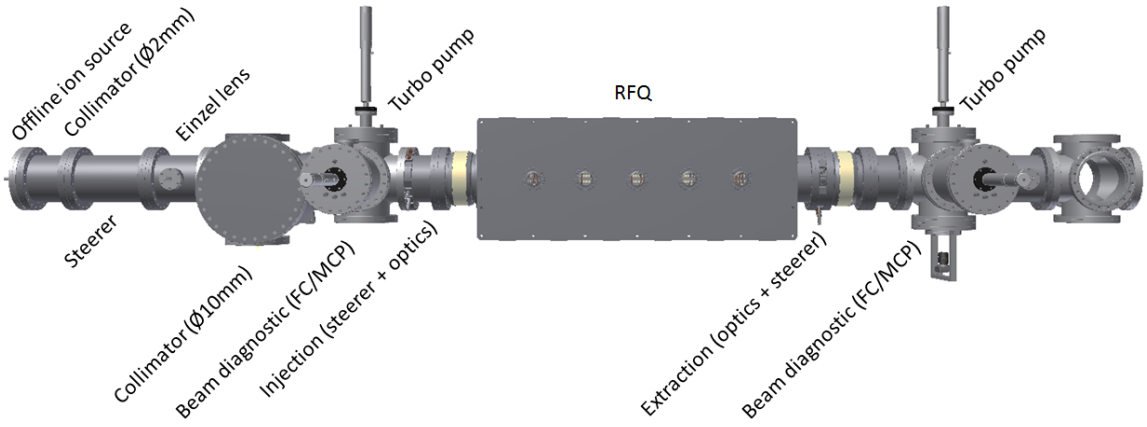

Figure 5.8: A schematic of the test beam line used for initial characterization of the RFQ cooler/buncher. For scale, the RFQ chamber is approximately 97 cm in length.

a representation of the final beam line as possible.

The beam line used for the initial characterization of the TAMUTRAP RFQ cooler/buncher can be seen in Fig. 5.8. The most important elements in this set up are, in order: the Heat Wave Labs ion source, 2 mm collimator, Einzel lens, 2-axis beam steerer, 10 mm collimator, diagnostic station, 2-axis beam steerer, injection optics, 6 mm entrance diaphragm, RFQ electrode structure, 6 mm exit diaphragm, extraction optics, 2-axis beam steerer, and diagnostic station, respectively. These elements are all contained within the 8 in. CF vacuum system introduced in Ch. 4, and turbo pumps with pumping speeds of 1000 L/s and backed by dry scroll roughing pumps are placed at the locations of the diagnostic stations. The beam line is in its approximate final location, but will require re-alignment during coupling to the output of the T-REX multi RFQ switch yard.

Alignment of the TAMUTRAP RFQ cooler/buncher test line was performed via optical transit. The optical axis itself is arbitrary since there is no fixed relation to the T-REX beam line at this time; however, the axis has been recorded by two targets on the high bay floor (one on a shielding block and one on a fixed cement wall), and

one midplane mark on a nearby steel I-beam. The optical transit that was used to generate the axis to which all elements were aligned can be replaced by re-aligning to these targets.

Once the optical axis had been established, centers of the flanges that are used to support the beam line were forced into alignment via 1/2-13 set screws located on the beam supports. The center of the flange was located by threading a thin (diameter approximately 0.2 mm) red thread that was wound between pins located in bolt holes of the flange separated by 90°. The location at which the threads crossed was considered the flange center to within about the diameter of the thread. Several elements were further aligned within the centered flanges via set screws on individual electrodes. In general, the process was performed on elements in sequence, beginning with the ion source flange. Results at the seven locations of beam alignment can be seen in Fig. 5.9.

The flange on which the ion source was mounted was the first location to be aligned. This flange was aligned to near perfect center (a deviation of no more than 0.1 mm in any direction) with the optical axis; however some small deflection is expected to have occurred after placement of the ion source, which has non-negligible weight. It is estimated that the final mis-alignment on this section is less than 1 mm in the vertical direction. A 2 mm diameter hole has been placed in the exact center of a copper gasket for use as a collimator between two adjacent CF flanges at approximately 28 cm from the ion source flange, and was the next element to be aligned to the optical axis. This centered collimator was aligned to approximately 0.5 mm in both the vertical and horizontal directions. A second, larger, 10 mm collimator, located at approximately 73 cm from the ion source flange was aligned to about 2 mm in both horizontal and vertical directions. By this location, the beam axis will already have been well-defined, so that as long as the beam is transmitted

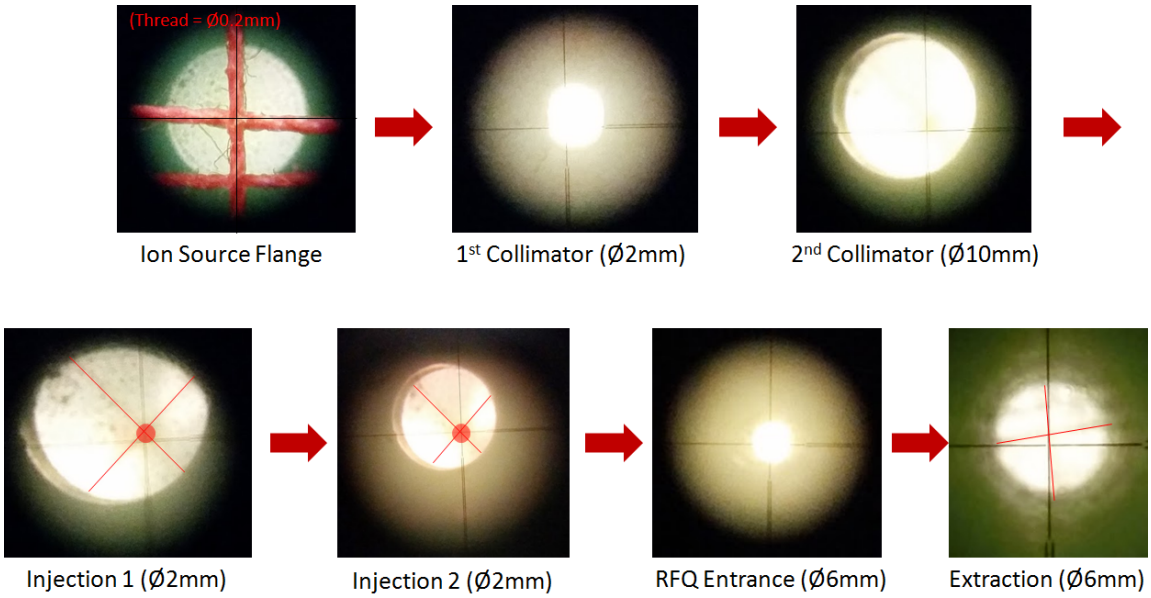

Figure 5.9: The final achieved alignment can be seen at several locations along the beam line, as viewed through the optical transit. Thread indicating the flange center is highlighted with red lines, and opaque red dots highlight collimator centers, where applicable.

by this collimator, no negative consequences will result from minor mis-alignment.

The floating electrodes for the injection optics allow additional centering via the set-screws supporting each electrode. As can be seen in Fig. 5.9, the first floating injection electrode was aligned to less than 1 mm from the optical axis vertically, with negligible mis-alignment in the horizontal direction. This was achieved by placing a tight-fitting collimator with centered 2 mm hole within the injection electrode, and aligning to this hole through fine adjustments of the set-screws holding the element in place from the support structure, and subsequently removing the collimator. The same procedure was followed for the second injection electrode, for which a slightly better alignment of less than about 0.5 mm in either direction was achieved. The red lines in Fig. 5.9 indicate the alignment of the flange on which the injection optics were mounted. This flange is also centered to within 0.5 mm in any direction.

Finally, the 6 mm injection and extraction diaphragms of the RFQ were aligned. These diaphragms are theoretically centered within the RFQ vacuum chamber's flanges, so alignment was performed by manipulating the flange centers to the optical axis. A deviation of less than 0.5 mm in either direction was achieved at both locations. After the alignment procedure was completed, the vacuum chamber was sealed on each end, and pumped down. Overall, critical elements were aligned to within 1 mm in any direction by this process, with the majority of elements centered to the arbitrary optical axis to within 0.5 mm, which should be sufficient for TAMUTRAP.

5.3 Initial Characterization

The TAMUTRAP RFQ cooler/buncher and adjacent beam line has been initially characterized with the offline ion source in two modes. First, the continuous mode efficiency was examined for several energies. Though this mode is not planned for use in TAMUTRAP experiments, it is a convenient metric to compare to existing facilities [55] and hints at the efficiency of the device. The second mode in which characterization has been undertaken for the TAMUTRAP RFQ is bunched mode. This is the mode in which the device will ultimately be operated. Properties of the bunch, such as time spread and bunch size (integrated number of ions), have been systematically investigated for this mode as a function of the device's operating parameters. As can be seen in Fig. 5.8, the diagnostics are located before the injection optics and after the extraction optics, respectively. The results presented here are, therefore, an examination of the performance of the injection optics, RFQ, and extraction optics as one unit (which will simply be referred to as the RFQ from this point).

One of the greatest sources of error present during characterization was due to fluctuation of the ion source current output. As discussed in Ch. 4, the ion gun power

supply utilizes a simple auto-transformer to scale the voltage of line AC to the desired heat setting for the source, and, as a result, the intensity of the source has proven very unstable. The output intensity has been recorded to fluctuate to greater than 10% of its value at some settings. An additional significant uncertainty is due to the precision on Faraday cup readings since the pico-ammeter is often being operated at the lower limit of its sensitivity. And, finally, the statistics also contribute to uncertainties in the presented results.

When present, error bars in the following discussion have been obtained by calculating the simple standard deviation of values derived from numerous ($\gtrsim$60) individual bunches. The center value is calculated as the simple average. Reported uncertainties should be considered a lower limit, since systematic effects have not been included. When omitted, uncertainties for measurements should be considered significant, and the results should be interpreted qualitatively.

5.3.1 Continuous Mode

Continuous mode efficiency for the RFQ cooler/buncher is defined as the ratio of the beam current observed at a Faraday cup detector located after the extraction optics (FC2) to one located before the injection optics (FC1), *i.e.* Efficiency= FC_2/FC_1. The Faraday cups in question are both of the same design, and are electron-suppressed. Each Faraday cup is read out by a Kiethley pico-ammeter. For these tests, beam current incident on FC_1 was typically $\approx$2 pA (corresponding to the order of 10^7 pps). Such a current is safe for use in the RFQ, which should be able to handle approximately 10^8 pps in continuous mode, and is above the minimum stable output intensity of the ion source (about 0.5 pA). Beam energy was adjusted by varying the potential of the high voltage platform on which the RFQ cooler/buncher sits, while maintaining the source platform at about 10 kV, (yielding a beam energy

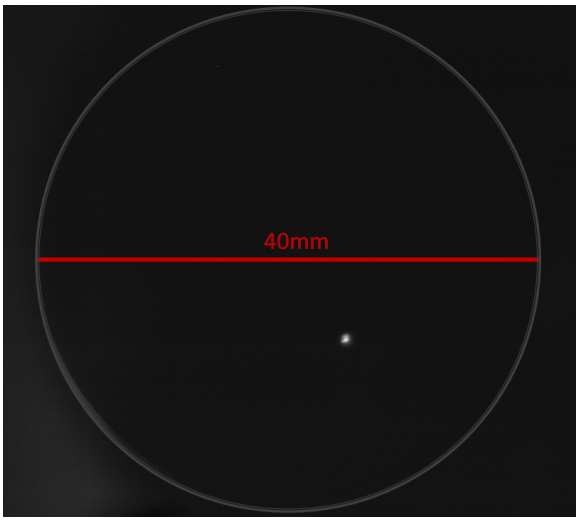

Figure 5.10: The collimated beam spot as seen on the first diagnostic MCP (located immediately before the injection optics). The spot is not concentric with the detector due to a misalignment in the detector mount, but can be injected into the RFQ with high efficiency.

of 10 keV with respect to ground).

Before performing efficiency measurements, the position sensitive MCP detector was used to ensure that the beam size could be contained entirely within FC1. If the beam spot were to exceed the diameter of FC1 (and could subsequently be lensed into the RFQ), it would be possible to achieve an artificially high efficiency. For all tests mentioned below, the beam spot at FC1 was located entirely within the acceptance area of the 19 mm diameter Faraday cup detector (Fig. 5.10). Similarly, the efficiency of the RFQ itself will be measured to be artificially low if transmitted beam misses FC2. Focusing onto FC2 was achieved by manipulation of the extraction optics. Ultimately, however, it is the overall efficiency of the combined device that is important.

For high incident beam energies (100 eV and above), it was observed that setting a non-zero drag potential over the length of the RFQ generated a higher transmission efficiency than having no drag potential (0 V/cm). Since the axial DC potential

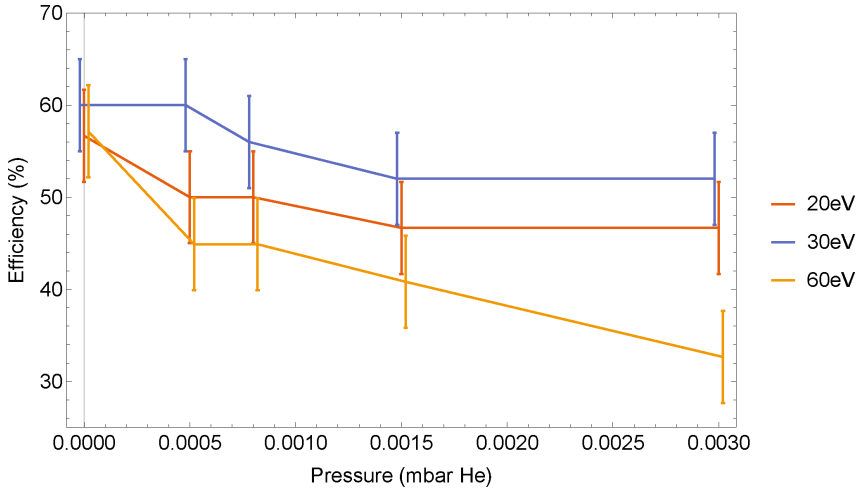

Figure 5.11: Continuous mode efficiencies as a function of pressure for 20, 30, and 60 eV beam energies, with all DC RFQ voltages set to 0. Error bars are assuming an uncertainty in 0.1 pA on current measurements.

returns to 0 V at either end of the device, this non-zero drag potential is thought to provide additional lensing. Tweaking the drag potential has yielded maximum overall continuous mode efficiencies of 74% at 180 eV and 65% at 100 eV beam energies.

Since trapping efficiency for a Paul trap improves (to an extent) as incoming ion energy is lowered, a more important regime for measuring efficiency is the range from 0-60 eV beam energy. In this range, it was observed that any significant deviation from 0 V/cm drag potential would actually lower the observed efficiency. As a result, efficiency was tested as a function of pressure at three energies (20 eV, 30 eV, and 60 eV), with 0 V/cm drag potential and all other RFQ electrodes set to 0 V. It is likely that some improvement could be achieved by fine adjustment of the RFQ DC potentials for individual energies and gas pressures, so the efficiencies reported in Fig. 5.11 should be considered lower limits. During testing, fluctuations in the ion source and pico-ammeter readings were observed at the 0.1 pA level, corresponding to a 5% uncertainty on the ≈2 pA incident current, as indicated in the error bars of

Figure 5.12: Block diagram for acquisition as used in RFQ bunched-mode characterization.

Fig. 5.11. The efficiency, peaking at the 60% range for a 30 eV beam, is competitive with continuous mode efficiencies reported at other facilities [55]. Logically, the efficiency decreases with increased gas pressure due to scattering losses. For the beam energies tested, the optimum continuous mode beam energy appears to occur at 30 eV. For too low an incoming energy the constant transverse component of ion velocity begins to dominate (*i.e.* transverse emittance dominates), making injection difficult, while at higher energies capture of the ions in the Paul trap is made more difficult and initial collisions with the gas are more violent, ejecting ions from the trap at a higher rate.

5.3.2 Bunched Mode

In normal use, the `TAMUTRAP` RFQ cooler/buncher will be operated in bunched mode, collecting ions of interest for some set amount of time, bunching them, and ejecting them in a tight packet. The design goals for this mode of operation had initially been set at 5 eV FWHM energy spread and 1.2 μs FWHM time spread for the emitted bunch. In what follows, yield and time spread will be examined; however, it has not been feasible so far to study the energy spread of bunches emitted by the device due to measurement constraints.

One quantity needed to characterize the bunches formed by the RFQ is the time spectrum of individual ions after bunching relative to some reference time, in this case the signal sent by the FPGA to begin the ejection process. Individual ions are

detected by a 40 mm Beam Imaging Solutions MCP detector. The electronics block diagram for preliminary signal conditioning is given in Fig. 5.12. The signal from the MCP is first amplified using an Ortec VT120 fast pre-amplifier. This output is further amplified with an Ortec FTA 820 fast timing amplifier, and a threshold is applied with a Tenelec TC454 Constant Fraction Discriminator, or CFD. The threshold was set as low as possible such that when the beam was blocked (corresponding to background) the CFD only fired at few Hz, corresponding to essentially 0 background over the μs timescale of interest. The CFD output was displayed and recorded by an Agilent InfiniiVision DSO7104A digital storage oscilloscope. The time resolution employed for data recording was chosen to be 10 ns per bin to safely record the approximately 20 ns width CFD output pulses.

Resulting data files were transported to a computer for offline analysis in Wolfram Mathematica 10 [64]. Workflow for reconstructing an ion bunch in Mathematica consists of several steps. First, the scope voltages were imported from the data files. The Mathematica function `PeakDetect[]` was run on the data for an individual bunch in threshold mode, with the threshold set to approximately one half the output voltage of the CFD (in this mode, `PeakDetect[]` identifies any element exceeding the threshold as a peak). The output of this function is a new table noting the location of peaks by "1" and the lack of a peak by "0," which was subsequently multiplied directly by the timing column of the scope output, creating a list consisting of zeros where there was no MCP signal, and the time of the hit when an MCP signal was recorded. Zeros were deleted from the list, the result was histogrammed (here in 0.25 μs bins), and the time spectrum could subsequently be fit or undergo further analysis as needed.

To extract the FWHM characterizing the time-spread of the bunch and the normalization parameter indicating the number of ions appearing in the bunch, the time-

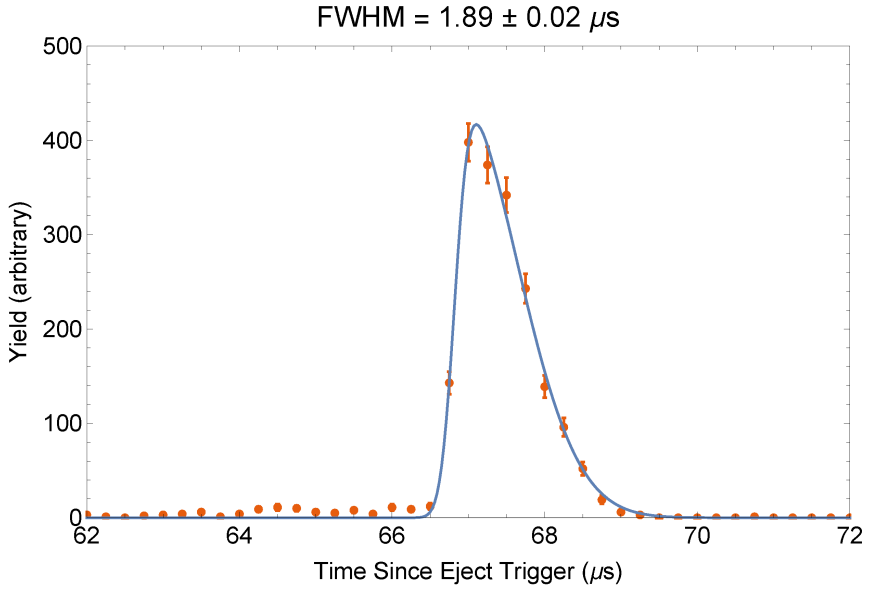

Figure 5.13: A good bunch with skewed Gaussian fit superimposed. Beam energy = 30 eV, gas pressure = 3×10^{-3} mbar He, drag potential = 0.08 V/cm, incident beam current = 0.7 pA. FWHM of Gaussian fit = 1.89 μs. Note that the mean bunch time of $\approx$ 67 μs is consistent with a several μs time of flight (as predicted by SIMION) combined with the 50-60 μs fall time of the bunching potential wall, as in Fig. 5.7.

spectrum histogram was fit by a skewed Gaussian, as in Fig. 5.13. RFQ-generated bunches are typically fit in the literature by a normal (not skewed) Gaussian function. Employing the skewed Gaussian allows for a much better fit to the long-time tail of the ion time-distribution. However, the resulting FWHM is nearly a factor of 2 larger than when fitting with a standard Gaussian (which neglects this low-count tail). As a result, while we are more satisfied with the fits achieved in this work, the enlarged bunch widths resulting from this fitting method should be kept in mind when comparing results to other facilities. Regarding the yield, it is important to note that the fluctuation in ion source intensity was significant during the RFQ characterization, so the reported yield should only be considered as a useful metric for comparison over the course of a single systematic study of short duration. Even then, caution should be observed when comparing number of counts between data points, as fluctuation of up to 10% in ion source current was observed on a several minute time scale.

The procedure for creating and ejecting a bunch follows several steps. First the settings of elements upstream of the RFQ were adjusted to values that had been observed to optimize efficiency in continuous mode, while checking that the entire beam spot was still visible on the first MCP detector. Next, all RFQ parameters were set to the values that had so far exhibited the best bunch (these values were initially determined by SIMION, calculations, and extensive trial and error). Faraday cup current downstream of the RFQ was optimized in continuous mode by making small steerer tweaks at each steerer location to align the beam. The RFQ was then switched to bunched mode by enabling the periodic operation of the Behlke high voltage switch and necessary power supplies, at which point only the MCP remained useful for diagnostics. The ions were blocked from traveling through the RFQ by means of a high ejection wall (275 V), and, as a result, cooled for a set amount of

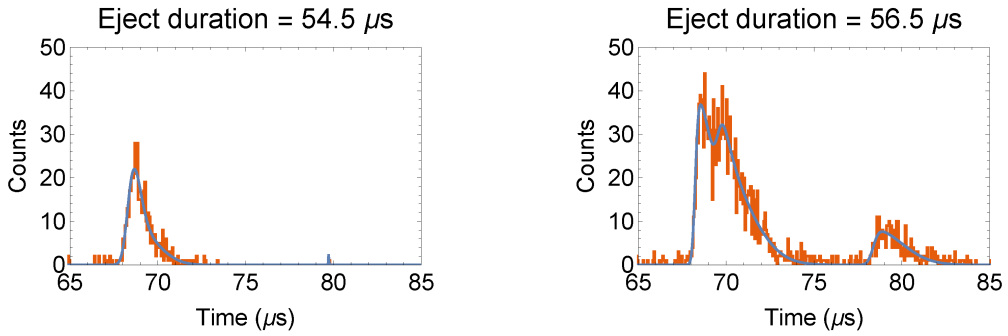

Figure 5.14: Bunches for which the eject duration was appropriate for the species of interest (left) and too long (right). Beam energy = 30 eV, gas pressure = 3×10^{-3} mbar He, drag potential = 0.08 V/cm.

time in the presence of the buffer gas (all studies detailed below employed a 250 ms cooling time, unless noted). A cooling time systematic study showed no significant change in bunch characteristics down to 15 ms cooling time, suggesting that bunches are fully cooled for the durations tested. Current draw on the power supplies for the last segment became too great to employ cooling times less than 15 ms, so this parameter could not be further probed, and partially cooled beams have not been investigated. Once the cooling time for a particular bunch had elapsed, a trigger was sent to the Behlke ultrafast switch to flip the final ejection segment of the RFQ to a negative polarity supply to allow ions to escape. The potential wall was switched back to the positive polarity supply after the eject duration had elapsed in order to begin collecting and cooling the next bunch.

Several operating parameters of the RFQ were investigated systematically by starting with device settings that had been known to generate a good bunch and testing the effect of adjusting one parameter at a time. Though various parameters are bound to be coupled to some degree, there are simply too many degrees of freedom to test coincidently. Operating parameters generating the best observed bunches can be found in Appendix A.1.

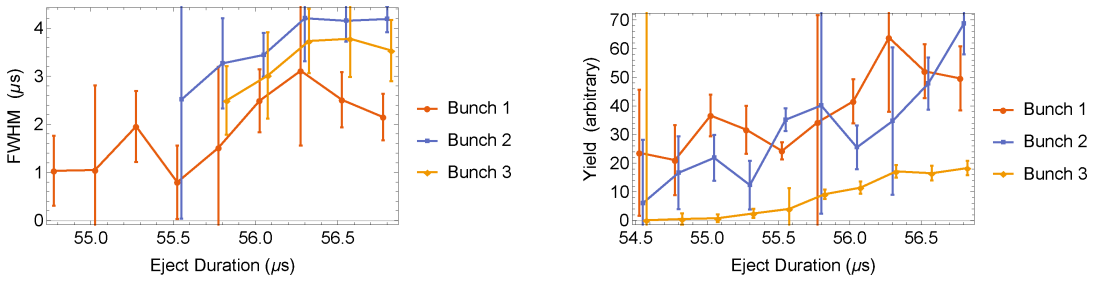

Figure 5.15: Bunch FWHM (left) and yield (right) as a function of eject duration for the three primary identified bunches. Beam energy = 30 eV, gas pressure = 3×10^{-3} mbar He, drag potential = 0.08 V/cm.

The first parameter studied systematically was eject duration, defined as the difference in time between the triggers sent to lower and subsequently raise the voltage on the last RFQ segment. When the segment is set low (-110 V relative to the high voltage platform), the bunch is allowed to escape; when it is set high (275 V relative to the platform), the bunch is trapped. The optimum eject time depends on many parameters, such as gas pressure and DC drag potential; however, all settings apart from eject duration were held at constant values for this test.

Fig. 5.14 shows typical time spectra for bunches with two different eject durations. The plot on the left indicates that a good bunch can be achieved with an eject duration of 54.5 μs for the following settings: beam energy = 30 eV, gas pressure = 3×10^{-3} mbar He, drag potential = 0.08 V/cm. The right plot, however, indicates the existence of additional bunches that become apparent when the eject duration is allowed to exceed the optimal value. Up to three primary bunches (here fit with three individual skewed Gaussians as in Fig. 5.14) could be identified with a sufficiently long eject duration. It is believed that these three bunches correspond to three different masses of charged particle trapped in the RFQ cooler/buncher, as opposed to multiple bunches of the same species or electronic noise since increasing yield for each bunch is observed independently (and at different rates) as eject du-

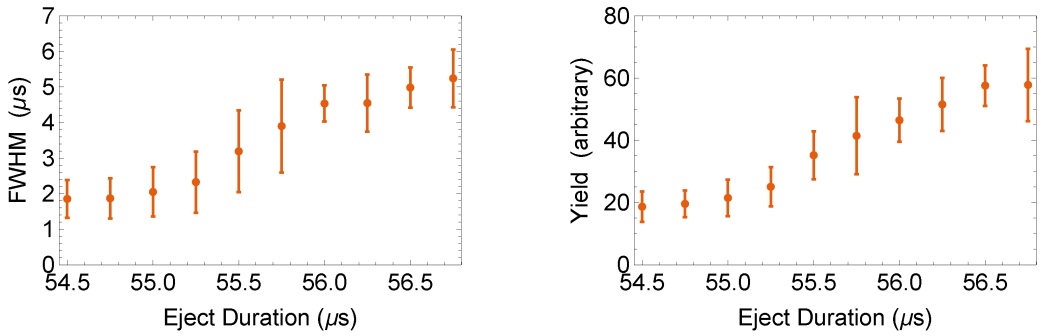

Figure 5.16: Original analysis of bunch FWHM (left) and yield (right) as a function of eject duration for the first two bunches together, before they had been resolved individually (the final bunch was previously identified and was excluded in the fitting). Beam energy = 30 eV, gas pressure = 3×10^{-3} mbar He, drag potential = 0.08 V/cm.

ration is increased (Fig. 5.15, right). This is consistent with more massive trapped species exiting the trap more slowly upon ejection, since such particles would necessarily exhibit a lower average velocity at the same kinetic energy. All bunches are also believed to be related to the ion species of interest, since it has been observed that blocking the ion source completely quenches all three peaks. As a result, it is believed that the first peak corresponds to the singly charged ion of interest, which represents the lightest possible charged particle composed of the incident ions.

The two initial bunches are separated by on average 1.24 μs in time of flight and therefore exhibit significant overlap, which made fitting difficult (evidenced by the significant error bars in Fig. 5.15). The magnitude of the bunches is similar at long eject durations; however, at short eject durations the shortest-time bunch dominates. Before the identification of the three unique bunches, initial fits employing a single skewed Gaussian to cover the first two peaks demonstrated an increase in FWHM and yield as a function of eject duration, as in Fig. 5.16. In fact, it was further exploration into the increasing FWHM in this plot that first identified the existence of the two separate short-time bunches. The increase in both FWHM and yield in

Fig. 5.16 was initially observed to occur at around 55.5 μs (see Fig. 5.16), which is in agreement with the current three-Gaussian fit that displays an increase in yield for the secondary bunch at this same eject duration (55.5 μs).

The final bunch is clearly separated from the first bunch by, on average, 10.21 μs, and, as a result, had been excluded from fits since the initial analysis (and so does not contribute to the preliminary results shown in Fig. 5.16). This bunch only appears at longer eject durations, which, in combination with its late arrival time at the detector, indicates that it is composed of the heaviest species of the three. The magnitude of the corresponding peak is significantly less than the two primary peaks, and it exhibits very low yield at short eject durations. As a result, the short-time yield data points corresponding to the third bunch exhibit massive uncertainties in FWHM, and have for this reason been omitted from the FWHM plot on the left of Fig. 5.15.

Despite the large uncertainties, it is possible to extract some information from Fig. 5.15. In particular, we notice that the FWHM values of each of the three bunches are of the same order and appear to plateau at higher eject duration values, indicating that the entire bunch has been extracted from the RFQ cooler/buncher at these eject durations. The yields of the secondary and tertiary bunches clearly increase more significantly over time when compared to the yield of the primary bunch, which is somewhat more stable. This suggests that it is possible to cut out these "contaminant" bunches by setting the eject duration to a short-enough value, which has been observed to be possible experimentally. In fact, for all systematic tests described subsequently in this document, the eject duration has been set such that only the initial, primary bunch is observed and analyzed (as a result, bunches for subsequent systematic tests were fit appropriately by a single skewed Gaussian).

Attempts were also made to determine the composition of the three bunches

by generating detailed models of the entire beam line downstream of the RFQ in SIMION and performing time of flight simulations to compare to the observed time spectra. It was found that adjusting electrode positions by as little as several mm in the simulation could have a significant effect on the outcome of the analysis, changing calculated species masses at the several percent level. Without a perfect understanding of where voltage carrying wires and all individual grounds precisely lay, it was deemed infeasible to predict the species in this way. Further tests will be needed to determine the composition of the three observed bunches. In particular, a radioactive beam and appropriate detection system could be used to verify that each of the bunches was composed, at least in part, of the incident ion species (supported by the fact that all features were eliminated by blocking the incident beam, as discussed above). Additionally, by exchanging the cooling buffer gas (*e.g.* replacing Helium with Argon or Krypton) and observing any changes in the time spectra, molecules forming with the buffer gas could be identified. Such molecules are primary suspects due to the high concentration of reactants [16]. Regardless, these subsequent bunches have been eliminated from the spectra and omitted from analysis in all subsequent tests through a strict time of flight cut on the ion bunches imposed by choosing the minimal eject duration possible in each test. If, in fact, the subsequent bunches are due to compounds formed between the incident ion and other residual species (including the buffer gas), the earliest arriving particles should be identically the ions of interest, as these are the lightest possible particles containing the incident beam.

The drag potential is specified in V/mm and indicates the slope of the axial DC potential superimposed on the RF trapping voltage. It is employed to force the ions to accumulate near the ejection end of the trap. The drag potential is applied to all RFQ segments except for the final two. The penultimate segment has, for all tests

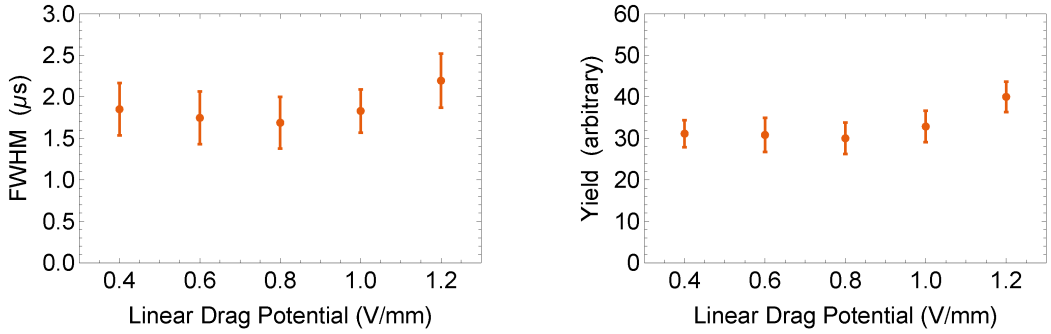

Figure 5.17: Bunch FWHM (left) and yield (right) as a function of DC drag potential. Beam energy = 30 eV, gas pressure = 3×10^{-3} mbar He.

shown here, been held at 5 V lower than the previous segment in order to create a distinct potential well for accumulation, while the final segment voltage is switched between +275 V for bunching and -110 V for ejection. Fig. 5.17, shows the effect of the drag potential on both FWHM of time spread and number of counts per bunch. The FWHM is roughly constant for the drag potentials tested, with a slight increase at higher drag potentials. A higher (more negative) drag potential generates a lower equilibrium ion potential energy for the cooled beam relative to the earth-ground, so that ejected ions have a relatively slower resulting kinetic energy when accelerated to ground, and, as a result, a somewhat extended time of flight. Additionally, though the number of counts per bunch increased slightly with increasing drag potential, it was not possible to observe any ion bunch for a gradient greater than 1.4 V/mm. It is possible that this is due to increased transverse lensing upon ejection, since the exit aperture of the RFQ cooler/buncher has been held at 0 V. Alternatively, this same electrode feature may provide an insurmountable potential wall for escaping ions with too low absolute potential energy.

At the pressures available for operation at TAMUTRAP ($< 5 \times 10^{-3}$ mbar He), increasing pressure has little effect on either the FWHM of time spread or number

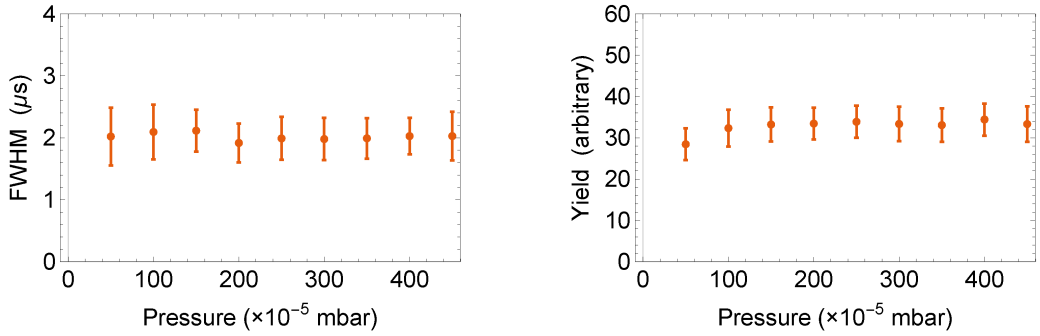

Figure 5.18: Bunch FWHM (left) and yield (right) as a function of buffer gas pressure. Beam energy = 30 eV, drag potential = 0.08 V/cm. Bunches did not form below about 25 mbar He.

of counts per bunch. Very low pressures ($\lesssim 5 \times 10^{-4}$ mbar) reduce the number of observed counts per ion bunch, due to impaired bunching ability in this regime. Fewer collisions with gas particles (a longer mean-free path) at lower pressures reduces the cooling ability of the device, and, as a result, also the ability to form bunches. In general, a reduction in FWHM for increasing pressure is expected as a result of improved cooling capacity (higher pressure); however, as noted, the cooling times used in these tests have generated fully cooled beams in each case. This feature is expected to appear in tests with partially cooled beams. The gas-pressure test makes no comment on the effect this variable has on transverse emittance, which may worsen to some degree with increasing pressure due to gas collisions after ejection. In fact, the beam spot has been noted to appear qualitatively more "diffuse" at higher pressures when viewed on the phosphor screen of the MCP, though no quantitative study has been performed as of yet. The results can be seen in Fig. 5.18.

The a and q parameters indicate the stability of the ion motion in a Paul trap, and are simultaneously dependent on the RF trapping potential and frequency (in addition to the mass of the ions of interest, trap geometry, and other variables). `TAMUTRAP` was designed to operate well within the stability region, at a value of $q \approx 0.6$. For

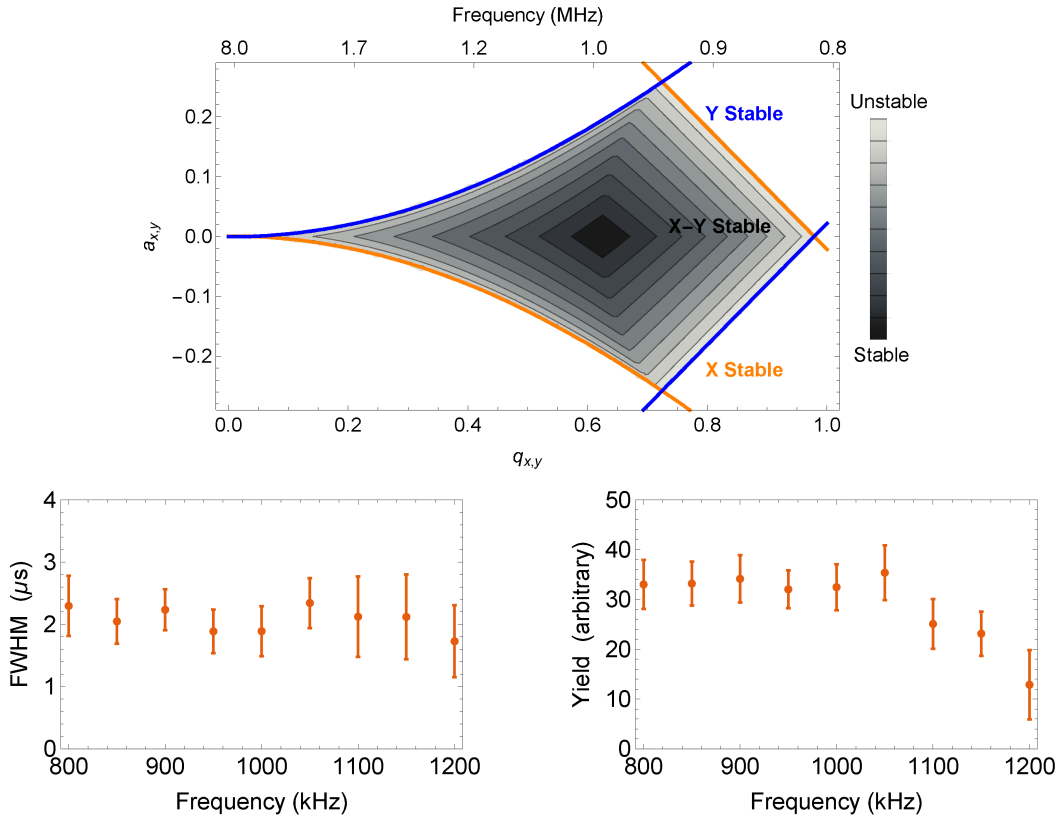

Figure 5.19: Top: The stability diagram for ion motion in the Paul trap assuming the TAMUTRAP cooler/buncher geometry and singly-charged ^{23}Na trapped at 107 V_{PP}. Bottom: Bunch FWHM (left) and yield (right) as a function of RF frequency. Beam energy = 30 eV, gas pressure = 3×10^{-3} mbar He, drag potential = 0.08 V/cm. Peak to peak voltage was held at 107 V.

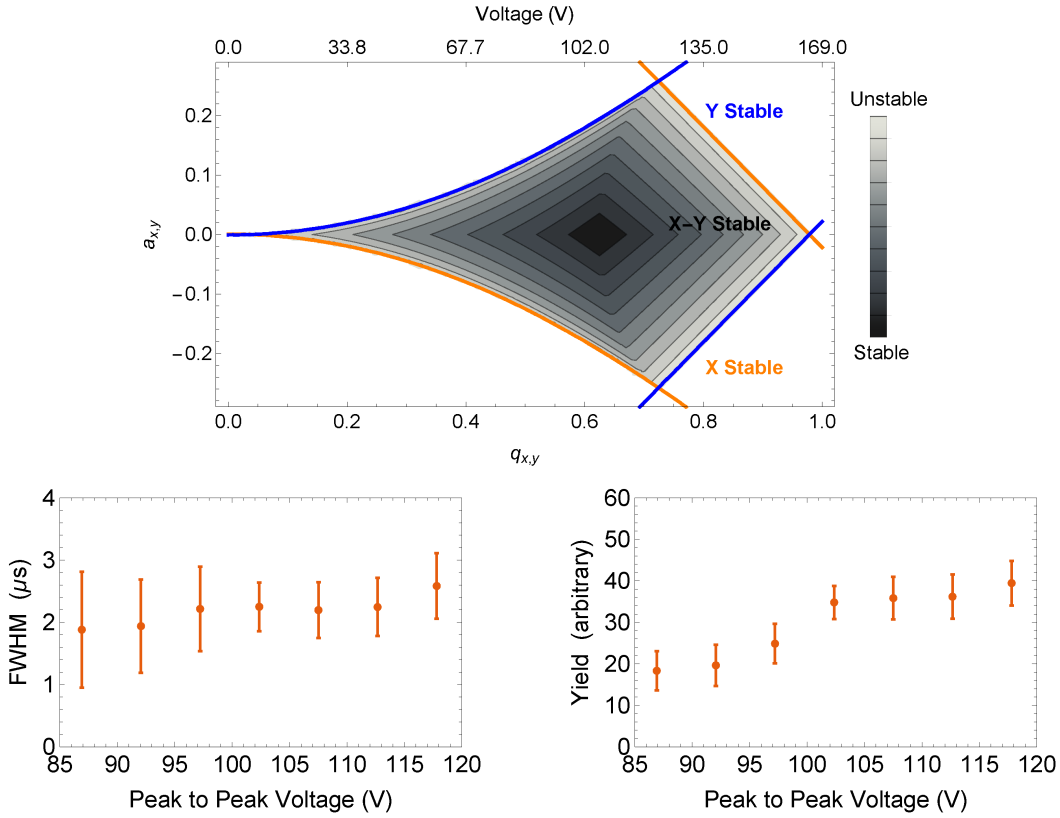

Figure 5.20: Top: The stability diagram for ion motion in the Paul trap assuming the TAMUTRAP cooler/buncher geometry and singly-charged ^{23}Na trapped at 1.0 MHz. Bottom: Bunch FWHM (left) and yield (right) as a function of RF voltage. Beam energy = 30 eV, gas pressure = 3×10^{-3} mbar He, drag potential = 0.08 V/cm. RF frequency was held at 1.00 MHz.

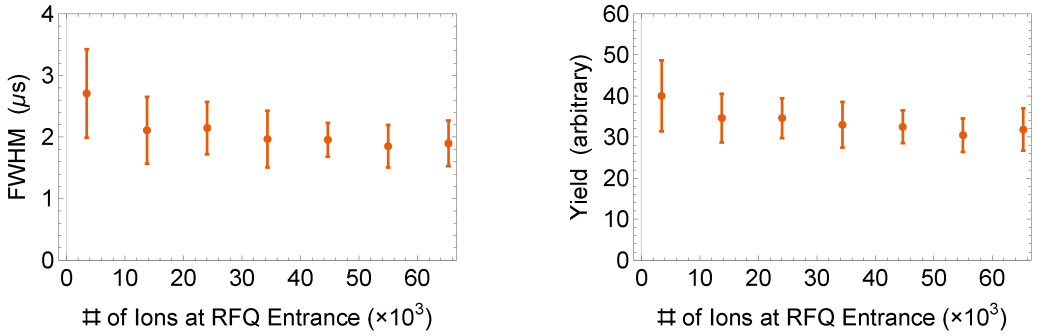

Figure 5.21: Bunch FWHM (left) and yield (right) as a function of incident beam current. Beam energy = 30 eV, gas pressure = 3×10^{-3} mbar He, drag potential = 0.08 V/cm.

the masses of interest and the physical structure of the TAMUTRAP apparatus, this equates to co-dependent ideal values for the peak-to-peak RF trapping potential and frequency in the ranges of 60-120 V and 0.8-1.2 MHz, respectively. Systematic tests were performed to investigate the effect of both frequency (at constant voltage) and voltage (at constant frequency) on bunch characteristics, the results of which are displayed in Figs. 5.19 and 5.20. A local minimum of FWHM for the bunch width was found in both frequency and voltage at 1.00 MHz and 107 V, respectively. A frequency of 1.00 MHz and peak-to-peak voltage of 107 V were also observed separately to roughly maximize the number of counts per bunch, and so are considered to be optimal for trapping the masses present in the offline ion source. Higher peak-to-peak voltages demonstrated larger number of counts per bunch, possibly a result of larger RF forces countering the effective damping force presented by the buffer gas; however, bunch FWHM also increased at larger voltages. Frequencies above 1.15 MHz showed a significant drop in number of counts per bunch, due to less table ion motion at 107 V, as can be seen in the top panel of Fig. 5.19. The left side of the diamond-shaped stability diagram presents as less stable to changes in either voltage or frequency, as evidenced by the yield plots.

The maximum number of stored ions in a Paul trap is reported in the range of 5×10^4 ions per bunch [48] to 1×10^7 ions per bunch [55], and is limited by space-charge effects, or coulomb repulsion, between trapped ions (see Ch. 3). The ions achieve a maximum density due to the competing coulomb repulsion and trapping potentials. As a result, the more ions that are trapped, the larger the ion bunch becomes, such that at some point additional ions can no longer fit in the potential well generated by the device. Using the operating parameters for the TAMUTRAP RFQ with Eq. 3.7 yields a maximum trap density of

$$\rho_{max} = 3.2 \times 10^{11} \text{ ions/m}^3. \tag{5.2}$$

Fig. 5.21 shows the effect of reducing the incident beam current on the FWHM and number of counts per bunch. For this test, the beam was detuned by steering it off-axis such that only about 0.1% of the current measured on the first Faraday cup was delivered to the RFQ. A duty cycle of 50 ms was employed. Above about 1.4×10^4 incident ions, very little effect is observed in either FWHM or number of counts per bunch when increasing the incident beam current. This region is thought to represent a fully saturated trap, *i.e.* the number of incident ions are greater than the capacity of the trap due to space-charge and other effects. Below 1.4×10^4 incident ions, an increase in both FWHM and number of counts per bunch is observed. The increase in FWHM may be attributed to the fact that in an unsaturated bunch higher energy ions may be retained that would be the first ions to be lost in a saturated trap (similar to evaporative cooling).

It was not possible to obtain data with less than 1000 ions loaded into the RFQ due to ion source and duty cycle constraints. Ideally, this regime of incident ion count could be studied more closely. Even so, by taking the space-charge limit at 1.4×10^4

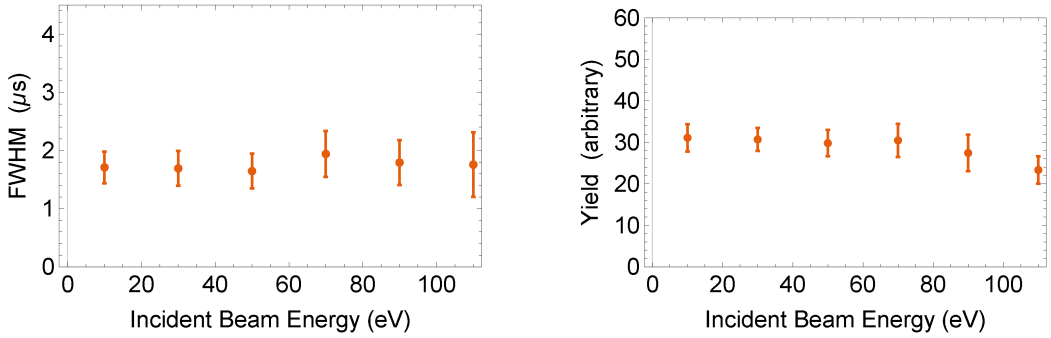

Figure 5.22: Bunch FWHM (left) and yield (right) as a function of incident beam energy. Gas pressure = 3×10^{-3} mbar He, drag potential = 0.08 V/cm.

ions, it is possible to calculate the approximate trap size via the discussion in Ch. 3. According to Eq. 5.2, we conclude that the approximate trap size should be 3.53 mm in any direction, which is reasonable in light of the overall electrode-electrode spacing of 12 mm. It should be noted here that the geometry of the TAMUTRAP RFQ is physically smaller than many other comparable RFQ cooler/bunchers c[55], and so a smaller trap size and maximum number of counts per bunch is not inconceivable.

The detuning method utilized for these tests is very crude, but was required due to the inability of the current ion source to provide a low enough ion rate. Future tests will employ an improved ion source and possibly a current-degrading mesh to obtain a more robust low current beam. As a result, the study presented here should be considered only a rough preliminary investigation into space-charge effects.

A 30 eV incident beam energy demonstrated the greatest continuous mode transmission efficiency of all incident energies tested for an uncooled beam. Since the TAMUTRAP RFQ cooler/buncher will be employed exclusively as a cooler/buncher, it is more critical to determine what beam energy to use in this mode of operation in order to obtain bunches with the smallest FWHM time spread and greatest yield. Fig. 5.22 displays these two bunch attributes as a function of incident beam energy

from 10-110 eV. This was accomplished by raising and lowering the voltage at which the RFQ platform is floated in order to achieve the desired potential difference from the ion source, which was held at approximately 10 kV. Both FWHM of the bunch's time spread and number of counts per bunch are relatively insensitive to the incident beam energy. The data presents a very slight improvement in FWHM around 50 eV beam energy, possibly due to increased acceptance in this regime, which ultimately yields a decrease in FWHM through evaporative cooling, as discussed. At higher incident beam energy, number of counts per bunch decreases slightly, due to a lowered initial capture efficiency of the Paul trap at these energies. However, as with all previously mentioned tests, this measurement was performed near or above the space-charge limit, so the trap may have been saturated in any case, and, therefore could be insensitive to features such as capture efficiency as tested here.

5.4 Present State and Future Work

Initial characterization of the TAMUTRAP RFQ cooler/buncher has been completed, including analysis of the performance of the device in both continuous and bunched modes. Appendix A.1 details the optimized settings for operation in both regimes at several beam energies.

Continuous mode efficiency has been demonstrated as high as 74% at 190 eV, and 60% at the useful incident beam energy of 30 eV. These values compare favorably to those reported in the literature, which quote efficiencies between 30-70% in continuous mode [17].

Characterization of bunched mode operation was limited to some degree by the stability of the ion source as well as its lower current limit. Despite this, some systematic tests were performed to characterize the resulting bunches, and the optimum operating configuration for several beam energies and gas pressures was determined.

Bunches $\leq$1.8 μs FWHM in time spread could be produced repeatably. Though this value missed the original design goal of the device, it is still more than suitable for the initial measurements of interest for which trapping in the Penning trap and high transport efficiency are the only requirements. Additionally, as discussed, if the resulting bunches are fit with standard Gaussians as opposed to skewed Gaussians (a practice which is common in the literature), the achievable FWHM reduces to $\approx$1 μs, matching the design goal of the device, and also comparing favorably to world class facilities such as devices located at the ISOLTRAP [26, 17], SHIPTRAP [48], and TITAN [55] experiments.

Though the TAMUTRAP RFQ cooler/buncher has been shown to supply satisfactorily bunched beam for the initial measurements of interest, there is still some work that should be done before moving on to further tasks. In particular, additional characterization that was not feasible in the time frame of the current tests should be undertaken to complete the picture of device operation, and some minor improvements should be made in the future.

Three additional tests need to be performed to gain a more complete characterization of the TAMUTRAP RFQ cooler/buncher. First of all, the exact identification of the individual ion bunches should be made clear. As observed when varying eject duration, up to three significant bunches could be observed in a single ejection. It is believed that these correspond to heavier molecular contaminants with the ion species of interest (as discussed); however, this can be further confirmed by employing radioactive beam and appropriate detectors and by systematically testing the effect of different buffer gases on th time spectra.

Second, the transverse emittance of the cooler/buncher should be investigated. As discussed in Ch. 4, a Pepper pot emittance device has been designed and assembled for this purpose. Software has also been written to acquire and analyze data.

The emittance station is ready for commissioning, and later implementation in the TAMUTRAP beam line.

Finally, in order to develop a full picture of the longitudinal emittance, information on the entire phase space of the beam is required, not just the time or (equivalently) spatial components that have been detailed above. To do this, a measure of the longitudinal energy spread of the beam should be performed. This was not feasible so far due to the time and energy costs necessary to develop an appropriate an energy spectrometer. The simplest means of characterizing the energy spread would be via an electrostatic "blocking voltage" technique as employed by Rubiales at SHIPTRAP [48]. Such a method involves ramping the potential on a blocking electrode placed upstream of the primary bunch detector and recording the rate on the detector as a function of blocking voltage, yielding an integrated energy spectrum. The resulting spectrum can then be used to determine the energy spread in the bunch. This technique will require additional electrode structures, power supplies, and improved acquisition relative to what is currently available.

Even though the TAMUTRAP RFQ has performed satisfactorily as far as can be ascertained with the current investigation techniques, some improvements, which have been hinted at in the above sections, have been identified to enhance the operation of the device. First, more precise testing of the device will be facilitated by an offline source with greater stability in current output. As mentioned, the present device is voltage regulated and directly coupled to any fluctuations in AC line voltage. As a result, the beam current fluctuates by as much as 10% over the seconds to minutes timescale. It is believed that switching to a current limited supply could solve this problem, greatly improving the stability of the source. Too further enhance low-rate stability, a degrader mesh may be implemented downstream of the improved source to physically and reliably reduce the beam current. These two advancements

would improve the precision of all measurements reported here, and give a much better idea of the space charge limits of the device, which are particularly sensitive to fluctuations in the current.

Next, though the mechanical design allows for adjustable injection and extraction voltages, these electrodes are unable to be consistently floated to any potential other than the platform ground, which could effect the physical beam envelope or divergence through lensing. Ultimately, transverse emittance tests will indicate how critical it is to resolve this issue, though some thought should be dedicated to discovering a solution, regardless. The injection and extraction electrodes are connected directly to individual channels of a Weiner low voltage multi-channel module. Each plate is also capacitively coupled to ground, since both had been observed to pick up some RF from the adjacent RFQ segments. The failure mode is characterized by an eventual shorting to ground of the electrodes under consideration, with any attempt to raise or lower their voltages yielding a DC current at the limit of the power supply (and no change in measured voltage). This only happens sporadically, such that the plates may hold a set voltage for a significant amount of time. For the above tests, the diaphragms have been set to 0 V relative to the platform ground, and have yielded suitable bunching time spreads and efficiencies in this configuration.

Another unforeseen shortcoming of the RFQ electronics is characterized by the minimum achievable cooling time. Switching the DC offset on the last segment of the RF structure effectively transports electrons from the negative supply to the positive supply through the Behlke ultrafast switch, with the segments themselves playing the role of the intermediate charge storage medium. The maximum rate at which the switching is required is around the low millisecond time regime (the minimum amount of time for a completely cooled bunch), and the potential difference applied has been 385 V in these tests (+275 V−(−110) V). In this realm and for the voltages

in question the problem may be simplified by considering only the contribution to the impedance of the low frequency capacitance. Here the equation for the charge held by the electrode structure is simply $q = CV$, such that the current is given by $I = CVR$, where R is the number of bunches per second (*i.e.* the number of switches of the Behlke unit per second, or the number of times charge is transported between power supplies per second). The power supply begins to trip at a current of 1 mA, at 12.5 ms per cycle. This yields a theoretical capacitance of 32 nF for the last segment of the RFQ, which is confirmed by a measurement of 37 nF with a multimeter. To achieve higher repeat rates, either the capacitance of the last segment must be reduced (which is not feasible without significant re-design), or the power supplies serving this last segment must be replaced with higher current units. Any factor improvement in the maximum power supply current will yield a corresponding improvement in bunching duty cycle.

The time spread of the bunch has been shown to be in the low microsecond range, depending on various settings, which is considered suitable for loading into the ultimate `TAMUTRAP` measurement Penning trap. As a result, no improvement in bunching characteristics is deemed necessary; however, it could be possible to tighten the ion bunch by dropping the final segment potential wall more quickly. As discussed in the preceding sections, the ejection wall empirically takes around 50 μs to drop low enough to allow the bunch to eject, despite the switch itself exhibiting fall times on the order of 500 ns. The non-negligible impedance of the last segments with the surrounding material and the low-pass protection circuit are thought to be the causes of this extended fall time. It has been observed that the total fall time of the system when connected to the segments is independent of voltage (*i.e.* a 500 V different is eclipsed in the same time taken for a 200 V difference), so one possible solution is to increase the positive and negative voltages that the wall is held

at during cooling and ejection, respectively. The problem with this solution is that the improvement is linear with the voltages applied, and at some point, increasing the voltage will become untenable. The other possible solution to this problem is to modify the low-pass circuit to minimize the impedance of the system driven by the Behlke switch, or to locate and remove additional sources of impedance in the system (though this may again require some redesign).

In the bunched studies performed so far, an increased gas pressure within the RFQ yielded better bunch properties with no significant decrease in observed efficiency (though many of these tests were carried out near the space-charge limit). In order to access even higher gas pressures inside the RFQ while maintaining suitable pressures in the adjacent beam line (where additional gas can lead to spreading of the beam envelope and deteriorating of the bunch), additional pumping will be required. Currently, two 1000 L/s turbo pumps service the beam line connecting to the RFQ. These pumps must maintain vacuum and exhaust the He gas used for beam cooling that escapes through the RFQ diaphragms. With the current set up it is possible to maintain 5×10^{-3} mbar He in the RFQ while keeping the beam line in the required 10^{-6} mbar range. Improving the pumping outside the RFQ would allow access to even higher gas pressures (and, as a result, lower cooling times and higher repetition rate, all else equal). Additionally, a significant pressure gradient from the pressure used in the RFQ to the nominal beam line pressure is expected between the diaphragms on the RFQ chamber and the nearest pump. These distances are on the order of 1 m on either side of the RFQ, which leaves significant room for the incoming beam and ejected bunch to undesirably interact with residual gas particles, hurting injection efficiency and deteriorating the bunch shape through unwanted collisions. Improvement in either pumping speed or pump placement in the future could only improve performance of the TAMUTRAP RFQ.

Finally, though the analog electronics that currently generate the trapping RF potential for the TAMUTRAP RFQ provide access to sufficient frequency and voltage ranges to extensively explore the regions of stable device operation for the given masses and electrode geometry, additional RF power and frequency availability would only make the trap more flexible. The current electronics allow for the trapping of singly charged ions up to Rb in the center of the stability region (+1 Rb requires approximately 150 V_{pp} for the TAMUTRAP geometry at 1.1 MHz). If future tests require heavier masses to be processed by the RFQ, higher voltage will be required. Additionally, motion in a gas filled trap deviates from motion in an ideal Paul trap due to the effective resistive force imposed by gas collisions. Because of this, at higher operating gas pressure, voltage in excess of the ideal trapping voltage may be required to contain ions of interest. For these reasons, upgraded electronics are already being considered for the TAMUTRAP RFQ cooler/buncher based upon solid-state digital circuitry and able to achieve roughly 1 kV peak-to-peak in the desired frequency range [**?**]. These electronics should be evaluated along with the likelihood of increased gas pressure and higher mass trapping requirements at the TAMUTRAP RFQ.

In conclusion, the TAMUTRAP RFQ cooler/buncher performs to its own design specification and at the level of other similar facilities in the attributes that have been probed in this initial characterization. Optimized operating parameters for device usage can be found in Appendix A.1. Though the device has proved satisfactory so far, additional tests are required for a complete characterization that were not feasible given the resources available, and several improvements have been noted for future consideration.

6. THE MEASUREMENT TRAP*

For the reasons mentioned in Ch. 3, a cylindrical geometry, illustrated in Fig. 6.1, has been chosen for the TAMUTRAP measurement Penning trap [37]. This particular geometry has been optimized to create a design that is suitable both for the precision β-decay experiments of interest, as well as a wide range of nuclear physics experiments. Specifically, the design displays a large-bore for containment of decay products, it allows for the placement of biased detectors at either end for observation of these products, and it exhibits a tunable and orthogonalized geometry in order to achieve a harmonic electric field.

Such a design had not previously been employed by any Penning trap facility, so a new geometry for the electrode structure was developed from first principles, and is presented here [37]. The analytic calculations have been performed in the spirit of [21]; however, without implementing the long-endcap approximation. This resulted in a new analytic Penning trap design, for a short, large diameter, compensated, and orthogonalized Penning trap, which will be discussed in this chapter.

6.1 Design Considerations

For $\beta - \nu$ correlation measurements, the Penning trap must have a free diameter large enough to contain the decay products of interest within the electrodes via the cyclotron force imposed by the trapping magnetic field. The initial program of measuring $a_{\beta\nu}$ will investigate the $T = 2$ nuclei shown in Table 3.1, by observing the proton energy distribution. To contain protons of interest with near full 4π

*Reprinted in part with permission from "Design of a unique open-geometry cylindrical Penning trap" by M. Mehlman, P.D. Shidling, S. Behling, L.G. Clark, B. Fenker, and D. Melconian, 2013. Nuclear Instruments and Methods in Physics Research Section A: Accelerators, Spectrometers, Detectors and Associated Equipment, 712, 9-14, Copyright 2013 by Elsevier B.V.

acceptance, the trap radius is set to twice the cyclotron radius of the most energetic expected proton within the 7 T magnetic field provided by the Agilent 7T 210 ASR magnet [2]. As a result, the inner radius of the electrode structure was chosen to be 90 mm, which will fully contain protons of up to 4.75 MeV decay energy. The highest energy proton of interest anticipated in the initial program is the 4.28 MeV proton resulting from the β-delayed proton decay of ^{20}Mg, which exhibits a 42.7 mm cyclotron radius. As a result the 90 mm inner radius was deemed safe for the entire envisioned initial program. This radius will be the largest of any existing Penning trap and will additionally easily contain the less magnetically rigid β's, and even the slow, low energy recoils, for the initial $a_{\beta\nu}$ studies.

The other primary requirement for performing the mentioned correlation measurements is that the design must ultimately accommodate position sensitive strip detectors at either end of the trap. The charged decay products (β, p, recoil ion) exhibit cyclotron motion in the radial directions and linear motion in the axial direction contained completely within the bore of the Penning trap. This motion results in a helical orbit progressing toward either end of the trap, until the products are detected at the endcap, as discussed in Ch. 3. For this work, the detectors have been simulated separately as disk-shaped "endcap electrodes," which satisfies the need to bias the detectors at an arbitrary potential not necessarily equal to that of the cylindrical end electrodes, while understanding the effect of this voltage on the overall electric field.

In an imperfect quadrupole potential, oscillation frequency is dependent on the amplitude of the oscillation. As a result, different frequencies may be recorded for particles exhibiting different kinetic energies, since these particles naturally observe different oscillation amplitudes. Having a well-understood highly quadrupolar field therefore gives great flexibility to an ion trap, allowing it to be not only useful for

confinement, but also for any measurements that involve ultra-precise frequency determination. For this reason, a priority for the TAMUTRAP facility is to attain a very good quadrupole field at the center of the measurement Penning trap. To achieve this, the trap design must be tunable, that is, it must make use of compensation electrodes that serve to adjust the field shape, since a simple cylindrical electrode geometry does not generate an inherently quadratic electric field (this is only accomplished naturally with a perfect hyperbolic geometry). Other cylindrical traps [45, 43] already employ tunable geometries; however, these configurations were not suitable for TAMUTRAP due to the large-bore requirement. Enlarging any existing geometries (a process that does not inherently affect the field shape if all features are scaled appropriately), results in a trap too long to fit within the available 7 T magnet. The existing designs cannot be compressed length-wise since the analytic solutions of the electric field used to design these traps [21] directly employ long-endcap approximations, which are only valid for long trap-length as compared to the inner radius (a feature TAMUTRAP explicitly wants to avoid). As a result, a new design utilizing the existing field calculations is not applicable to the short-endcap / large-bore requirements necessitated by the envisioned TAMUTRAP experimental program, and, for this reason, original electric field calculations removing such approximations have been performed.

6.2 Orthogonalization

In this section, a new analytic solution for a short-endcap, tunable Penning trap will be defined (for greater detail, please see Appendix B). The electric field was derived from first principles, in part following the discussion in Ref. [21]. The contribution to the potential due to the various electrodes (Fig. 6.1) can be found by noting that any potential may be expanded in terms of the Legendre polynomials, P_k, the

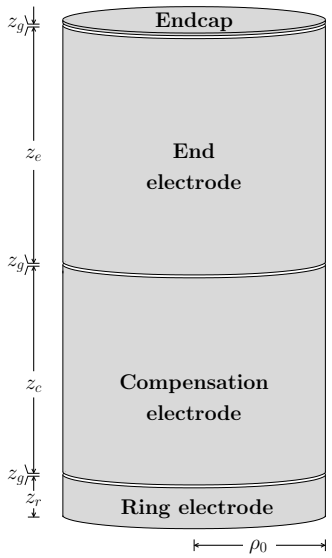

$\boldsymbol{\phi_0}$ $\rho = \rho_0$	$\boldsymbol{\phi_1}$ $\rho = \rho_0$	$\boldsymbol{\phi_2}$ $\rho \leq \rho_0$
0	0	1
0.5	0	0
0	1	0
-0.5	0	0

Figure 6.1: The trap geometry and boundary conditions used in the analytic solution. The device is symmetric about the $z = 0$ plane.

potential depth, radius from the trap axis, and characteristic trap distance [21], V_0, r, and d, respectively, and the expansion coefficients, C_k (k is even due to symmetry across the trapping plane):

$$V = \frac{1}{2} V_0 \sum_{\substack{k=0 \\ k \text{ even}}}^{\infty} C_k \left(\frac{r}{d}\right)^k P_k(\cos\theta), \tag{6.1}$$

with

$$d = \sqrt{\tfrac{1}{2}\left[(z_r + z_g + z_c + z_g)^2 + \tfrac{1}{2}\rho_0^2\right]}. \tag{6.2}$$

Here z_i is defined as in Fig. 6.1 and ρ_0 is the inner radius of the trap electrodes. By superposition, the potential at the trap center may also be written as a sum of the

potentials of each of the contributing electrodes:

$$V = V_0\phi_0 + V_1\phi_1 + V_2\phi_2. \tag{6.3}$$

Here, ϕ_0 is the potential generated by the ring and end electrodes (the primary potential well), and ϕ_1 and ϕ_2 are from the compensation and endcap (detector) electrodes respectively (Fig. 6.1), while the V_i's are the electrical potentials at which the electrodes are held. Each of the ϕ's can in turn be expanded in Legendre polynomials and substituted back into Eq. 6.3, which yields the simple result:

$$C_k = D_k + E_k\frac{V_1}{V_0} + F_k\frac{V_2}{V_0}, \tag{6.4}$$

where D_k, E_k, and F_k are the individual expansion coefficients due to the ring and end electrodes, compensation electrodes, and endcap (detector) electrodes respectively, and must be solved for individually. D_k and E_k, which are due to hollow cylinder shaped electrodes, can be found by expanding ϕ_0 and ϕ_1 in Bessel functions, J_α. After applying the periodic boundary condition in z, $\phi(z) = \phi(-z)$, it can be found that

$$\phi_i = \sum_{n=0}^{\infty} A_n J_0(\imath k_n \rho)\cos(k_n z), \tag{6.5}$$

where A_n is an additional expansion coefficient. Here k_n is due to the periodic boundary condition, and is given by

$$k_n = \frac{(n+\frac{1}{2})\pi}{z_{\text{tot}}}, \tag{6.6}$$

where $z_{\text{tot}} = z_r + z_c + z_e + 3z_g$. Setting Eq. 6.5 equal to the expansion in Legendre polynomials (Eq. 6.1) allows one to solve for the coefficients of the Legendre

polynomials by equating the two along $\hat{z}$. This results in the following solutions:

$$\begin{aligned} D_k &= \sum_{n=0}^{\infty} \frac{2A_n^D d^k k_n^k (-1)^{k/2}}{k!} \\ E_k &= \sum_{n=0}^{\infty} \frac{2A_n^E d^k k_n^k (-1)^{k/2}}{k!}. \end{aligned} \tag{6.7}$$

The coefficients A_n^i are subsequently determined by applying the appropriate boundary conditions (Fig. 6.1) along with the orthogonality of cosine, yielding

$$\begin{aligned} A_n^D &= \frac{(-1)^n - \sin[k_n(z_r + z_g + z_c + z_g)] - \sin(k_n z_r)}{k_n z_{\text{tot}} J_0(\imath k_n \rho_0)} \\ A_n^E &= \frac{2\big(\sin[k_n(z_r + z_g + z_c)] - \sin[k_n(z_r + z_g)]\big)}{k_n z_{\text{tot}} J_0(\imath k_n \rho_0)}. \end{aligned} \tag{6.8}$$

The contribution to the potential from the endcap electrodes must be handled differently. Here ϕ_2 is defined at z_{tot} for any radius less than ρ_0. After simplifying due to the cylindrical symmetry of the system, ϕ_2 can be written:

$$\phi_2 = \sum_{n=0}^{\infty} J_m(k_{0n}\rho) e^{k_{0n} z} B_n, \tag{6.9}$$

where, k_{mn} is related to x_{mn}, the n^{th} zero of the m^{th} Bessel function as in

$$k_{mn} = \frac{x_{mn}}{\rho_0}. \tag{6.10}$$

Since Bessel functions of the first kind oscillate indefinitely around $J_m(x) = 0$ as x increases, such a zero, x_{mn}, will necessarily exist. B_n can now be determined through the application of appropriate boundary conditions (see Fig. 6.1) and the

Bessel function orthogonality relation, giving

$$B_n = \frac{2e^{-k_{0n}z_{\text{tot}}}}{x_{0n}J_1(x_{0n})}. \tag{6.11}$$

Taking into account both endcaps (at $\pm z$) yields the complete formulation of the potential due to the endcaps at any z:

$$\phi_2 = \frac{V_2}{2}\left[\sum_{n=1}^{\infty} J_0\left(\frac{x_{0n}}{\rho_0}\rho\right) e^{z\frac{x_{0n}}{\rho_0}} \frac{2e^{-k_{0n}z_{\text{tot}}}}{x_{0n}J_1(x_{0n})} + \sum_{n=1}^{\infty} J_0\left(\frac{x_{0n}}{\rho_0}\rho\right) e^{-z\frac{x_{0n}}{\rho_0}} \frac{2e^{-k_{0n}z_{\text{tot}}}}{x_{0n}J_1(x_{0n})}\right]. \tag{6.12}$$

This result for the potential was subsequently Taylor expanded using `Mathematica` [64], yielding coefficients which may be referred to here by T_k. Setting the result from the expansion equal to the potential expanded in Legendre polynomials along the z-axis and equating terms yields the final result for the coefficients F_k:

$$F_k = V_0 T_k d^k. \tag{6.13}$$

All expansion coefficients from Eq. 6.4 have now been completely defined, and the electric field at the trap center can be specified to arbitrary precision. By construction, it is easy to characterize the components of this field, which allows for a straightforward optimization.

6.3 Optimization

For certain experiments (such as precision mass measurements), it is crucial to be able to minimize the anharmonic terms ($C_{\geq 4} \to 0$) of the electric field during the course of a measurement without affecting the harmonic (C_2) component of the

field. In order to achieve this for TAMUTRAP, the procedure discussed in Ref. [21] was followed.

The strength of the dominant anharmonic term for the superposition of the electric fields is given by the coefficient C_4, and the second most dominant contribution comes from C_6, which has an effect on the shape of the electric field smaller than C_4 by a magnitude of $(r/d)^2$ (where r is that radius of ion motion and d is the characteristic trap dimension) [21]. These coefficients are determined, in turn, by the anharmonic contributions from the constituent electrodes, that is, D_4, D_6, E_4, E_6, F_4, and F_6. C_4 may always be made negligibly small by adjusting the potential on the compensation electrodes until the field is essentially harmonic. For a general geometry, however, this procedure will affect the value of C_2. Since only the potentials of the compensation electrodes are adjusted in this process, it is possible to eliminate this affect by requiring that $E_2 = 0$, *i.e.* by requiring that the compensation electrodes have no influence on the harmonic term of the superposition, C_2.

The expansion coefficient E_2, which is a function of the entire geometry, was minimized using the analytic solution derived above. To do this, physical constraints imposed by measurement considerations, assembly requirements, etc. were first imposed. This left three free parameters: ring electrode length, compensation electrode length, and end electrode length. Ring electrode length and end electrode length were chosen in order to both minimize C_6 and achieve a large tunability with respect to C_4, where tunability is described in Ref. [19]:

$$\text{Tunability} = V_0 \frac{dC_4}{dV_1}. \tag{6.14}$$

After determining the ring and end electrode lengths, E_2 was minimized with respect to the remaining parameter, the compensation electrode length, thereby orthogonal-

izing the geometry. Since E_2 changes sign when scanning over electrode length, it was possible to choose a geometry that resulted in an arbitrarily small value for E_2.

The resulting geometry is shown in Fig. 6.2. The trap radius is 90 mm, which is larger than in any existing Penning trap. The ring electrode length is 29.17 mm; the compensation electrode length is 71.36 mm; the end electrode length is 80.00 mm; and 0.50 mm gaps have been accounted for. This geometry yields a length/radius ratio of $l/r_0 = 3.72$. A good quadrupole field ($C_4 = -6.8\times10^{-6}$, $C_6 = 6.2\times10^{-6}$) has been calculated to be achievable with compensation electrodes set to $V_1 = -0.373V_0$ (where V_0 is the primary trap depth). The analytic expansion of the electric field around the trap center up to C_8 is shown in Table 6.1. Changing the voltage on the endcap electrodes (detectors) will adjust the predicted tuning (compensation) voltage; however, the trap will always remain tunable and orthogonalized since the contributions to the potential for each electrode are independent by superposition.

6.4 Simulation with `SIMION`

The analytic solution for the proposed geometry was verified using `SIMION` [50], an electric field and ion trajectory simulation program, in order to confirm the validity of the calculations. The results from `SIMION` are listed in Table 6.1 (along with the analytic solutions from §6.3), and the resulting equipotential lines have been overlayed on the geometry cross section presented in Fig. 6.2. The values output by `SIMION` agree with the analytic solutions for each C_k to a few parts in 10^{-3}. The discrepancies between the analytic and simulated values can be accounted for by the inherent pixelation of the geometry as represented in `SIMION` and processing constraints, which have both been minimized as far as allowed by RAM and available computing time. Specifically, the optimized geometry has been represented in the simulation to the nearest 0.01 mm, and the voltages have been defined to 1×10^{-3} V.

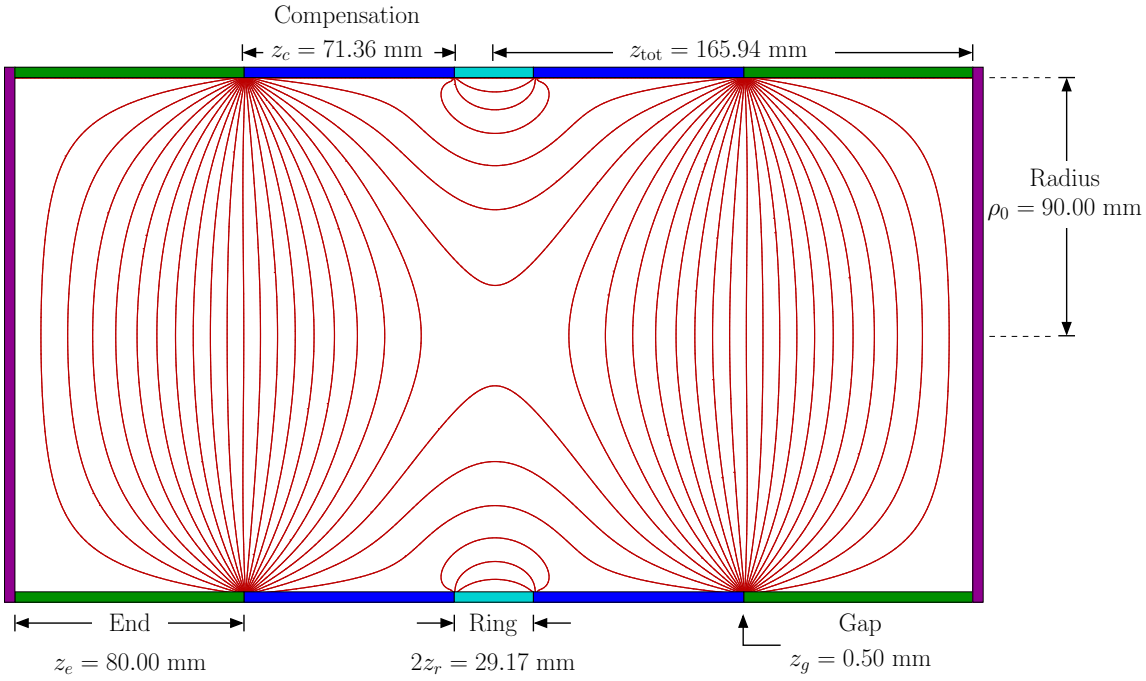

Figure 6.2: The optimized trap geometry with SIMION generated electric fields lines overlayed.

C_i	TAMU Analytic	TAMU Simulated	TITAN Analytic	PENTATRAP Analytic	LEBIT Simulated
C_0	-5×10^{-1}	-5×10^{-1}	-	-	8×10^{-1}
C_2	5×10^{-1}	6×10^{-1}	-	-2×10^{-2}	1
C_4	-7×10^{-6}	9×10^{-4}	-7×10^{-6}	4×10^{-6}	2×10^{-3}
C_6	6×10^{-6}	-3×10^{-3}	5×10^{-5}	2×10^{-7}	-4×10^{-3}
C_8	-4×10^{-2}	-4×10^{-2}	-	-1×10^{-1}	3×10^{-3}

Table 6.1: Expansion coefficients are compared for the optimized TAMUTRAP measurement trap when tuned (analytic and simulated) and three other existing Penning traps: TITAN (calculated analytically as in Ref. [11]), PENTATRAP (calculated analytically as in Ref. [45]), and LEBIT (simulated using SIMION as in Ref. [47]).

6.5 Comparison to Existing Traps

The defining features of the TAMUTRAP geometry described here are the unique inner radius (90 mm), the small length/radius ratio ($l/r_0 = 3.72$), and the consideration made for detectors (short endcap electrodes). This new l/r_0 ratio is what allows TAMUTRAP to exhibit such an unprecedented radial size when compared to other cylindrical Penning traps, while still measuring only 335 mm in overall length. The optimized ISOLTRAP cooler trap geometry, for example, has an $l/r_0 = 11.75$ [43], and would therefore require over 1 m in length in order to maintain geometrical proportions (and, therefore, electric field shape) with a 90 mm inner radius. The compact geometry employed by TAMUTRAP allows for a structure with a very large radius to easily fit within the 1 m long bore of the 7T 210 ASR magnet. At the same time, the new analytic solution described in §6.3 retains the quadrupolar nature of the electric field displayed by other prominent Penning traps, which is required for high-precision frequency measurements, such as precision mass measurements.

Table 6.1 compares the analytic and simulated electric field expansion coefficients of TAMUTRAP to analytic solutions reported by LEBIT [47] and PENTATRAP [45], and a simulated solution reported by TITAN [11]. The suppression of the anharmonic terms in the electric field generated by the geometry for the TAMUTRAP measurement Penning trap is comparable to that presented by these three prominent mass-measurement facilities, for which a very well-tuned harmonic electric field is critical [20]. With respect to the inherent field shape, the TAMUTRAP geometry should therefore be suitable for such precision mass measurements; however, it remains to be seen what effects the unprecedented electrode size and trapping volume necessitated by the primary program of performing $\beta - \nu$ correlation measurements will have on the specific procedures required in these studies. In particular, one foreseeable

challenge due to the enlarged geometry is achieving high uniformity of the applied potentials across the electrodes, though it is currently not known whether or not this effects will ultimately limit mass resolution.

One additional concern for precision measurement facilities is deviation of the physical geometry from the calculated geometry in terms of magnetic field inhomogeneities, misalignment of the electrode structure with respect to the magnetic field, and machining and assembly imperfections. For mass measurements, precision manufacturing and assembly and a careful systematic study of the system can allow for ultimate mass uncertainty on the order of $\delta m/m \sim 10^{-9}$, which is sufficient for the investigation of nuclear structure, the -r, -rp, and -νp processes, halo nuclei charge radii, and testing of CVC ([12] and references therein). Construction techniques and systematic analyses have been well documented in the field (see [11, 12, 20, 9]), and will be similarly employed at TAMUTRAP. Again, the effect of the enlarged geometry of the TAMUTRAP electrode structure may cause further complications that could decrease the ultimate attainable mass precision; however, in any case, these effects will not have a significant impact on the main experimental program where the quality of the trap is not as stringent.

6.6 Geometric Efficiency

In addition to electric field and overall size considerations, one must consider the geometric acceptance of the proposed geometry for the products of interest. Here, we shall consider only the protons, which range in centroid energy from 1.23 MeV for ^{48}Fe to 4.28 MeV for ^{20}Mg. The electric fields of the trap, which are on the order of tens to hundreds of volts, will be ignored here, as they are insignificant when compared to the MeV energies of the protons.

The same magnetic field that is used to confine the parent ions in the Penning

trap affects the trajectory of the resulting protons, since these products of interest are also charged. The resulting cyclotron motion involves a periodic return to the z-axis radially, coupled with a constant velocity in $\hat{z}$ depending on the initial velocity vector of the particle. This yields a helical trajectory, which passes periodically through $\rho = 0$. Since the trap design allows for entrance and exit apertures of finite size on $\rho = 0$, an unexpectedly large fraction of protons of interest may escape through these apertures at either end rather than being detected, relative to the small cross-section of these apertures in terms of the entire assembly.

To assess this effect, we must calculate at what radius, ρ, the proton of interest will strike the endcap (or detector) for a given proton energy. It will be assumed that the angular distribution of protons relative to the trap geometry is isotropic. It is easy to determine the position of the proton as a function of time in one of the direction orthogonal to the trap axis:

$$\rho = v_p \sin(\theta) \frac{m_p}{q_p B} \left(\cos\left(\frac{q_p B}{m_p} \cdot t \right) + 1 \right). \tag{6.15}$$

Here, ρ is the distance from the trap axis, v_p, m_p, and q_p are the velocity, mass, and charge of the proton, respectively, θ is the initial angle of the proton with respect to the z-axis, B is the strength of the confining magnetic field, and t is the time of flight. However, the component of the proton's velocity that is along the z-axis will determine the total time of flight of the proton. From this, the radial position of the proton as a function of trap half-length, d, is found to be,

$$\rho = v_p \sin(\theta) \frac{m_p}{q_p B} \left(\cos\left(\frac{q_p B}{m_p} \cdot \frac{d}{v_p \cos(\theta)} \right) + 1 \right). \tag{6.16}$$

At this point, all that remains is to determine the fraction of protons that are

detectable at the endcaps of the trap. There are two reasons why a proton may not be detected. First, the radius of the proton may be less than the radius of the entrance or exit aperture at the location of the endcap, which can be determined by the above calculations for a given geometry. Or, second, the proton may arrive at the endcap with too shallow of an angle to be detected reliably. The effect of these two scenarios can be combined as:

$$\text{Efficiency} = \int_{\cos(\theta_0)}^{1} F\left(\cos^{-1}(\mu), v_p, m_p, q_p, B, d\right)\, \mathrm{d}\mu, \tag{6.17}$$

where

$$F(\theta, v_p, m_p, q_p, B, d) = \begin{cases} 0, & \text{if } \rho_0 > v_p \sin(\theta) \frac{m_p}{q_p B} \left(\cos\left(\frac{q_p B}{m_p} \cdot \frac{d}{v_p \cos(\theta)}\right) + 1\right) \\ 1, & \text{otherwise.} \end{cases} \tag{6.18}$$

Here, a change of variables has been made from θ to μ to account for the isotropic distribution of protons. In Eqs. 6.17 and 6.18, ρ_0 is the cutoff for radial acceptance of the endcap detectors and θ_0 is the cutoff for glancing angle (protons that hit the endcap with an angle shallower than θ_0 are assumed lost).

In this way, a study of the geometric acceptance of a proposed Penning trap may be examined as a function of trap half-length, as in Fig. 6.3. For an aperture radius of 2 mm and ignoring protons that come in shallower than 10 degrees to the endcap detector, a maximum of about 80% efficiency is observed, which varies both over trap half-length and proton energy.

This geometric efficiency can be improved by artificially increasing the magnetron radius of the trapped particle through resonant excitation. Such a procedure would result in a larger trap size; however, decays would no longer occur from $\rho = 0$,

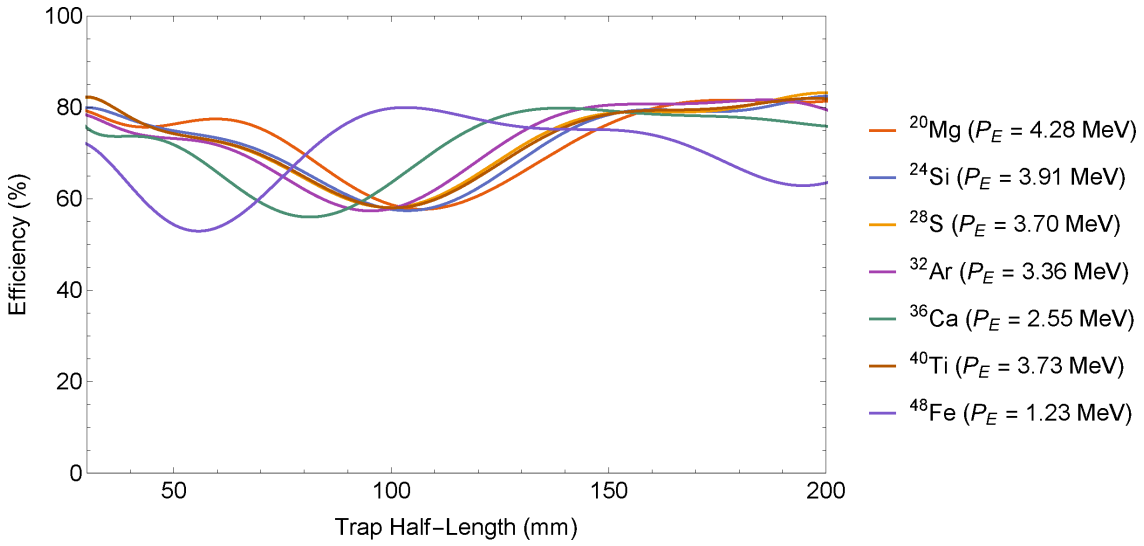

Figure 6.3: Sample geometric efficiency for collecting protons resulting from superallowed decays of interest as a function of trap half-length. For this plot, the entrance and exit apertures are assumed to be 2.4 mm, magnetic field strength is 7 T, and the trap is symmetric about the $Z = 0$ plane.

reducing the effect described above. While this approach has been discussed, no additional work has been done to develop the improved injection scheme at the time of this writing, and so it is important to consider the limitations of the traditional approach for this experiment.

6.7 Present State and Future Work

A tunable analytic design for the TAMUTRAP measurement Penning trap exhibiting a very short endcap structure has been developed from first principles. The geometry has been optimized to generate a highly quadratic electric field, which will endow the TAMUTRAP measurement trap with great future flexibility as either a simple confinement tool for ions of interest, or as an apparatus facilitating ultra-high precision frequency measurements. Both the analytic solution and electric field simulations have been shown to compare favorably to values published by world-class facilities for precision Penning traps. Additionally, an analytic approach to determining geo-

metric efficiency of such a geometry for the decays of interest has been investigated, indicating the fraction of ions lost through the injection diaphragm of the device. It has been noted that this loss of efficiency may be remedied by an initial ion excitation before any measurements take place.

The solution presented above has been shown to be suitable for the measurements of interest, in addition to frequency measurements that are not specifically anticipated at this time; however, the initial beta-neutrino correlation parameter measurements envisioned for the TAMUTRAP facility will only require simple confinement from the measurement Penning trap, which can be achieved in a simpler, three-electrode configuration. For this reason, it remains to be seen whether the added flexibility of the unique trap described here merits the additional complexity. GEANT 4 simulations are currently in progress by Dr. Praveen Shidling to accurately simulate the decays of interest for the initial program, and to aid in making this decision. Additionally, it will be important at this stage to determine the necessity of including a second purification Penning trap before the measurement trap. It is possible that sufficient cleaning will occur from time of flight differences over the travel distance between the RFQ and measurement trap due to varying masses present in the bunched beam that a purification trap will not be necessary [46]. The added complexity and cost of this device will have to be weighed against the likely level of contamination and the effect these unwanted species would have on the ultimate measurement.

Once the geometry has been chosen (whether the novel geometry presented above or a simple, three-electrode configuration), the next step will be to employ the GEANT simulations to determine the detection scheme necessary for the initial experimental program. Currently, position sensitive annular dual-sided silicon strip detectors are envisioned to be positioned inside the vacuum chamber, composing the

endcaps of the electrode geometry for the measurement Penning trap; however there are several additional options for the ultimate configuration. In particular, another attractive solution involves placing the detectors out of the magnetic field, which would improve access and ease of assembly. In this scheme, the cyclotron motion of the particles in the magnetic field would be converted to axial motion as the particles pass through the magnetic field gradient. This technique is employed in the time of flight approach to mass spectrometry, and should be equally applicable to the proposed measurements at TAMUTRAP. The detection scheme decision will be aided by complete GEANT 4 simulations and a detailed measurement of the magnetic field gradient of the existing Agilent 72-210 ASR magnet, in order to get a more accurate picture of the flight kinematics for the different decay products.

Once the trap geometry and detection scheme has been established, it will be important to work with the detector manufacturer to build detectors for this facility. If maximum geometric acceptance is desired, it is almost certain that a new detector design will be required, with custom semi-conductor and mounting features. The ultimate characteristics of these detectors will additionally be shaped by knowledge gained from the GEANT simulations.

With the detection scheme fully determined, a mechanical design of the trap, vacuum system, and electronics must be defined. This is a significant project with a currently estimated time of completion set in 2017.

7. CONCLUSION

Significant development on the TAMUTRAP experiment at the Texas A&M University Cyclotron Institute has been achieved over the past nearly six years. The high bay, where the experiment is situated, has evolved from nothing more than blank cement shielding blocks, to the facility that has been discussed and pictured in this thesis. The notion of the experiment has progressed from a schematic idea, to a detailed concept that partially exists in steel and aluminum. This development, guided, supported, and nurtured by Dr. Dan Melconian, has been brought about largely by Dr. Praveen Shidling and myself, and has served as the work composing this PhD thesis in applied physics.

Through literature reviews, calculations, and, various simulations, the idea for the $0^+ \rightarrow 0^+$ superallowed $T = 2$ beta-delayed proton decay measurements was fleshed out and understood. The outline of the ultimate measurement trap was determined by decay kinematic calculations for the ions and products of interest, and a Monte Carlo simulation reassured the group of the feasibility of studying the proton energy spread to access information about the nature of the SM and the weak interaction itself. The measurement program, once completed, should yield a higher precision measurement of the beta-neutrino correlation parameter than has been attained so far by observing the decay of ^{32}Ar. In addition, the capability of the Texas A&M University Cyclotron Institute to produce several analogous nearby nuclei will allow for a more thorough investigation of the weak interaction by this means than ever before.

Using SIMION, the beam optics necessary to transport radioactive beam from the T-REX gas catcher to the ultimate site of the measurement apparatus was developed.

Once vetted by experts at leading facilities, the theoretical beamline was realized first in CAD with Autodesk Inventor, and ultimately in reality. A great deal of time was dedicated to this design, ensuring not only that the facility would ultimately be ideal for the measurements of interest, but also that maximum flexibility is retained in the design for future upgrades, expansions, or programs. When complete, the TAMUTRAP experiment will be a very unique facility for nuclear physics. This, combined with the generous amount of beamtime accessible to research at the Texas A&M University Cyclotron Institute, will make for a very attractive experimental site.

Apart from the measurement trap, the heart of the facility is composed of the RFQ cooler/buncher Paul trap. This device was designed originally for the TAMUTRAP experiment. After initial SIMION simulations confirmed the electrode structure geometry, the mechanical design was performed in Autodesk Inventor and scrutinized by experts in the field. The design features a rigid mechanical structure that is symmetric along the beam axis, unlike nearly all existing traps that are used in this capacity, which ensures great future flexibility. The device has been precision machined, assembled with great concern for vacuum integrity, and installed in the TAMUTRAP beamline. An initial characterization has been performed on the device showing that, for the quantities measured, the apparatus performs competitively with instruments employed at world class facilities, and should be suitable for beam preparation at TAMUTRAP. Additional work needs to be performed for a full characterization of the device, though substantial development of detector and acquisition systems, in addition to an offline ion source with improved stability, will be needed before this can be completed.

All effort mentioned so far has been directed toward the goal of performing precision beta-decay measurements in the envisioned TAMUTRAP measurement Penning trap. Considering solely the initial measurement of interest, a very simple three-

electrode structure would have sufficed. However, to make the TAMUTRAP facility truly adaptable to a wide range of future experiments, a novel, large-bore, short-endcap Penning trap geometry was developed for the first time. Analytic calculations defining the electric field of the proposed structure, which had not previously been mentioned in the literature, were performed, and the resulting geometry was optimized to generate a highly quadratic electric field at the trap center, a feature that is necessary for many precision frequency measurements. The analytic solution was simulated in SIMION, and proved consistent with the calculated field. The proposed geometry was compared to existing Penning trap facilities, and would offer the largest inner diameter of any existing Penning trap, if fabricated. The critical characteristics of the electric field were shown to compare quite favorably to existing traps at world-class facilities [37].

The next steps in the development of the TAMUTRAP experiment are continued assembly and testing of the beamline and further evolution of the measurement trap design. The mechanical design for the beamline is nearly complete, so that additional work on these components will mostly involve fabrication and assembly of several feet of new beamline, followed by testing, which is expected to be completed sometime in 2016. Development of the measurement Penning trap entails determining the detection scheme that will be employed in the final experiment and weighing the pros and cons of going with the flexible design discussed above as opposed to the simpler design, which would be used for one type of measurement. This decision will be facilitated by examining detailed GEANT 4 calculations currently being performed by Praveen Shidling with an expected completion time frame of 2016. Once the decision has been made, mechanical design of the trap should be completed, before fabrication, assembly and integration in to the existing beamline in 2017. Finally, commissioning of the device will complete the initial development program of the

TAMUTRAP facility, expected sometime in 2018.

As envisioned, the TAMUTRAP facility will become a unique experiment at the Texas A&M University Cyclotron Institute. The primary program of $0^+ \rightarrow 0^+$ superallowed $T = 2$ beta-delayed proton decay measurements will give new insight into the inner workings of the weak force and the SM, and the facility will fill the particular general purpose trapped particle end-station niche that is currently unoccupied at the Texas A&M University Cyclotron Institute and underserved in the nuclear physics community. The idea that existed in 2009 when I embarked on this project is now partly a reality as a result of the work of Dan Melconian, Praveen Shidling, and myself, and the help and guidance of countless others, and I have faith that it will continue to grow toward its potential under their stewardship.

REFERENCES

[1] E.G. Adelberger, C. Ortiz, A. Garcia, H.E. Swanson, M. Beck, O. Tengblad, M.J.G. Borge, I. Martel, and H. Bichsel. Positron-neutrino correlation in the $0^+ \rightarrow 0^+$ decay of ^{32}Ar. *Physical review letters*, 83(7):1299–1302, 1999.

[2] Agilent Technologies. Agilent — chemical analysis, life sciences, and diagnostics, August 2012. http://www.agilent.com.

[3] M. Amoretti, C. Amsler, G. Bonomi, A. Bouchta, P. Bowe, C. Carraro, C.L. Cesar, M. Charlton, M.J.T. Collier, M. Doser, V. Filippini, K.S. Fine, A. Fontana, M.C. Fujiwara, R. Funakoshi, P. Genova, J.S. Hangst, R.S. Hayano, M.H. Holzscheiter, L.V. Jrgensen, V. Lagomarsino, R. Landua, D. Lindelof, E. Lodi Rizzini, M. Macri, N. Madsen, G. Manuzio, M. Marchesotti, P. Montagna, H. Pruys, C. Regenfus, P. Riedler, J. Rochet, A. Rotondi, G. Rouleau, G. Testera, A. Variola, T.L. Watson, and D.P. van der Werf. Production and detection of cold antihydrogen atoms. *Nature*, 419(6906):456–9, October 2002.

[4] R.A. Battye and A. Moss. Evidence for massive neutrinos from cosmic microwave background and lensing observations. *Phys. Rev. Lett.*, 112:051303, Feb 2014.

[5] J.A. Behr and G. Gwinner. Standard model tests with trapped radioactive atoms. *Journal of Physics G: Nuclear and Particle Physics*, 36(3):033101, 2009.

[6] J.M. Blatt and V.F. Weisskopf. *Theoretical Nuclear Physics*. Dover Publications, Inc., New York, NY, 1979.

[7] H.K. Blaum and F. Herfurth. Trapped charged particles and fundamental interactions. *Lecture Notes in Physics*, 749, 2008.

[8] K. Blaum. High-accuracy mass spectrometry with stored ions. *Physics Reports*, 425(1):1–78, March 2006.

[9] G. Bollen, R.B. Moore, G. Savard, and H. Stolzenberg. The accuracy of heavy-ion mass measurements using time of flight-ion cyclotron resonance in a Penning trap. *Journal of Applied Physics*, 68(9):4355, 1990.

[10] Y. Boran. Development of an offline ion source for use at TAMUTRAP. Master's thesis, 2013.

[11] M. Brodeur. *First direct mass measurement of the two and four neutron halos* ^{6}*He and* ^{8}*He using the TITAN Penning trap mass spectrometer*. PhD thesis, University of British Columbia, 2010.

[12] M. Brodeur et al. Verifying the accuracy of the TITAN Penning-trap mass spectrometer. *Int. J. Mass Spec.*, 310:20–31, 2012.

[13] F. Duval, A. Mery, G. Ban, D. Durand, X. Flechard, M. Labalme, E. Lienard, F. Mauger, O. Naviliatcuncic, and D. Rodriguezrubiales. Status of the LPC-Trap facility at GANIL. *Nuclear Instruments and Methods in Physics Research Section B: Beam Interactions with Materials and Atoms*, 266(19-20):4537–4541, October 2008.

[14] E. Fermi. Versuch einer theorie der -strahlen. i. *Zeitschrift für Physik*, 88(3-4):161–177, 1934.

[15] R. Feynman and M. Gell-Mann. Theory of the fermi interaction. *Phys. Rev.*, 109:193–198, Jan 1958.

[16] C. Folden. Private Communication, 2015.

[17] H. Franberg, P. Delahaye, J. Billowes, K. Blaum, R. Catherall, F. Duval, O. Gianfrancesco, T. Giles, A. Jokinen, and M. Lindroos. Off-line commissioning of the ISOLDE cooler. *Nuclear Instruments and Methods in Physics Research Section B: Beam Interactions with Materials and Atoms*, 266(19-20):4502–4504, October 2008.

[18] H.O. Funsten, S.M. Ritzau, R.W. Harper, and R. Korde. Fundamental limits to detection of low-energy ions using silicon solid-state detectors. *Applied Physics Letters*, 84(18), 2004.

[19] G. Gabrielse. Relaxation calculation of the electrostatic properties of compensated Penning traps with hyperbolic electrodes. *Physical Review A*, 27(5):2277, 1983.

[20] G. Gabrielse. The true cyclotron frequency for particles and ions in a Penning trap. *International Journal of Mass Spectrometry*, 279(2-3):107–112, January 2009.

[21] G. Gabrielse, L. Haarsma, and S.L. Rolston. Open-endcap experiments penning traps for high precision experiments. *Journal of Mass Spectrometry*, 88:319–332, 1989.

[22] G. Gamow and E. Teller. Selection rules for the β-disintegration. *Phys. Rev.*, 49:895–899, Jun 1936.

[23] R.L. Garwin, L.M. Lederman, and M. Weinrich. Observations of the failure of conservation of parity and charge conjugation in meson decays: the magnetic moment of the free muon. *Phys. Rev.*, 105:1415–1417, Feb 1957.

[24] A. Gorelov, D. Melconian, W. P. Alford, D. Ashery, G. Ball, J. A. Behr, P. G. Bricault, J. M. D'Auria, J. Deutsch, J. Dilling, M. Dombsky, P. Dubé, J. Fingler, U. Giesen, F. Glück, S. Gu, O. Häusser, K. P. Jackson, B. K. Jennings, M. R. Pearson, T. J. Stocki, T. B. Swanson, and M. Trinczek. Scalar interaction limits from the $\beta-\nu$ correlation of trapped radioactive atoms. *Phys. Rev. Lett.*, 94:142501, Apr 2005.

[25] J. C. Hardy and I. S. Towner. Superallowed $0^+ \to 0^+$ nuclear β decays: A new survey with precision tests of the conserved vector current hypothesis and the standard model. *Phys. Rev. C*, 79:055502, May 2009.

[26] F. Herfurth, J. Dilling, A. Kellerbauer, G. Bollen, S. Henry, H.J. Kluge, E. Lamour, D. Lunney, R.B. Moore, C. Scheidenberger, and Others. A linear radiofrequency ion trap for accumulation, bunching, and emittance improvement of radioactive ion beams. *Nuclear Instruments and Methods in Physics Research Section A: Accelerators, Spectrometers, Detectors and Associated Equipment*, 469(2):254–275, 2001.

[27] B. Holstein. Recoil effects in allowed beta decay: The elementary particle approach. *Reviews of Modern Physics*, 46(4):789–814, October 1974.

[28] J. Jackson, S. Treiman, and H. Wyld. Possible tests of time reversal invariance in beta decay. *Physical Review*, 106(3):517–521, May 1957.

[29] J.D. Jackson, S.B. Treiman, and H.W. Wyld. Coulomb corrections in allowed beta transitions. *Nuclear Physics*, 4:206–212, 1957.

[30] A. Kellerbauer, T. Kim, R.B. Moore, and P. Varfalvy. Buffer gas cooling of ion beams. *Nuclear Instruments and Methods in Physics Research Section A:*

Accelerators, Spectrometers, Detectors and Associated Equipment, 469(2):276–285, 2001.

[31] V. Kolhinen, S. Kopecky, T. Eronen, U. Hager, J. Hakala, J. Huikari, A. Jokinen, A .and Nieminen, S. Rintaantila, and J. Szerypo. JYFLTRAP: a cylindrical Penning trap for isobaric beam purification at IGISOL. *Nuclear Instruments and Methods in Physics Research Section A: Accelerators, Spectrometers, Detectors and Associated Equipment*, 528(3):776–787, August 2004.

[32] V.Y. Kozlov, M. Beck, S. Coeck, M. Herbane, I.S. Kraev, N. Severijns, F. Wauters, P. Delahaye, A. Herlert, F. Wenander, and D. Zakoucky. The WITCH experiment: towards weak interactions studies. Status and prospects. *Hyperfine Interactions*, 175:15–22, 2006.

[33] H. Kreckel, H. Bruhns, K.A. Miller, E. Wahlin, A. Davis, S. Höckh, and D.W. Savin. A simple double-focusing electrostatic ion beam deflector. *The Review of scientific instruments*, 81(6):063304, June 2010.

[34] T.D. Lee and C.N. Yang. Question of parity conservation in weak interactions. *Physical Review*, 104:254–258, October 1956.

[35] G.E. Lee-Whiting and L. Yamazaki. Semi-analytical calculations for circular quadrupoles. *Nuclear Instruments and Methods*, 94(2):319 – 332, 1971.

[36] P.J. Linstrom and W.G. Mallard, editors. *NIST Chemistry WebBook, NIST Standard Reference Database Number 69*. National Institute of Standards and Technology, Gaithersburg MD, 20899, 2012.

[37] M. Mehlman, D. Melconian, and P. D. Shidling. Texas A&M Penning trap facility - design of the measurement trap. arXiv:1208.4078, August 2012.

[38] D. Melconian. The β^+ decay of a $0^+ \rightarrow 0^+$ Transition. March 2001.

[39] D. Melconian. Implementing recoil-order corrections. March 2011.

[40] S. Molitor. Private Communication, 2014.

[41] J.B. Neumayr, L. Beck, D. Habs, S. Heinz, J. Szerypo, P. Thirolf, V. Varentsov, F. Voit, D. Ackermann, and D. Beck. The ion-catcher device for SHIPTRAP. *Nuclear Instruments and Methods in Physics Research Section B: Beam Interactions with Materials and Atoms*, 244(2):489–500, March 2006.

[42] W. Paul and H. Steinwedel. Ein neues Massenspektrometer ohne Magnetfeld. *Zeitschrift Naturforschung Teil A*, 8:448, 1953.

[43] H. Raimbault-Hartmann, D. Beck, G. Bollen, M. Konig, H.J. Kluge, E. Schark, J. Stein, S. Schwarz, and J. Szerypo. A cylindrical Penning trap for capture, mass selective cooling, and bunching of radioactive ion beams. *Nuclear Instruments and Methods in Physics Research Section B: Beam Interactions with Materials and Atoms*, 126(1-4):378–382, 1997.

[44] R. Reiszig and F.M. Arscott. Periodic differential equations. *ZAMM - Journal of Applied Mathematics and Mechanics / Zeitschrift für Angewandte Mathematik und Mechanik*, 45(6):453–454, 1965.

[45] J. Repp, C. Böhm, J. R. Crespo López-Urrutia, A. Dörr, S. Eliseev, S. George, M. Goncharov, Y. N. Novikov, C. Roux, S. Sturm, S. Ulmer, and K. Blaum. PENTATRAP: a novel cryogenic multi-Penning-trap experiment for high-precision mass measurements on highly charged ions. *Applied Physics B: Lasers and Optics*, 107:983–996, June 2012.

[46] R. Ringle. Private Communication, 2014.

[47] R. Ringle, G. Bollen, A. Prinke, J. Savory, P. Schury, S. Schwarz, and T. Sun. The Lebit 9.4T Penning trap mass spectrometer. *Nuclear Instruments and Methods in Physics Research Section A: Accelerators, Spectrometers, Detectors, and Associated Equipment*, 3(604):536–547, 2009.

[48] D.R. Rubiales. *A radiofrequency quadrupole buncher for accumulation and cooling of heavy radionuclides at SHIPTRAP and high precision mass measurements on unstable krypton isotopes at ISOLTRAP*. PhD thesis, 2003.

[49] G. Savard, S. Baker, C. Davids, A.F. Levand, E.F. Moore, R.C. Pardo, R. Vondrasek, B.J. Zabransky, and G. Zinkann. Radioactive beams from gas catchers: The caribu facility. *Nuclear Instruments and Methods in Physics Research Section B: Beam Interactions with Materials and Atoms*, 266(1920):4086 – 4091, 2008. Proceedings of the 15th International Conference on Electromagnetic Isotope Separators and Techniques Related to their Applications.

[50] Scientific Instrument Services, Inc. Industry standard charged particle optics simulation software, August 2012. http://www.simion.com.

[51] N. Severijns, M. Beck, and O. Naviliat-Cuncic. Tests of the standard electroweak model in beta decay. *Reviews of Modern Physics*, 78:991–1040, 2006.

[52] N. Severijns, J. Deutsch, D. Beck, M. Beck, B. Delauré, T. Phalet, R. Prieels, P. Schuurmans, B. Vereecke, and S. Versyck. Fundamental weak interaction studies using polarised nuclei and ion traps. *Hyperfine Interactions*, 129(1-4):223–236, 2000.

[53] N. Severijns and O. Naviliat-Cuncic. Symmetry tests in nuclear beta decay. *Annual Review of Nuclear and Particle Science*, 61:23–46, 2011.

[54] P.D. Shidling. Private Communication, 2014.

[55] M. Smith. *A square-wave-driven radiofrequency quadrupole cooler and buncher for TITAN*. PhD thesis, 2005.

[56] G.A. Souliotis, A.L. Keksis, B.C. Stein, M. Veselsky, M. Jandel, D.V. Shetty, S.N. Soisson, S. Wuenschel, and S.J. Yennello. Rare isotope production in the Fermi energy regime and application to the Texas A&M RIB Upgrade. *Nuclear Instruments and Methods in Physics Research Section B: Beam Interactions with Materials and Atoms*, 261(1-2):1094–1097, August 2007.

[57] M.P. Stockli. *Measuring and analyzing the transverse emittance of charged particle beams*. 2008.

[58] M. Strohmeier. Development of a pepperpot device to determine the emittance of an ion beam generated by an ECR ion source. Master's thesis, 2009.

[59] M. Strohmeier. Private Communication, 2012.

[60] E. Sudarshan and R. Marshak. Chirality invariance and the universal fermi interaction. *Phys. Rev.*, 109:1860–1862, Mar 1958.

[61] J. Wang, G. Savard, K. Sharma, J. Clark, Z. Zhou, A. Levand, C. Boudreau, F. Buchinger, J. Crawford, and J. Greene. The Canadian Penning Trap mass spectrometer. *Nuclear Physics A*, 746:651–654, December 2004.

[62] J.G. Wang, D.X. Wang, and M. Reiser. Beam emittance measurement by the pepper-pot method. *Nuclear Instruments and Methods in Physics Research Section A: Accelerators, Spectrometers, Detectors and Associated Equipment*, 307(2-3):190–194, October 1991.

[63] S. Weinberg. A model of leptons. *Phys. Rev. Lett.*, 19:1264–1266, Nov 1967.

[64] Wolfram Research. Wolfram: computation meets knowledge, August 2012. http://www.wolfram.com.

[65] C.S. Wu. Experimental test of parity conservation in beta decay. *Physical Review*, 105(4):1413–1415, February 1957.

APPENDIX A

OPTIMIZED OPERATING PARAMETERS FOR THE RFQ COOLER/BUNCHER

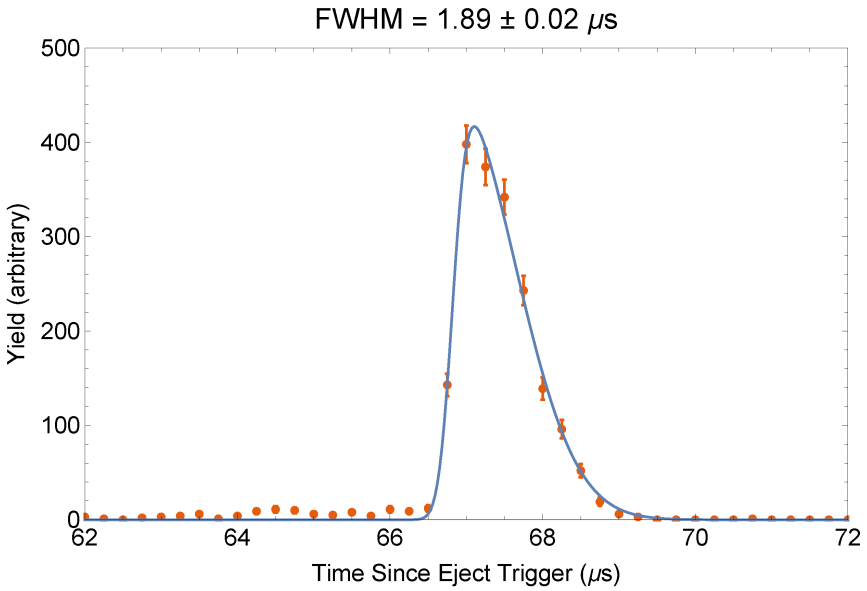

Figure A.1: A good bunch with timespread FWHM = 1.89 μs. Beam energy = 30 eV, gas pressure = 3×10^{-3} mbar He, drag potential = 0.08 V/cm, incident beam current =0.07 pA.

This appendix contains a reference of the best bunched mode settings recorded to date, presented in Table A.1. The results (seen in Fig. A.1) are reproducible, with only the voltages on some steerers occasionally requiring adjustment.

Parameter	Value
Incident beam current	0.07 pA
Ion gun platform	9.97 kV
RFQ platform	9.94 kV
Beam energy	30 eV
RFQ frequency	1.0 MhZ
RFQ voltage (peak to peak)	107 V
Gas pressure (99.999% He)	3×10^{-3} mbar
Drag potential	≈ 0.08 V/cm
Eject duration	53.75 μs
Cooling time	250 ms
MCP front	0 V
MCP back	1848 V
MCP screen	2100 V
CFD threshold	1 V
Einzel 1	6 kV
Steerer 1 (l,r,t,b)	6, 5, 70, 1 V
Injection steerer (l,r,t,b)	230, 0, 30, -40 V
Injection electrode 1	7625 V
Injection electrode 2	8100 V
Injection diaphragm	0 V
RFQ S1 DC	0.08 V
RFQ S2 DC	0.16 V
RFQ S3 DC	0.24 V
RFQ S4 DC	0.32 V
RFQ S5 DC	0.40 V
RFQ VD 1 DC	0.48 V
RFQ VD 2 DC	5.80 V
RFQ S29 DC	5.88 V
RFQ S30 DC	5.96 V
RFQ S31 DC	6.04 V
RFQ S32 DC	11.04 V
RFQ S33+ DC	275 V
RFQ S33− DC	−110 V
Extraction diaphragm	0 V
Extraction electrode 1	−1300 V
Extraction electrode 2	−200 V
Extraction electrode 3	−1300 V
Extraction steerer (l,r,t,b)	0, 0, 0, 0 V

Table A.1: Operating parameters for the bunch pictured in Fig. A.1. Drag potential is approximately 0.08 V/cm.

APPENDIX B

ELECTRIC FIELD OF THE MEASUREMENT TRAP

In this appendix, the calculations employed to define the electric field of the measurement Penning trap are presented. The derivation is similar to that of [21]; however, with modifications necessary for application in the TAMUTRAP facility. That is, the infinite-endcap approximation has been removed, and flat endcaps which can be held at an arbitrary voltage are considered. One set of compensation electrodes is considered, as in Figure B.1.

Before we begin, let us set up the geometry such that the direction $\hat{z}$ represents the axial direction within the trap, and the direction $\hat{\rho}$ represents the radial direction within the trap. We will also consider only one half of the trap, $z \geq 0$, due to symmetry.

To start, let us recognize that any potential can be written as an expansion in Legendre polynomials (here we use the even terms only, due to symmetry across the mid-plane, $z = 0$):

$$V = \frac{1}{2} V_0 \sum_{\substack{k=0 \\ k \text{ even}}}^{\infty} B_k \left(\frac{r}{d}\right)^k P_k \left(\cos\theta\right). \tag{B.1}$$

Here, d is the characteristic trap distance as in [21]:

$$d = \sqrt{\frac{1}{2}\left(\left(z_r + z_g + z_c + z_g\right)^2 + \frac{1}{2}{\rho_0}^2\right)}. \tag{B.2}$$

Now, by superposition we can write the potential at the trap center as a sum of the

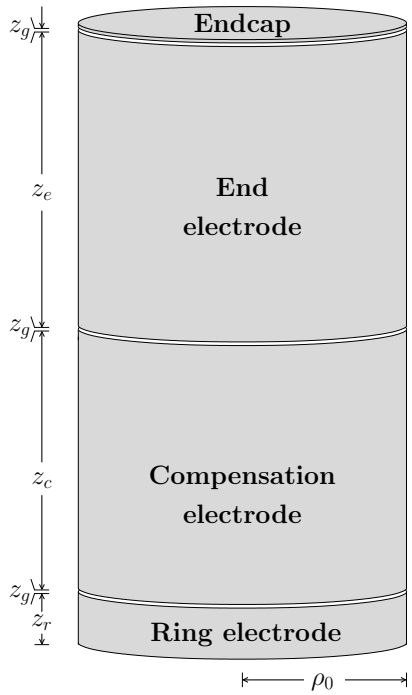

$\boldsymbol{\phi_0}$ $\rho = \rho_0$	$\boldsymbol{\phi_1}$ $\rho = \rho_0$	$\boldsymbol{\phi_2}$ $\rho \leq \rho_0$
0	0	1
0.5	0	0
0	1	0
-0.5	0	0

Figure B.1: The trap geometry and boundary conditions used in the analytic solution. The device is symmetric about the $z = 0$ plane.

potentials of each of the contributing electrodes:

$$V = V_0\phi_0 + V_1\phi_1 + V_2\phi_2. \tag{B.3}$$

For this geometry, ϕ_0 is due to the ring and end electrodes (the primary potential well), and ϕ_1 and ϕ_2 are from the compensation and endcap electrodes respectively. Since V_0, V_1, and V_2 are adjustable parameters to define the final voltage scale of each electrode, we may take the unscaled potentials to be defined as follows:

$$\begin{aligned}
\phi_0 &= \begin{cases} 1/2 & \text{if } z_r + z_g + z_c + z_g \le z \le z_r + z_g + z_c + z_g + z_e \text{ and } \rho = \rho_0 \\ -1/2 & \text{if } 0 \le z \le z_r \text{ and } \rho = \rho_0 \\ 0 & \text{else} \end{cases} \\
\phi_1 &= \begin{cases} 1 & \text{if } z_r + z_g \le z \le z_r + z_g + z_c \text{ and } \rho = \rho_0 \\ 0 & \text{else} \end{cases} \\
\phi_2 &= \begin{cases} 1/2 & \text{if } z = z_r + z_g + z_c + z_g + z_e \text{ and } \rho \le \rho_0 \\ 0 & \text{else.} \end{cases}
\end{aligned} \tag{B.4}$$

Each of these potentials can in turn be expanded in Legendre polynomials:

$$\begin{aligned}
\phi_0 &= \tfrac{1}{2} \sum_{\substack{k=0 \\ k \text{ even}}}^{\infty} C_k \left(\tfrac{r}{d}\right)^k P_k(\cos\theta) \\
\phi_1 &= \tfrac{1}{2} \sum_{\substack{k=0 \\ k \text{ even}}}^{\infty} D_k \left(\tfrac{r}{d}\right)^k P_k(\cos\theta) \\
\phi_2 &= \tfrac{1}{2} \sum_{\substack{k=0 \\ k \text{ even}}}^{\infty} E_k \left(\tfrac{r}{d}\right)^k P_k(\cos\theta).
\end{aligned} \tag{B.5}$$

Plugging these back into Equation B.3 yields the simple result:

$$B_k = C_k + D_k \frac{V_1}{V_0} + E_k \frac{V_2}{V_0}. \tag{B.6}$$

The next step is to solve for each of the expansion coefficients, C_k, D_k, and E_k. Each of the potentials which are due to electrodes shaped like hollow cylinders can be found more naturally using an expansion in Bessel functions,

$$\phi_i = \sum_{n=0}^{\infty} A_n J_0 \left(\imath k_n \rho\right) \cos\left(k_n z\right), \tag{B.7}$$

where we have applied the periodic boundary condition in z such that:

$$k_n = \frac{\left(n + \frac{1}{2}\right)\pi}{z_{tot}}. \tag{B.8}$$

Setting Equation B.7 equal to the expansion in Legendre polynomials (Eqs. B.1 and B.5) allows us to solve for the expansion coefficients of the Legendre polynomials. Below, the procedure for the primary well is shown.

$$\frac{1}{2} \sum_{\substack{k=0 \\ k \text{ even}}}^{\infty} C_k \left(\frac{r}{d}\right)^k P_k \left(\cos\theta\right) = V_i \sum_{n=0}^{\infty} A_n^C J_0 \left(\imath k_n \rho\right) \cos\left(k_n z\right) \tag{B.9}$$

If we choose to solve this along $\hat{z}$, then $\theta \to 0$, $\cos\theta \to 1$, $P_k \to 1$, $\rho \to 0$, $r \to z$, and $J_0\left(0\right) \to 1$, which simplifies Equation B.9:

$$\frac{1}{2} \sum_{\substack{k=0 \\ k \text{ even}}}^{\infty} C_k \left(\frac{r}{d}\right)^k = V_i \sum_{n=0}^{\infty} A_n^C \cos\left(k_n z\right). \tag{B.10}$$

Expanding the cosine term gives

$$\frac{1}{2} \sum_{\substack{k=0 \\ k \text{ even}}}^{\infty} C_k \left(\frac{r}{d}\right)^k = V_i \sum_{n=0}^{\infty} A_n^C \sum_{\substack{k=0 \\ k \text{ even}}}^{\infty} \frac{\left(-1\right)^{k/2}}{k!} \left(k_n z\right)^k. \tag{B.11}$$

Equating powers of k gives the coefficient for ϕ_0:

$$C_k = \sum_{n=0}^{\infty} \frac{2A_n^C d^k {k_n}^k (-1)^{k/2}}{k!}. \tag{B.12}$$

And the coefficient for ϕ_1 can similarly be found to be

$$D_k = \sum_{n=0}^{\infty} \frac{2A_n^D d^k {k_n}^k (-1)^{k/2}}{k!}. \tag{B.13}$$

Now we need to apply additional boundary conditions in order to determine A_n^i. Setting the expansion in Bessel functions (Eq. B.7) equal to the potential at the boundary under consideration, ϕ_i, multiplying by $\cos(k_m z)$, and integrating over the boundary allows us to take advantage of the orthogonality of cosines[1] and solve for the coefficients ${A_n}^i$. According to this procedure, solving for A_n^C goes like:

$$\phi_0 = \sum_{n=0}^{\infty} A_n^C J_0(\imath k_n \rho) \cos(k_n z). \tag{B.14}$$

Multiplying by $\cos(k_m z)$ and integrating over the boundary gives

$$\int_{\substack{0 \\ \text{boundary}}}^{z_{tot}} \phi_0 \cos(k_m z)\, \mathrm{d}z = \int_{\substack{0 \\ \text{boundary}}}^{z_{tot}} \sum_{n=0}^{\infty} A_n^C J_0(\imath k_n \rho) \cos(k_n z)\, \mathrm{d}z. \tag{B.15}$$

Taking the integral of both sides and substituting in the actual potential ϕ_0 (the left hand side must be integrated over the electrode boundary and the right hand side

[1]We did not have to take advantage of the orthogonality of the Bessel functions here since the boundary conditions are only defined at ρ_0 and the Bessel functions are only functions of the radius, ρ.

benefits from the orthogonality of cosines) yields

$$\begin{aligned}&\frac{1}{k_n}\Bigg\{\frac{1}{2}\sin\left(k_n(z_r+z_g+z_c+z_g+z_e)\right)-\\&\frac{1}{2}\sin\left(k_n\left(z_r+z_g+z_c+z_g\right)\right)-\\&\frac{1}{2}\sin\left(k_n z_r\right)+0\Bigg\}\\&=A_n^C J_0\left(\imath k_n\rho_0\right)\frac{z_{tot}}{2},\end{aligned}\tag{B.16}$$

which allows us to solve for A_n^C:

$$A_n^C=\frac{\sin\left(k_n(z_r+z_g+z_c+z_g+z_e)\right)-\sin\left(k_n\left(z_r+z_g+z_c+z_g\right)\right)-\sin\left(k_n z_r\right)}{k_n z_{tot}J_0\left(\imath k_n\rho_0\right)}.\tag{B.17}$$

Below the same derivation is shown for A_n^D in order to clarify the boundary definitions:

$$\phi_1=\sum_{n=0}^{\infty}A_n^D J_0\left(\imath k_n\rho\right)\cos\left(k_n z\right)\tag{B.18}$$

$$\int\limits_{\substack{0\\\text{boundary}}}^{z_{tot}}\phi_1\cos\left(k_m z\right)\,\mathrm{d}z=\int\limits_{\substack{0\\\text{boundary}}}^{z_{tot}}\sum_{n=0}^{\infty}A_n^D J_0\left(\imath k_n\rho\right)\cos\left(k_n z\right)\,\mathrm{d}z\tag{B.19}$$

$$\frac{1}{k_n}\left\{\sin\left(k_n\left(z_r+z_g+z_c\right)\right)-\sin\left(k_n\left(z_r+z_g\right)\right)\right\}=A_n^D J_0\left(\imath k_n\rho_0\right)\frac{z_{tot}}{2}\tag{B.20}$$

$$A_n^D=\frac{2\left\{\sin\left(k_n\left(z_r+z_g+z_c\right)\right)-\sin\left(k_n\left(z_r+z_g\right)\right)\right\}}{k_n z_{tot}J_0\left(\imath k_n\rho_0\right)}.\tag{B.21}$$

Now we need to look at the contribution to the potential from the endcaps. This potential, ϕ_2, is defined at z_{tot} for any radius less than ρ_0. Most generally, we can write:

$$\phi_2=\sum_{m=0}^{\infty}\sum_{n=0}^{\infty}J_m\left(k_{mn}\rho\right)e^{k_{mn}z}\left(A_m\sin(m\phi)+B_m\cos(m\phi)\right).\tag{B.22}$$

In Equation B.22, the unlabeled ϕ represents the azimuthal angle. At $\rho=\rho_0$, $\phi_2\to 0$,

since the other electrodes occur at ρ_0 and generate their own potentials. Because of this, we can see that the k_{mn}'s are related to the zeroes of the Bessel functions as in Equation B.23.

$$k_{mn} = \frac{x_{mn}}{\rho_0} \tag{B.23}$$

Here, x_{mn} is the n^{th} zero of the m^{th} Bessel function (where n is a positive integer). Since we have cylindrical symmetry, $m \equiv 0$,

$$\phi_2 = \sum_{n=0}^{\infty} J_m\left(k_{0n}\rho\right) e^{k_{0n}z} B_n \equiv V_2 \text{ (on the electrode).} \tag{B.24}$$

B_n can now be determined through the application of appropriate boundary conditions and the Bessel function orthogonality relation. Say $\phi_2 = V_0$ on the electrode surface[2], that is, at $z = z_{tot}$ and $\rho \leq \rho_0$. Multiplying by $\rho J_m(k_{0m}\rho)\,\mathrm{d}\rho$, inserting the value of ϕ_2, and integrating over the radius of the endcap electrode (at $z = z_{tot}$) gives

$$\int_0^{\rho_0} \rho J_m(k_{0m}\rho)\,\mathrm{d}\rho = \int_0^{\rho_0} \sum_{n=1}^{\infty} J_0\left(k_{0n}\rho\right) e^{k_{0n}z_{tot}} B_n \rho J_m(k_{0m}\rho)\,\mathrm{d}\rho. \tag{B.25}$$

Performing the integration yields (again, x_{mn} refer to the zeroes of the Bessel functions)

$$\frac{{\rho_0}^2 J_1(x_{0m})}{x_{0m}} = e^{k_{0n}z_{tot}} B_n {\rho_0}^2 {J_1}^2(x_{0n}\rho)\delta_{mn}, \tag{B.26}$$

from which we can solve for B_n:

$$B_n = \frac{2e^{-k_{0n}z_{tot}}}{x_{0n}J_1(x_{0n})}. \tag{B.27}$$

Substituting this back into Equation B.22 and taking into account both endcaps

[2]This procedure may be modified to account for small apertures in the endcap electrodes; however, in practice the affect of these features on the potential is quite small.

(at $\pm z$) yields the complete formulation of the potential due to the endcaps at any z:

$$\phi_2 = \frac{V_2}{2}\left(\sum_{n=1}^{\infty} J_0\left(\frac{x_{0n}}{\rho_0}\rho\right) e^{\frac{x_{0n}}{\rho_0}(z)} \frac{2e^{-k_{0n}z_{tot}}}{x_{0n}J_1(x_{0n})} + \sum_{n=1}^{\infty} J_0\left(\frac{x_{0n}}{\rho_0}\rho\right) e^{\frac{x_{0n}}{\rho_0}(-z)} \frac{2e^{-k_{0n}z_{tot}}}{x_{0n}J_1(x_{0n})}\right). \tag{B.28}$$

Next, we set this equal to the potential expanded in Legendre polynomials (Eq. B.5) along the z-axis ($\rho = 0$).

$$\frac{1}{2}\sum_{\substack{k=0 \\ k \text{ even}}}^{\infty} E_k\left(\frac{z}{d}\right)^k = \frac{V_2}{2}\left(\sum_{n=1}^{\infty} J_0\left(\frac{x_{0n}}{\rho_0}0\right) e^{\frac{x_{0n}}{\rho_0}(z)} \frac{2e^{-k_{0n}z_{tot}}}{x_{0n}J_1(x_{0n})} + \sum_{n=1}^{\infty} J_0\left(\frac{x_{0n}}{\rho_0}0\right) e^{\frac{x_{0n}}{\rho_0}(-z)} \frac{2e^{-k_{0n}z_{tot}}}{x_{0n}J_1(x_{0n})}\right) \tag{B.29}$$

This reduces to

$$\sum_{\substack{k=0 \\ k \text{ even}}}^{\infty} E_k\left(\frac{z}{d}\right)^k = V_2\left(\sum_{n=1}^{\infty} e^{\frac{x_{0n}}{\rho_0}(z)} \frac{2e^{-k_{0n}z_{tot}}}{x_{0n}J_1(x_{0n})} + \sum_{n=1}^{\infty} e^{\frac{x_{0n}}{\rho_0}(-z)} \frac{2e^{-k_{0n}z_{tot}}}{x_{0n}J_1(x_{0n})}\right). \tag{B.30}$$

The right hand side of Equation B.30 can easily be expanded in a Taylor series using a computer (in practice, as many terms should be used as possible; the solution has been found to be inaccurate with fewer than fifty terms calculated in the Taylor series). This allows us to define the expansion coefficients E_k in terms of the calculated Taylor coefficients, which we may call SC_k:

$$\sum_{k=0}^{\infty} E_k\left(\frac{z}{d}\right)^k = \sum_{k=0}^{\infty} V_0 SC_k z^k. \tag{B.31}$$

This in turn gives the final result for the expansion coefficients E_k:

$$E_k = V_0 S C_k d^k. \tag{B.32}$$

All expansion coefficients from Equation B.6 have now been completely defined, and the electric field at the trap center can be specified to arbitrary precision (depending on the number of terms calculated in the Taylor expansion employed in Equation B.31). By construction, it is easy to characterize the components of this field, which allows for a straightforward optimization as discussed in the main text.